



**HAL**  
open science

## Turbulence characteristics and mixing properties of gravity currents over complex topography

Maria Rita Maggi, Maria Eletta Negretti, Emil Hopfinger, Claudia Adduce

► **To cite this version:**

Maria Rita Maggi, Maria Eletta Negretti, Emil Hopfinger, Claudia Adduce. Turbulence characteristics and mixing properties of gravity currents over complex topography. *Physics of Fluids*, 2023, 35 (1), 10.1063/5.0132830 . hal-04252424

**HAL Id: hal-04252424**

**<https://hal.science/hal-04252424>**

Submitted on 20 Oct 2023

**HAL** is a multi-disciplinary open access archive for the deposit and dissemination of scientific research documents, whether they are published or not. The documents may come from teaching and research institutions in France or abroad, or from public or private research centers.

L'archive ouverte pluridisciplinaire **HAL**, est destinée au dépôt et à la diffusion de documents scientifiques de niveau recherche, publiés ou non, émanant des établissements d'enseignement et de recherche français ou étrangers, des laboratoires publics ou privés.

This is the author's peer reviewed, accepted manuscript. However, the online version of record will be different from this version once it has been copyedited and typeset.

PLEASE CITE THIS ARTICLE AS DOI: 10.1063/5.0132830

Accepted to *Phys. Fluids* 10.1063/5.0132830

AIP/123-QED

1 **Turbulence characteristics and mixing properties of gravity currents over complex**  
 2 **topography**

3 Maria Rita Maggi,<sup>1, a)</sup> M. Eletta Negretti,<sup>2</sup> Emil Hopfinger,<sup>2</sup> and Claudia Adduce<sup>1, 3</sup>

4 <sup>1)</sup>*Department of Engineering, Roma Tre University, Via Vito Volterra 62, 00146,*  
 5 *Rome, Italy*

6 <sup>2)</sup>*Univ. Grenoble Alpes, CNRS, Grenoble INP, LEGI, 38000, Grenoble,*  
 7 *France*

8 <sup>3)</sup>*Institute of Marine Sciences, National Research Council, Rome,*  
 9 *Italy*

10 (Dated: 23 December 2022)

11 Understanding gravity currents developing on complex topography, that involve tur-  
 12 bulence and mixing processes on a wide range of spatial and temporal scales, is of  
 13 importance for estimating near ground fluxes in oceanic and atmospheric circula-  
 14 tion. We present experimental results, based on high resolution velocity and density  
 15 measurements, of constant upstream buoyancy supply gravity currents flowing from  
 16 a horizontal boundary onto a tangent hyperbolic shaped slope. The mean flow, the  
 17 turbulence characteristics and mixing properties, the latter expressed in terms of mix-  
 18 ing lengths and eddy coefficients, are determined, highlighting their dependency on  
 19 topography. These mean flow and mixing characteristics are compared with the field  
 20 measurements in katabatic winds by Charrondière, Hopfinger, and Brun<sup>1</sup>, which are  
 21 gravity flows that develop over sloping terrain due to radiative cooling at the surface.  
 22 The results obtained show that the mean katabatic flow structure is substantially  
 23 different from that of the upstream buoyancy supply gravity current. However in-  
 24 terestingly, dimensionless mixing lengths and eddy coefficients compare well despite  
 25 the difference in mean flow structure and a two order of magnitude difference in the  
 26 Reynolds number.

---

<sup>a)</sup>Electronic mail: mariarita.maggi@uniroma3.it

27 **I. INTRODUCTION**

28 Gravity currents are frequent in the natural environment with the density difference being  
 29 due to temperature, salinity, dissolved substances, or particles within the flow. Examples of  
 30 such currents in the atmosphere and oceans are sea breeze fronts<sup>2</sup>, katabatic winds<sup>3-6</sup>, con-  
 31 tinental slope boundary currents<sup>7</sup>, turbidity currents<sup>8</sup> including avalanches<sup>9</sup> and exchange  
 32 flows<sup>10-14</sup>. These frequent and diverse occurrences of gravity currents in the natural environ-  
 33 ment have motivated numerous investigations, of interdisciplinary nature, of these gravity  
 34 flows. Several studies have shown how the propagation of dense, bottom gravity currents is  
 35 affected by topographic aspects<sup>15-22</sup>, by sloping boundaries<sup>23-31</sup> as well as rapidly changing  
 36 slopes<sup>32-35</sup>. Most of these studies have focused on the mean flow dynamics and the related  
 37 entrainment of ambient fluid that strongly affects the flow development and fluid properties.  
 38 Entrainment is related with the type of interfacial instability<sup>36-38</sup> that also depends on initial  
 39 conditions and slope angle<sup>33,34</sup>.

40 Gravity currents involve a large variety of different processes, e.g. flow instabilities,  
 41 boundary layers, vortices and internal waves, which occur in very localized regions, so that  
 42 they cannot be resolved in oceanic and atmospheric circulation models<sup>39</sup>. It is therefore  
 43 necessary to parametrize gravity currents in general circulation models<sup>40</sup>, which requires an  
 44 understanding of the turbulence characteristics and mixing properties.

45 Modern experimental techniques allow high quality, quantitative measurements of the  
 46 mean flow development and entrainment, the turbulence characteristics, and internal mixing.  
 47 Measurements of eddy coefficients and mixing lengths have been conducted in the  
 48 outer part of a gravity current by Odier *et al.*<sup>41</sup> and in lock exchange gravity currents  
 49 by Balasubramanian and Zhong<sup>42</sup>, Agrawal *et al.*<sup>43</sup>, Mukherjee and Balasubramanian<sup>44,45</sup>.  
 50 Measurements in katabatic winds on glaciers and alpine slopes have been performed by  
 51 Princevac, Hunt, and Fernando<sup>4</sup>, Monti, Fernando, and Princevac<sup>46</sup>, Charrondière *et al.*<sup>47</sup>,  
 52 who focused on mean flow oscillations and turbulence characteristics and, more recently, on  
 53 mixing length and eddy coefficients<sup>6</sup>.

54 As it has been mentioned above, previous studies showed how gravity currents are affected  
 55 by topographic features such as sloping boundaries as well as rapidly changing slopes. Here  
 56 we present results of laboratory experiments of continuously supplied saline gravity currents  
 57 flowing onto a tangent hyperbolic shape bottom boundary that reproduces a typical alpine

58 topography<sup>6</sup>. Emphasis is placed on the turbulence and mixing characteristics in the different  
 59 regions of the gravity current down the slope. Comparison of the present results with those  
 60 obtained in the laboratory by Odier, Chen, and Ecke<sup>48</sup> and by Charrondière *et al.*<sup>6</sup> in  
 61 katabatic winds (buoyancy driven down slope winds caused by radiative ground cooling)  
 62 is performed. The latter is of particular interest because Reynolds numbers and scales  
 63 are widely different. A comparison of eddy coefficients and mixing lengths of laboratory  
 64 currents with field measurement therefore requires the determination of the appropriate  
 65 scaling parameters. In this respect the present laboratory results and their analysis sheds  
 66 new light on katabatic wind mixing behavior. Furthermore, most of the experimental data  
 67 of katabatic winds have been obtained in a limited region above the maximum-wind-speed  
 68 height where mixing lengths increase with height. Thus, laboratory results can shed new  
 69 light on katabatic wind mixing behaviour.

70 The paper is organized as follows: the essential details of the experimental apparatus  
 71 and measurements techniques are given in Sec.II, including a general description of the  
 72 flow development. Results of the mean flow development, mixing properties and Reynolds  
 73 stresses are discussed in Sec.III. A comparison of some mean flow, mixing length and  
 74 eddy coefficients of the present experiments with previous studies<sup>48</sup> and especially with the  
 75 katabatic wind results of Charrondière, Hopfinger, and Brun<sup>1</sup> is presented in Sec.IV. Sec.V  
 76 summarizes the results and includes concluding remarks.

## 77 II. EXPERIMENTAL DESIGN

78 The experiment, sketched in figure 1a and described in detail elsewhere<sup>33,34</sup>, consists of  
 79 a saline gravity current initiated by injecting a constant flow rate  $Q_0$  characterized by a  
 80 constant initial velocity  $U_0$  upstream of a 25cm wide (b) and 160cm long horizontal channel  
 81 within a lighter ambient fluid (ethanol solution for refractive index matching). The hori-  
 82 zontal channel is followed by a hyperbolic tangent profiled slope boundary (cf. figure 1b),  
 83 defined as:

$$84 \quad y = \frac{h_c}{2}(1 - \tanh(x)), \quad \theta = \operatorname{atan}\left(-\frac{h_c}{2}(1 - \tanh(x^2))\right) \quad (1)$$

85 No return flow and a constant total water depth of  $h = 20 \pm 0.5$ cm in the initial horizontal  
 86 channel were assured by evacuating the same volume as supplied at the downstream end of  
 88 the experimental channel. The corresponding hydraulic initial conditions are summarized

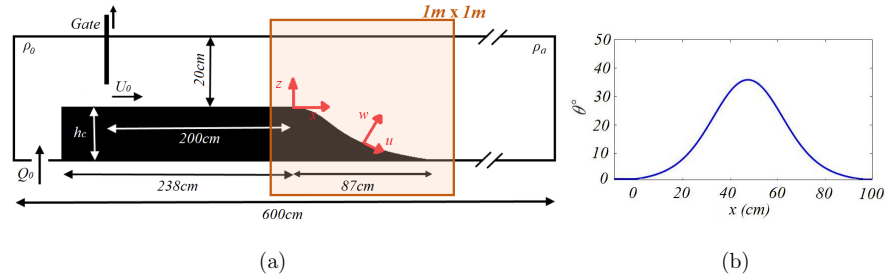


FIG. 1. a) Schematic side-view of the tank used to perform laboratory experiments with the main geometrical features and the notations. The orange rectangular box is the PIV acquisition windows of size 1m1m located in the centre of the slope. b) Slope angle evolution along the  $x$  (down slope) direction.

89 in table 1 and are expressed in terms of initial flow rate per unit width  $q_0 = Q_0 b$ , initial  
 90 reduced gravity  $g'_0 = g(\Delta\rho\rho_a)$ , inlet Reynolds number  $Re_0 = q_0\nu$ , where  $\nu$  is the kinematic  
 91 viscosity, and initial buoyancy flux  $B_0 = q_0 g'_0$ .

92 Fig.2 presents one series of snapshots of one experiment with dye added in the saline  
 93 water at  $t_0 = 100s$  ( $D5_2$ , cf. table I) after the current has reached stationary conditions (i.e.  
 94 after the initial passage of the gravity current head). Two different types of shear instabilities  
 95 at the interface between the dense flow and the ambient fluid can be recognized: Holmboe  
 96 instability (HI)<sup>49</sup> near slope begin, followed by Kelvin–Helmholtz instabilities (KHI) on the  
 97 steepest part of the slope. The final portion and the downstream part of the slope are  
 98 characterized by the collapse of the KHIs which generate a turbulent (mixed) shear layer  
 99 (TSL) with an intermediate upper density layer.

101 A total of 12 experiments have been performed by varying the initial density difference  
 102  $\Delta\rho$  between the current and the ambient water and  $Q_0$  (see table I). The optical non-  
 103 intrusive experimental technique PIV was adopted to measure the instantaneous velocity  
 104 field in 9 experiments, while the fluorescent dye was added to the saline injected solution  
 105 to determine the local relative density difference in further 3 experiments for evaluating the  
 106 gradient Richardson number (cf. table I).

107 For the PIV measurements, a CCD camera (1200x1600 pixels) was used to acquire the  
 108 experimental images with an acquisition frequency of 23.23Hz. The camera allowed to  
 109 record the whole slope field with an image size of 1m×1m. Each vector of the resulting field

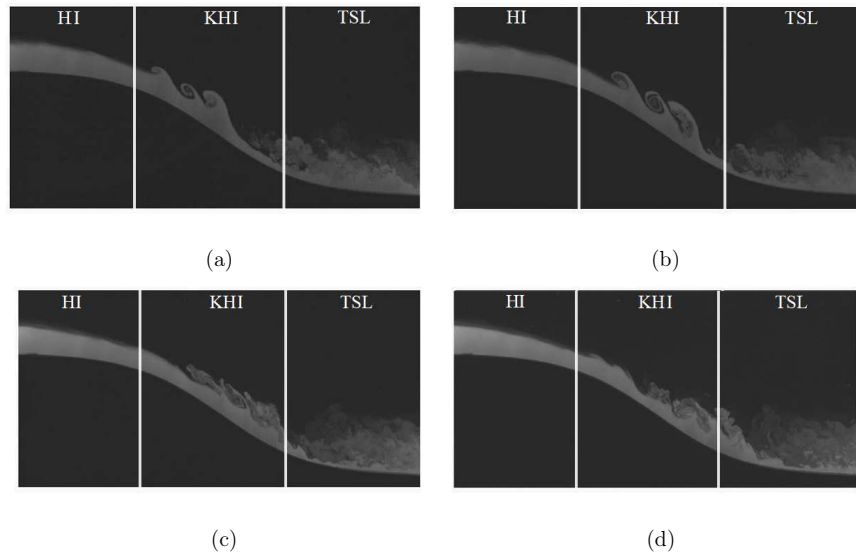


FIG. 2. Instantaneous images of dye visualizations of a gravity current with  $q_0 = 45.76\text{cm}^2\text{s}^{-1}$  and  $g'_0 = 5\text{cm s}^{-2}$ . (a)  $t = t_0$ ; (b)  $t = t_0 + 0.01\text{s}$ ; (c)  $t_0 + 0.02\text{s}$  and (d)  $t_0 + 0.03\text{s}$ . Three different zones can be defined that are characterized by different interface instabilities: Holmboe instability (HI) near slope begin, Kelvin-Helmholtz instability (KHI) at steep slope and the final area of KHI collapse to a turbulent (mixed) shear layer (TSL).

110 represents an area of approximately  $0.23\text{cm} \times 0.23\text{cm}$ . Further details on the PIV procedure  
 111 are given in Martin, Negretti, and Hopfinger<sup>34</sup>.

112 To estimate relative averaged density profiles, a local calibration procedure taking into  
 113 account the light absorption of Rhodamine 6G added to the injected saline water has been  
 114 adopted. Details of the procedure can be found in Negretti, Zhu, and Jirka<sup>50</sup>.

### 115 III. EXPERIMENTAL RESULTS

#### 116 A. Mean flow development and entrainment

117 The along-slope mean velocity  $u$  and slope normal velocity  $w$  have been measured at  
 118 three downstream positions  $x$  and are processed in experiments  $R5_2$ ,  $R15_2$  and  $R15_3$  that  
 119 are representative of all the experiments conducted. These show how a change in  $g'_0$  and  $q_0$

TABLE I. Parameters of the experiments conducted, where  $q_0$  is the dense flow rate per unit width,  $g'_0$  the reduced gravity,  $Re_0 = q_0/\nu$  is the inlet Reynolds number,  $B_0 = q_0 g'_0$  is the initial buoyancy flux and  $h_{0i}$  is the initial height of the dense current in the horizontal part of the channel. In the Run expression, the number indicates the value of the reduced gravity  $g'_0$ , while the subscript numbers indicate the three flow rates considered, from the smallest value (1) to the largest one (3).

Run	$q_0(\text{cm}^2\text{s}^{-1})$	$g'_0(\text{cm s}^{-2})$	$Re_0$	$B_0(\text{cm}^3\text{s}^{-3})$	$h_{0i}(\text{cm})$
$R5_1$	32.28	5	3200	160	6
$R5_2$	45.76	5	4600	225	6.7
$R5_3$	57.24	5	5700	280	7.5
$R10_1$	32.28	10	3200	320	5.8
$R10_2$	45.76	10	4600	460	6.3
$R10_3$	57.24	10	5700	570	7
$R15_1$	32.28	15	3200	485	5.7
$R15_2$	45.76	15	4600	685	6
$R15_3$	57.24	15	5700	860	6.4
$D5_1$	32.28	5	3200	160	6
$D5_2$	45.76	5	4600	225	6.7
$D5_3$	57.24	5	5700	280	7.5

120 affect the flow. As in Negretti, Flòr, and Hopfinger<sup>33</sup> and Martin, Negretti, and Hopfinger<sup>34</sup>,  
 121 the flow distance  $x$  has been normalized by  $h_{0i}$ , the initial mean height of the dense current  
 122 at slope begin, i.e.  $x^* = x/h_{0i}$ .

123 For each experiment 4200 frames with an acquisition frequency of 23.23Hz have been  
 124 recorded. For temporal average, 2000 frames between 1500 and 3500 considering only the  
 125 steady flow regime, i.e. after the current head has passed  $<1500$  and before of the mixed  
 126 layer develops changing the initial ambient conditions  $>3500$ .

127 Fig.3 shows time-averaged along-slope velocity  $\langle u \rangle$  and slope normal velocity  $\langle w \rangle$  at three  
 128 positions  $x^* = 1$ ,  $x^* = 7$  and  $x^* = 11$  indicated by the continuous vertical black lines in  
 129 Fig.3a. Upstream of the slope, the current has a constant  $\langle u \rangle$  as long as the change in the  
 130 bottom inclination does not affect the flow. Then,  $\langle u \rangle$  increases until KHI develop, which  
 131 cause the slow down of the current followed by a nearby maximum constant velocity, which

132 is reached from  $x^* \approx 7$  as seen the in the insets in Fig.4.

133 Fig.3b-d show the  $\langle u \rangle$  velocity profile and Fig.3c-g the slope normal velocity distribution  
 134  $\langle w \rangle$  at  $x^* = 1$  (a,d),  $x^* = 7$  (b,e) and  $x^* = 11$  (c,f). The different symbol colors indicate  
 135 different experiments, while the symbol shape refers to the position  $x^*$ .

136 In Fig.3a-c all the experiments show velocity profiles  $\langle u \rangle$  similar to that of a plane turbu-  
 137 lent wall jet<sup>51</sup> as has also been observed by Buckee, Kneller, and Peakall<sup>52</sup> and Ottolenghi  
 138 *et al.*<sup>53</sup>. The height where maximum velocity occurs is conditioned by interfacial drag. The  
 139 maximum velocity moves closer to the bottom as  $x^*$  increases. Fig.3d-f shows the time-  
 140 average vertical velocity  $\langle w \rangle$ . At  $x^* = 1$   $\langle w \rangle$  is negative from the slope bottom up to the  
 141 shear layer where it tends to zero. The behaviour is opposite at  $x^* = 7$ , where the slope  
 142 is steepest with  $\langle w \rangle$  being negative in the outer part of the current and in the ambient  
 143 fluid. Further downstream at  $x^* = 11$   $\langle w \rangle$  weakly decreases with increasing  $z$ . The negative  
 144 value of vertical velocity  $w$  in the boundary region at  $x^* = 1$  is due to the boundary layer  
 145 thinning due to acceleration and in the shear zone the negative value indicates entrainment.  
 146 At  $x^* = 7$ , the large negative values of  $\langle w \rangle$  in the shear zone indicate large entrainment  
 147 with the larges negative value in the outer part of the shear zone. At  $x^* = 11$  weak negative  
 148 values of  $\langle w \rangle$  indicate weak entrainment.

149 In order to highlight more clearly the change in flow structure with downstream distance  
 150 it is of interest to present velocities in dimensionless form. Fig.4 shows the variation along  
 151  $z/z_{0.5}$  of the dimensionless longitudinal velocity  $\langle u \rangle / \langle u_m \rangle$  (symbols outlined in blue) and of  
 152 the normal component  $\langle w \rangle / \langle u_m \rangle$  (symbols outlined in black) for experiments  $R5_2$  (a) and  
 153  $R15_3$  (b), where  $\langle u_m \rangle$  is the maximum mean velocity, shown in the insets, and  $z_{0.5}$  is the  
 154 distance from the boundary where the velocity  $\langle u \rangle$  is  $\langle u_m \rangle / 2$ . The maximum mean velocity,  
 155  $\langle u_m \rangle$ , and  $z_{0.5}$  are shown in blue and orange respectively in the insets at the top right in  
 156 Fig.4(a) and (b). Both experiments show a similar trend of  $z_{0.5}$  and  $\langle u_m \rangle$ . In accordance  
 157 with what was mentioned already above, it can be seen (compare insets) that higher  $g'_0$  and  
 158  $q_0$  lead to a higher  $\langle u_m \rangle$ , which increases along  $x^*$  until it reaches an almost constant value  
 159 at  $x^* > 7$ . The change in  $z_{0.5}$  is more complex. Upstream of the slope,  $z_{0.5}$  is nearly constant  
 160 while at slope begin first decreases and then increases smoothly in the deepest part of the  
 161 slope due to the formation of KHI. Toward the end of the slope there is a rapid decrease  
 162 of  $z_{0.5}$  toward a constant value. As expected, the dimensionless velocity distributions and  
 163 values are practically the same in experiments  $R5_2$  and  $R15_3$ .



This is the author's peer reviewed, accepted manuscript. However, the online version of record will be different from this version once it has been copyedited and typeset.

PLEASE CITE THIS ARTICLE AS DOI: 10.1063/5.0132830

Accepted to Phys. Fluids 10.1063/5.0132830

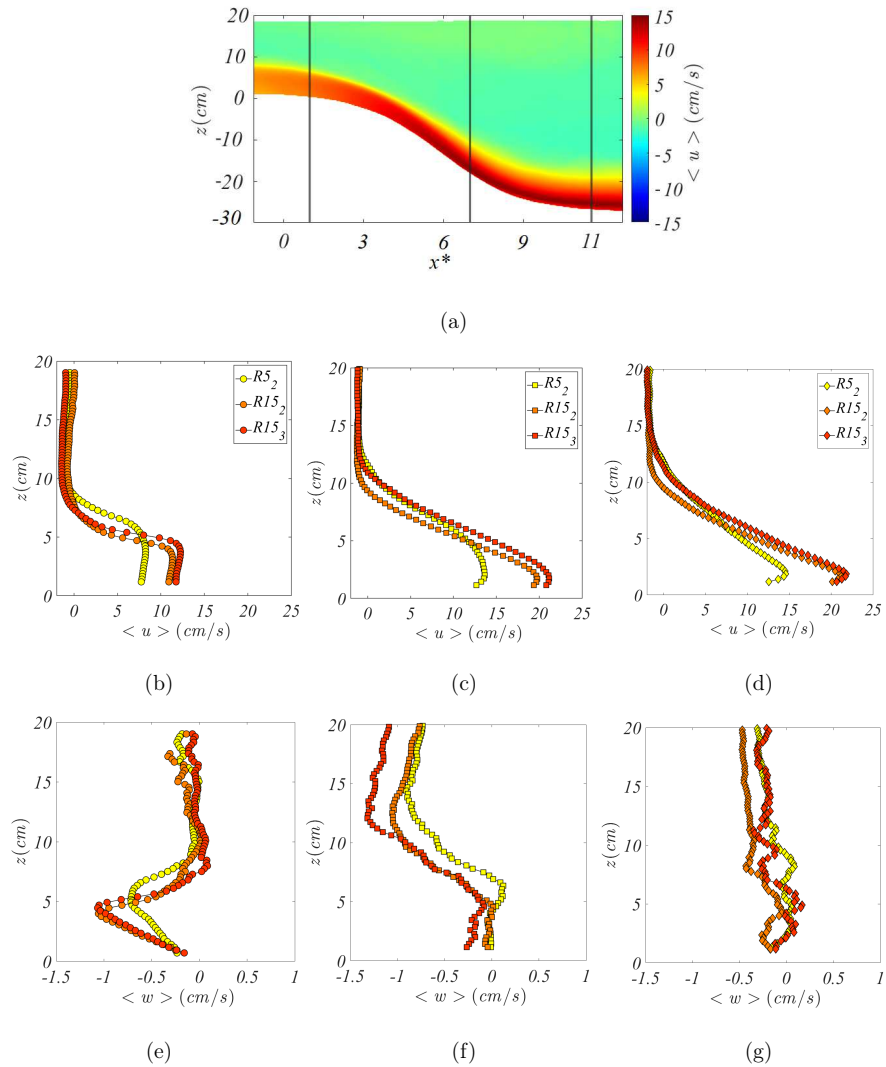


FIG. 3. (a) Color plot of the time-averaged along-slope velocity  $\langle u \rangle$  vs  $x^*$  for  $R15_2$ . The vertical solid lines indicate the positions  $x^* = 1$ ,  $x^* = 7$  and  $x^* = 11$  where the time averaged streamwise velocity profiles  $\langle u \rangle$  and the vertical velocity  $\langle w \rangle$  have been measured for experiments  $R5_2$  (b-e),  $R15_2$  (c-f) and  $R15_3$  (d-g) respectively.

This is the author's peer reviewed, accepted manuscript. However, the online version of record will be different from this version once it has been copyedited and typeset.

PLEASE CITE THIS ARTICLE AS DOI: 10.1063/5.0132830

Accepted to Phys. Fluids 10.1063/5.0132830

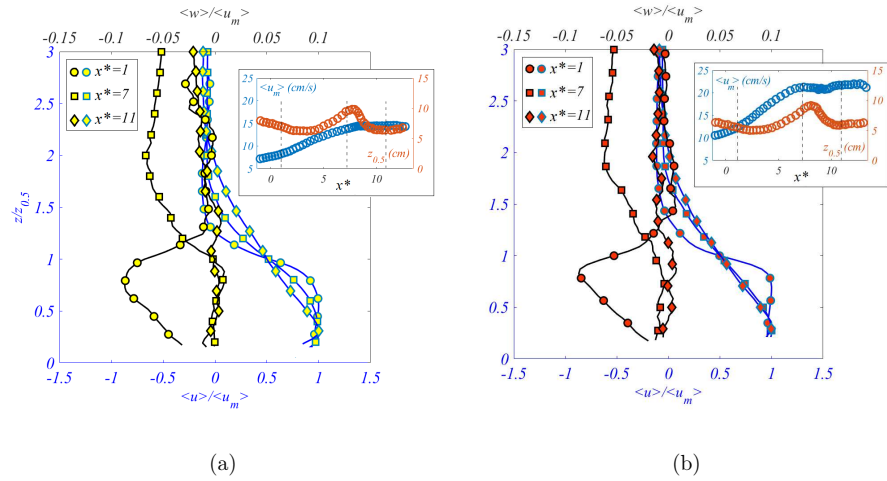


FIG. 4. Dimensionless profiles of the averaged streamwise velocity  $\langle u \rangle / \langle u_m \rangle$  and vertical velocity  $\langle w \rangle / \langle u_m \rangle$  for the experiments  $R5_2$  (a) and  $R15_3$  (b). The insets show time-average maximum values of the streamwise velocity component  $\langle u_m \rangle$  in blue and the  $z_{0.5}$  in red with the vertical continuous lines indicating the positions  $x^* = 1, 7$  and  $11$ .

165 Calculating entrainment is of interest because it expresses mixing with the ambient fluid,  
 166 related with interfacial instability, and interfacial drag. Following Morton, Taylor, and  
 167 Turner<sup>54</sup>, entrainment of ambient fluid is related with the normal velocity  $w_h$  at the interface  
 168 with the entrainment coefficient defined by:

$$169 \quad E_w = -\frac{w_h}{U}, \quad (2)$$

170 where  $U$  is the depth integrated velocity of the current. A cross-stream location  $z/z_{0.5} \approx 1.5$   
 171 has been chosen as the interface. Then, the velocity  $w_h$  at this location has been obtained  
 172 from the PIV velocity data (Fig 3 and 4) by taking the average of three values of the normal  
 173 velocity around  $z/z_{0.5} = 1.5$ . Invariance of the results has been checked by comparison be-  
 174 tween results obtained directly from averaged velocity fields and from instantaneous velocity  
 175 fields. We note that, as already reported by Odier, Chen, and Ecke<sup>37</sup> and Martin, Negretti,  
 176 and Hopfinger<sup>34</sup> this definition of entrainment coefficients gives values somewhat larger than  
 177 those obtained with the definition using the volume flux change in the downstream direction,  
 178  $E_q = 1/Ud(Uh)/dx$  (cf. also Fig. 6).

This is the author's peer reviewed, accepted manuscript. However, the online version of record will be different from this version once it has been copyedited and typeset.

PLEASE CITE THIS ARTICLE AS DOI: 10.1063/5.0132830

Accepted to Phys. Fluids 10.1063/5.0132830

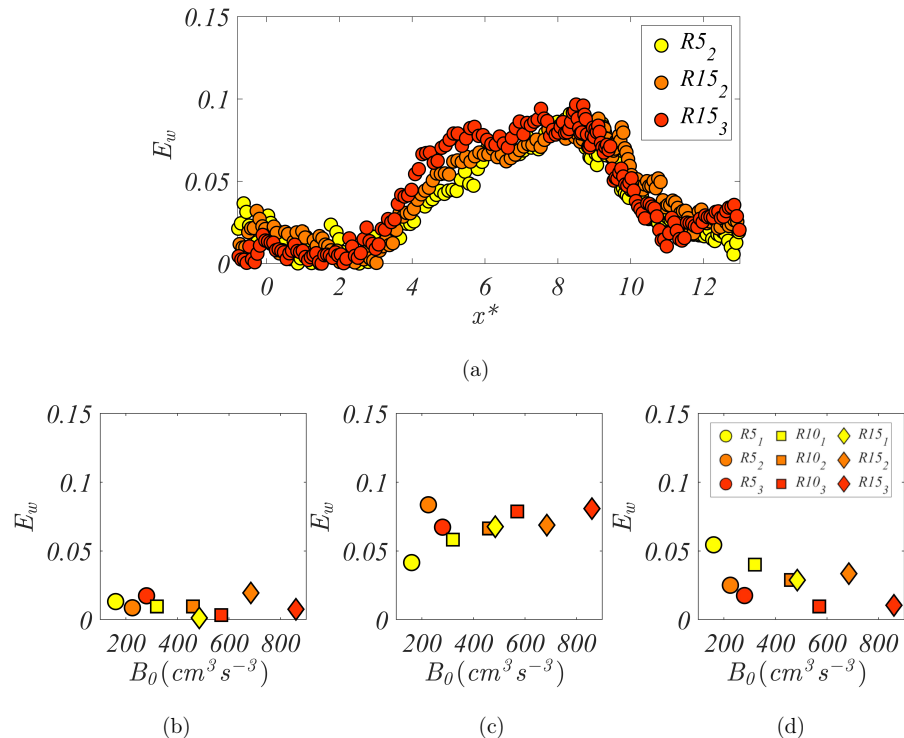


FIG. 5. a) Time-averaged entrainment coefficients  $E_w$  versus  $x^*$  for experiments  $R5_2$ ,  $R15_2$  and  $R15_3$ . Entrainment coefficient  $E_w$  versus initial buoyancy flux  $B_0$ , at  $x^* = 1$  (b),  $x^* = 7$  (c) and  $x^* = 11$  (d) for all performed experiments.

179 Fig.5a shows the time-averaged entrainment coefficients  $E_w$  versus  $x^*$  for  $R5_2$ ,  $R15_2$  and  
 180  $R15_3$  experiments. Despite the different initial conditions,  $E_w$  shows a similar behavior in  
 181 all experiments. The entrainment rates are almost zero during the initial acceleration phase  
 182 ( $0 < x^* < 2$ ) and increase rapidly as KHI develop to reach maximum values at the steepest  
 183 part of the slope ( $x^* \approx 7$ ) and then decreases again in the TSL region. Figs 5 (b-d) show  
 184 the entrainment  $E_w$  evaluated at  $x^* = 1$  (b), slope angle about  $2^\circ$ ,  $x^* = 7$  (c), slope angle  
 185 about  $30^\circ$  and  $x^* = 11$ (d), slope angle about  $5^\circ$ , as a function of initial buoyancy flux  $B_0$ .  
 186 This highlights further the strong dependency of entrainment on slope angle whereas any  
 187 variation of  $E_w$  with initial buoyancy flux does not present any clear trend.

188 In Fig.6 the entrainment coefficient  $E_w$  and  $E_q$  are plotted as a function of the local

189 Froude number  $Fr = Ri_g^{-0.5}$  and compared with other experimental data. The present data  
 190 are for the range  $0.5 < x^* < 1.5$ ,  $6.5 < x^* < 7.5$  and  $10.5 < x^* < 11.5$  and for experiments in  
 191 which both velocity and density field measurements are available. To compute the Froude  
 192 number, the gradient Richardson number  $Ri_g = N^2 \cos \theta / S^2$  ( $Fr = 1/\sqrt{Ri_g}$ ) has been used,  
 193 where  $N = \sqrt{-g \langle \partial_z \rho \rangle / \langle \rho \rangle}$  and  $S = \langle \partial_z u \rangle$  represent the Brunt-Väisälä frequency and the  
 194 vertical shear of velocity, respectively. We see that the data of the present study are in good  
 195 agreement with those of previous studies.

## 196 B. Reynolds stresses

197 Key quantities for describing turbulence processes are the Reynolds stresses expressing  
 198 turbulent transport of momentum<sup>60</sup>. Fig.7 displays the variation with  $z/z_{0.5}$  of the time  
 199 averaged Reynolds stresses  $\langle u'u' \rangle / \langle u_m^2 \rangle$ , (a,b) and of  $\langle w'w' \rangle / \langle u_m^2 \rangle$  (c,d) at  $x^* = 7$  and  $x^* = 11$   
 200 for experiments  $R5_2$ ,  $R15_2$  and  $R15_3$ .

201 The maximum values of the normal Reynolds stresses  $\langle u'u' \rangle / \langle u_m^2 \rangle$  and  $\langle w'w' \rangle / \langle u_m^2 \rangle$  at  
 202  $x^* = 7$  have a near Gaussian distribution and are located close to  $z/z_{0.5} = 1$  (see Fig.7a,c).  
 203 In the experiments with larger density difference ( $R15_{2,3}$ ), the values are lower and more  
 204 spread out.

205 In experiment  $R5_2$  the profile above maximum velocity is similar to that of a mixing layer  
 206 i.e. of erf type<sup>61</sup>, whereas when  $g'_0$  is larger, higher acceleration due to larger gravitational  
 207 force, gives rise to a wider region of nearly constant shear and consequently constant normal  
 208 stresses. Stratification has practically no effect on Reynolds stresses at  $x^* = 7$ , the gradient  
 209 Richardson number being small (of order 0.1). At  $x^* = 11$  a region of nearly constant  
 210 shear exists in all three experiments, hence nearly constant normal stresses over this region.  
 211 Maximum values of the Reynolds stresses are about half of those at  $x^* = 7$  due to the  
 212 collapse of KHIs and re-stratification process that takes place at the end of the slope.

213 The Reynolds shear stresses  $\langle u'w' \rangle$  are shown in Fig. 8, with the instantaneous two-  
 214 dimensional field of the scaled Reynolds shear stresses  $\langle u'w' \rangle$  along  $x^*$ , of experiment  $R5_2$ ,  
 215 presented in Fig. 8a. As previously observed<sup>34</sup>, in the HI region the largest fluctuations  
 216 are concentrated at the sheared interface only. As the current develops down the slope, an  
 217 increase of the shear stresses is observed due to acceleration and rapid onset of the KHI,  
 218 which spread over the full current depth: large values of  $\langle u'w' \rangle / \langle u_m^2 \rangle$  characterize the full  
 219

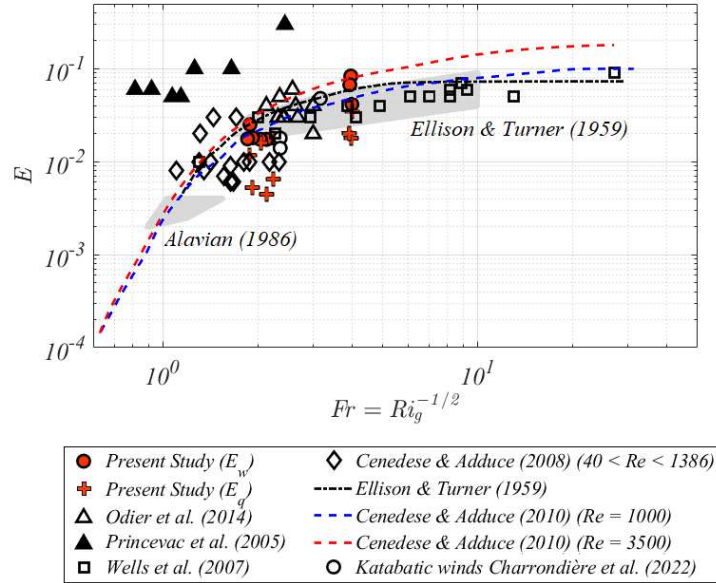


FIG. 6. Entrainment coefficients,  $E_w$  (red  $\circ$ ), and  $E_q$  (red  $+$ ) as a function of the local Froude number  $Fr = Ri_g^{-1/2}$ . Present entrainment coefficients are for the range  $0.5 < x^* < 1.5$ ,  $6.5 < x^* < 7.5$  and  $10.5 < x^* < 11.5$  of all experiments with  $g'_0 = 5\text{cm s}^{-2}$ . Data of  $E_w$  from Odier, Chen, and Ecke<sup>37</sup>, Princevac, Fernando, and Whiteman<sup>55</sup>, Wells, Cenedese, and Caulfield<sup>56</sup>, Cenedese and Adduce<sup>57</sup> and Charrondière *et al.*<sup>6</sup> (katabatic winds in situ measurements) are included for comparison. Shaded areas represent laboratory experiments of Alavian<sup>58</sup> and Ellison and Turner<sup>26</sup> with the black dashed line representing the classical variation of Ellison and Turner<sup>26</sup> and the dashed blue and red lines the variation as reported in Cenedese and Adduce<sup>59</sup>.

220 shear layer with the largest values on the steepest part of the slope at  $x^* = 7$  where  $\theta = 31^\circ$ .  
 221 This is highlighted in Fig.8b and Fig.8c where scaled Reynolds shear stress profiles, computed  
 222 at  $x^* = 7$  and  $x^* = 11$ , respectively, are reported. In accordance with the behaviour of the  
 223 normal stresses, at  $x^* = 7$  there is a clear maximum in experiment  $R5_2$ , located at the  
 224 sheared interface close to  $z/z_{0.5} = 1$  whereas when  $g'_0$  is larger, maximum values are lower  
 225 and spread out. Furthermore, at  $x^* = 11$  where there is a general decrease of the turbulent

This is the author's peer reviewed, accepted manuscript. However, the online version of record will be different from this version once it has been copyedited and typeset.

PLEASE CITE THIS ARTICLE AS DOI: 10.1063/5.0132830

Accepted to Phys. Fluids 10.1063/5.0132830

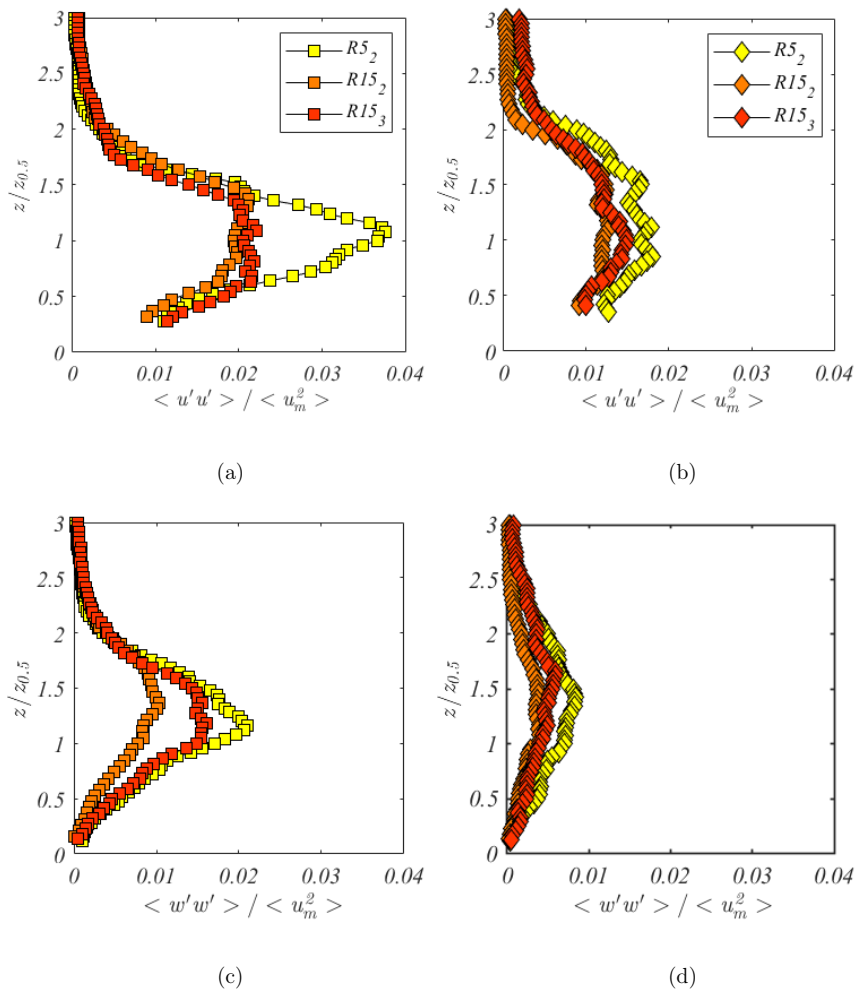


FIG. 7. Scaled normal Reynolds stress profiles determined at  $x^* = 7$  (a,c) and  $x^* = 11$  (b,d) in experiments  $R5_2$ ,  $R15_2$  and  $R15_3$ .

fluctuations, the shear stress values are less than half of those at  $x^* = 7$ .

Odier, Chen, and Ecke<sup>48</sup> proposed a novel method for characterizing the distribution of correlations of the velocity fluctuations to better understand the mixing process based on the probability density functions (PDFs) of the momentum fluxes  $\langle u'w' \rangle$ . Fig.9 shows the

This is the author's peer reviewed, accepted manuscript. However, the online version of record will be different from this version once it has been copyedited and typeset.

PLEASE CITE THIS ARTICLE AS DOI: 10.1063/5.0132830

Accepted to Phys. Fluids 10.1063/5.0132830

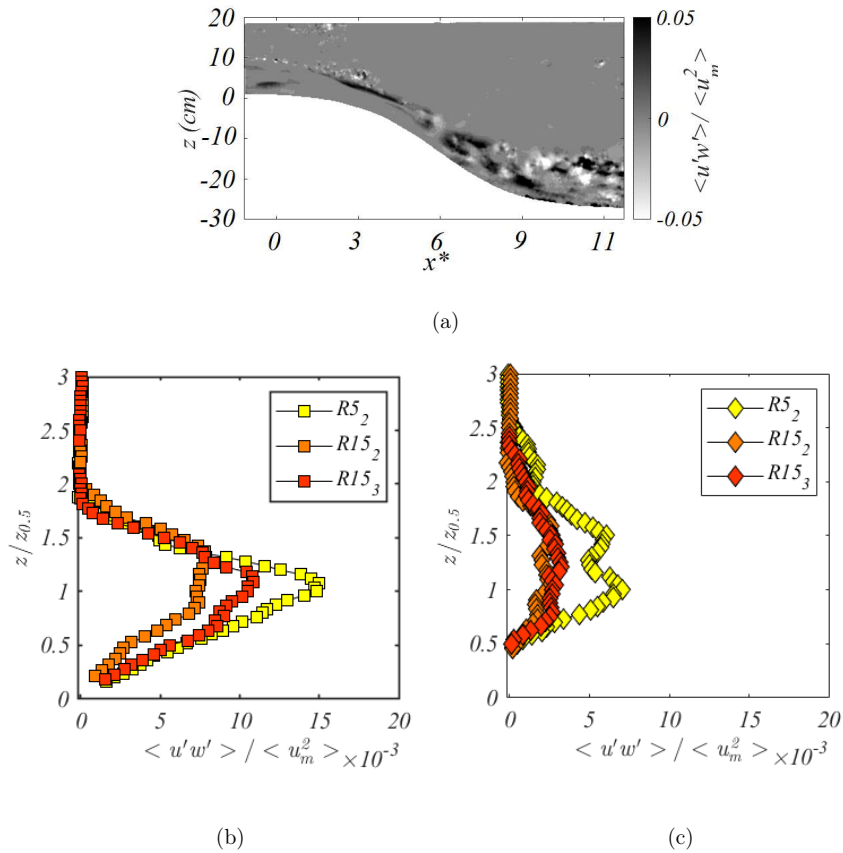


FIG. 8. (a) Scaled instantaneous Reynolds shear stresses  $\langle u'w' \rangle / \langle u_m^2 \rangle$  along  $x^*$  of experiment  $R5_2$ . Profiles of scaled Reynolds shear stresses at  $x^* = 7$  (b) and at  $x^* = 11$  (c) in experiments  $R5_2$ ,  $R15_2$  and  $R15_3$ .

231 PDFs of  $\langle u'w' \rangle$  in the ranges  $5.5 < x^* < 8.5$  and  $8.5 < x^* < 11.5$  of experiment  $R15_2$ . Each  
 232 PDF is obtained using data in a normal band of  $1\text{cm}$  height, starting from the bottom of  
 233 the slope, and is highlighted with a different color enabling to see the evolution of the PDFs  
 234 as the vertical distance increases.

236 As also seen in Fig. 8, the fluxes reach nearly 2% of the squared maximum velocity flow  
 237 so as there is still a probability ( $10^{-3}$ ) that a fluctuation will reach a value about 15 times the  
 238 mean (Fig.9). Usually, as the center of the mixing region is approached, i.e. the interface

This is the author's peer reviewed, accepted manuscript. However, the online version of record will be different from this version once it has been copyedited and typeset.

PLEASE CITE THIS ARTICLE AS DOI: 10.1063/5.0132830

Accepted to Phys. Fluids 10.1063/5.0132830

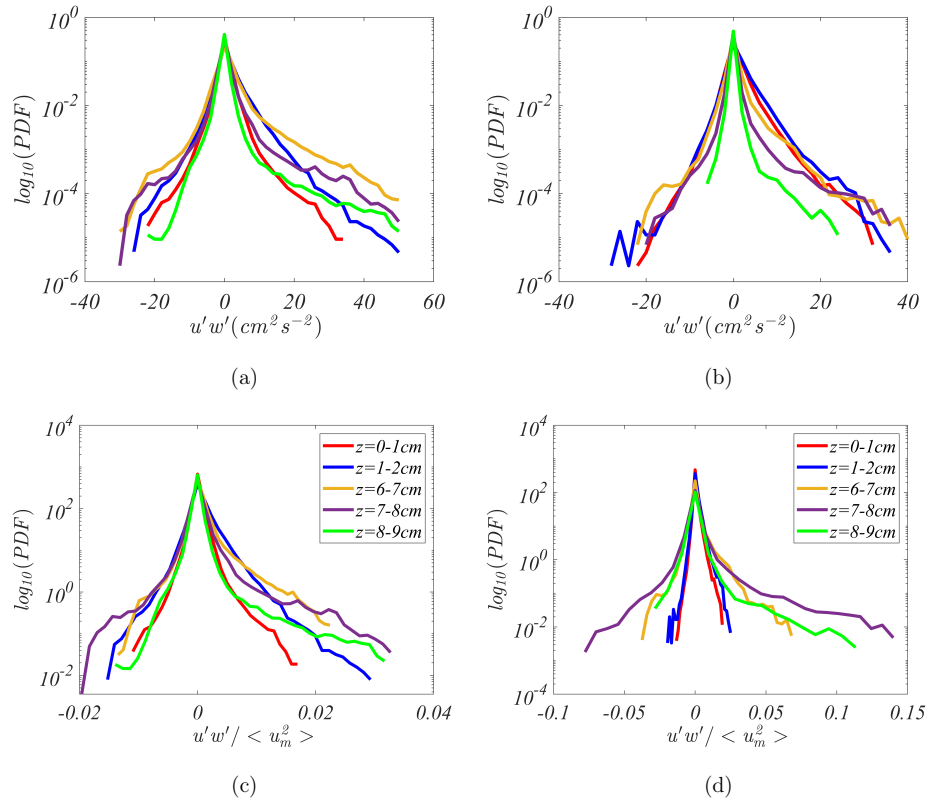


FIG. 9. PDFs of instantaneous shear stress (a,b), and of scaled shear stress (c,d) in  $R15_2$  experiment. Each PDF is constructed using data in a band of 1cm height from the bottom (normal position indicated in the legend), situated at  $5.5 < x^* < 8.5$  (a,c) and TSL area at  $8.5 < x^* < 11.5$  (b,d)

239 between the current and the ambient fluid, large fluctuations are present and the PDFs  
 240 of the momentum fluxes are asymmetric<sup>48</sup> as highlighted in figure 9 (a,c) and in accord  
 241 with previous observations of Odier, Chen, and Ecke<sup>48</sup>. This asymmetry is the origin of  
 242 the non-zero mean value of the fluxes indicating either downward transport (entrainment)  
 243 of downstream momentum or upward transport of upstream momentum, according to the  
 244 mixing mechanism induced by the KHI. This asymmetry weakens when reaching the TSL  
 245 zone as a results of the restratification process issued by the collapse of the KHI.



246 **C. Mixing length and shear scale**

247 Reynolds stresses can be conceptually parameterised by an eddy or turbulent viscosity,  
 248  $K_m = -\langle u'w' \rangle / \partial_z u$ , that relates chaotic fluid motion to diffusive type processes<sup>44,61</sup>. It is a  
 249 useful parameter for indicating the extent of internal mixing and is used extensively in both  
 250 numerical and analytical modelling of turbulent flows.

251 Based on the mixing length model proposed by Prandtl<sup>62</sup>, the Reynolds stresses  $\langle u'w' \rangle$   
 252 can also be related to the square of the velocity gradient  $\langle \partial_z u \rangle^2$  using a proportionality  
 253 constant which represents a mixing length  $L_m$ :

$$254 \quad L_m^2 = \frac{\langle u'w' \rangle}{\langle \partial_z u \rangle^2}, \quad (3)$$

255 Fig.10 shows the computed vertical profiles of the turbulent eddy diffusivity  $K_m$  (a,b)  
 256 and mixing lengths  $L_m$  (c,d) at  $x^* = 7$  and  $x^* = 11$  (left and right columns, respectively).  
 257 The corresponding  $z$  variation of mean velocity gradients  $\partial_z u$  are presented in the insets.  
 258 Data close to the bottom and top extremities are not reported because experimental errors  
 259 become large.  $L_m$  is computed starting at a distance from the wall of approximately 20% of  
 260 the current depth<sup>61</sup>.

261 At  $x^* = 7$  (Fig.10c), mixing lengths  $L_m$  are nearly constant in experiments  $R15_2$  and  
 262  $R15_3$ , while eddy coefficients increase and then decrease with distance  $z$  (Fig.10a). When  
 263 density differences are lower ( $R5_2$ ), both,  $L_m$  and  $K_m$  behave differently in the lower part  
 264 because of the difference in velocity gradient. In general, close to the velocity maximum and  
 265 at large distances from the bottom, the vertical derivative  $\partial_z u$  becomes almost zero, so that  
 266 large fluctuations in the calculated  $L_m$  occur at these extremities. Averaging over the depth  
 267 and the downstream distance in the considered region, gives a mean value of  $L_m \approx 0.60 \pm 0.1$ ,  
 268 which compares well with those reported by Odier *et al.*<sup>41</sup> of  $L_m \approx 0.45 \pm 0.1$ .

269 At the end of the slope in the TSL region ( $x^* = 11$ ) (Fig.10b,d) the values of  $L_m$  and of  
 270  $K_m$  are lower and both increase almost linearly with  $z/z_{0.5}$ . This is probably related with  
 271 the substantially lower and nearly constant Reynolds stresses at this location.

272 In order to understand how mixing lengths and eddy coefficients depend on the effect of  
 273 turbulent kinetic energy, of stable stratification, and of destabilization by shear it is useful  
 274 to determine the shear scale  $L_s$ , also referred to as Corrsin scale<sup>63</sup>, and the buoyancy length  
 275 (Ozmidov scale)  $L_o$ , which are defined as<sup>37,64</sup>:

This is the author's peer reviewed, accepted manuscript. However, the online version of record will be different from this version once it has been copyedited and typeset.  
 PLEASE CITE THIS ARTICLE AS DOI: 10.1063/5.0132830

Accepted to Phys. Fluids 10.1063/5.0132830

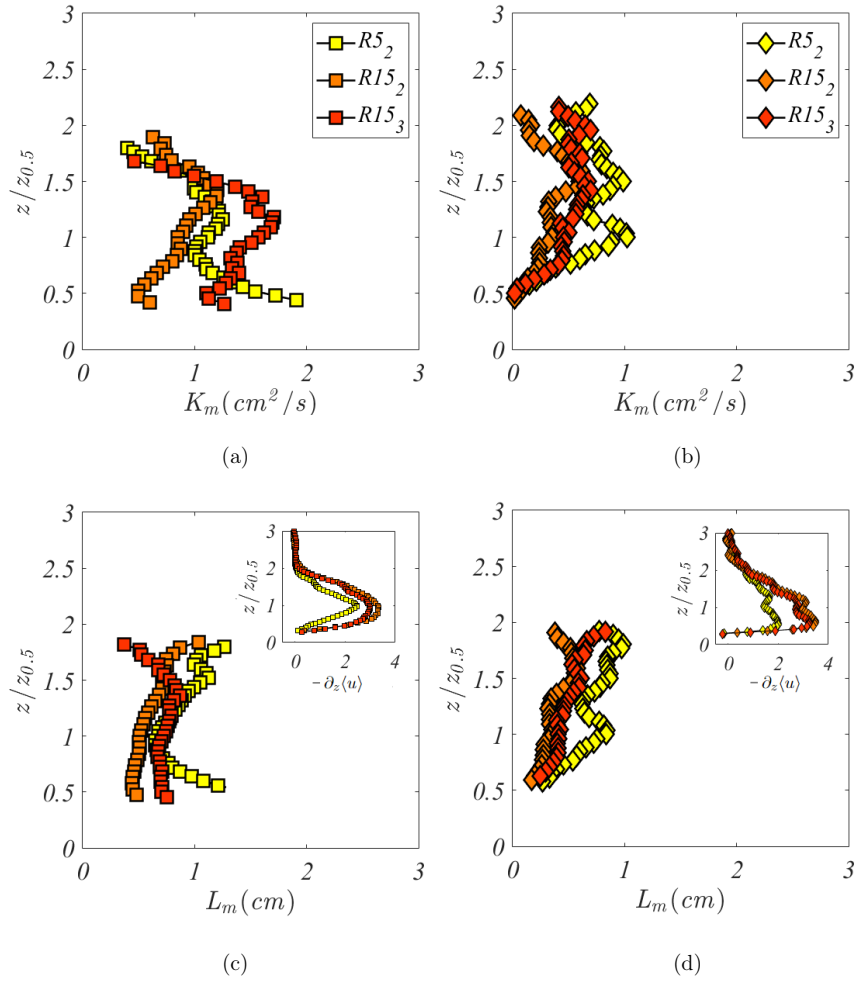


FIG. 10. Variations of eddy coefficient  $K_m$  and mixing lengths  $L_m$  with  $z/z_{0.5}$  at  $x^* = 7$ , (a,c) and at  $x^* = 11$ , (b,d). Close to the velocity maximum, as well as far away from it, the  $\partial_z(u)$  tend to vanish, producing large fluctuations in  $K_m$  and  $L_m$ . The insets show the velocity gradients  $\partial_z(u)$  as a function of  $z/z_{0.5}$ .

$$L_s = \sqrt{\frac{\bar{\epsilon}}{\left(\overline{\langle \partial_z u \rangle}\right)^3}}, \quad L_o = \sqrt{\frac{\bar{\epsilon}}{\left(g \frac{\overline{\langle \partial_z \rho \rangle}}{\overline{\langle \rho \rangle}}\right)^{3/2}}, \quad (4)$$

where  $\overline{\langle \cdot \rangle}$  represents a time average over the experimental duration and  $\bar{\epsilon}$  the mean turbulent dissipation rate. As already pointed out by Odier, Chen, and Ecke<sup>48</sup>, the smaller of these scales limits the mixing length  $L_m$ , hence, also  $K_m$ . The strength of stratification with respect to the shear is measured by the (gradient) Richardson number  $Ri_g$  which also relates these two scales via the relation  $L_s/L_o = Ri_g^{3/2}$ . Generally, gravity currents on slopes are characterized by low Richardson numbers  $Ri_g \ll 1$ , hence shear dominates over stratification so that the shear scale  $L_s$  is expected to limit the mixing length  $L_m$  and  $K_m$ .

According to Kolmogorov's similarity hypothesis, the dissipation is the only flow variable that characterizes the state of turbulence when stratification is weak. The significance of  $\epsilon$  has been extensively addressed in numerous studies<sup>65-67</sup>. Following Steinbuck *et al.*<sup>68</sup> and Xu and Chen<sup>67</sup> the dissipation rate can be estimated using the four resolved velocity gradients obtained by PIV as:

$$\epsilon = \nu \langle 4(\partial_x u')^2 + 4(\partial_z w')^2 + 3(\partial_z u')^2 + 3(\partial_x w')^2 + 4(\partial_x u' \partial_z w') + 6(\partial_z u' \partial_x w') \rangle \quad (5)$$

In a stratified flow the dissipation is equal to production minus the loss of energy to buoyancy. In a flow on a slope there is, in addition to shear production, also TKE production by buoyancy. Neglecting advection and diffusion terms, the TKE energy balance is given by:

$$-\overline{u'w'} \frac{\partial u}{\partial z} - \frac{g \overline{w'\rho'}}{\rho} \cos \theta + \frac{g \overline{u'\rho'}}{\rho} \sin \theta \approx \epsilon \quad (6)$$

The turbulent momentum flux  $\overline{u'w'}$  is positive in the region of the dense flow, while the gradient velocity  $\partial u/\partial z$  has the opposite sign. Their product represents the production of TKE by shear, i.e. the conversion of energy from the averaged flow to TKE.  $(-g)/\rho \overline{w'\rho'} \cos \theta + g/\rho \overline{u'\rho'} \sin \theta$  are, respectively, the loss of TKE to buoyancy and the production of TKE by buoyancy. The buoyancy terms are opposite in sign with the ratio of  $g/\rho \overline{u'\rho'} \sin \theta$  to shear and buoyancy production (i.e. mixing efficiency, which gives the ratio of increase of potential energy to total production) being  $\approx 0.1$  and  $\overline{u'\rho'} \sin \theta / \overline{w'\rho'} \cos \theta \leq 1$  when  $Ri_g < 0.1$ , see Charrondière *et al.*<sup>6</sup>; hence

$$\epsilon \approx \overline{u'w'} \frac{\partial u}{\partial z}. \quad (7)$$

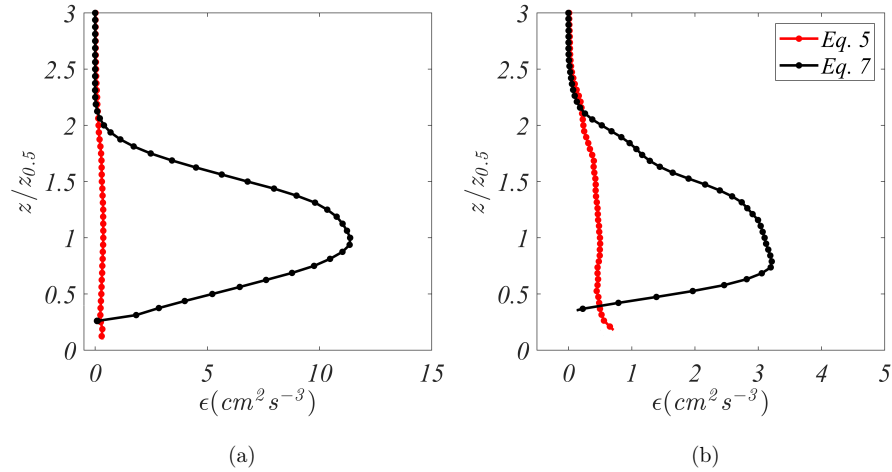


FIG. 11. Vertical profiles of the dissipation rates  $\epsilon$  calculated using equations 5 (red lines) and 7 (black lines) at  $x^* = 7$  (a) and  $x^* = 11$  (b) for the experiment  $R15_2$ .

304 Figure 11 displays the  $z$  variation of the dissipation rates calculated using equations (5) (red  
 305 lines) and (7) (black lines) at  $x^* = 7$  (a) and  $x^* = 11$  (b). The value of  $\epsilon$  computed from  
 306 equation (5) is nearly up to an order of magnitude less than  $\epsilon$  from equation (7).

308 To estimate the dissipation rate  $\epsilon$  directly from the PIV data and avoid important underes-  
 309 timations, it is necessary to have a spatial resolution of the PIV close to the Kolmogorov scale  
 310  $\eta_K$ . The spatial resolution of the present PIV measurements is  $3mm$ , while  $\eta_K = (\nu^3/\epsilon)^{1/4}$   
 311 is of the order of  $\mathcal{O} \sim 0.4mm$  estimated using  $\epsilon = u^3/h^{69}$ . Hence the direct calculation of  
 312  $\epsilon$  from the PIV data using equation (5) will lead to considerable underestimations. As seen  
 313 from the figure 11, the production is maximum near  $z/z_{0.5}$  whereas, because of diffusion  
 314 and advection terms, dissipation is more uniformly distributed across the outer region of the  
 315 current and is close to the average of the production, i.e.:

$$316 \quad \bar{\epsilon} \approx 0.6(\overline{u'w'\partial_z u})_{max}. \quad (8)$$

317 Using equation (8) for the dissipation rate, gives for the shear and Ozmidov scales  $L_s =$   
 318  $0.50 \pm 0.25cm$  and  $L_o = 2.2 \pm 1cm$ , respectively. As expected, for low Richardson numbers  
 319 ( $Ri < 1$ ), the smallest of these two scales is the shear scale  $L_s$  and sets the limit of the  
 320 mixing length  $L_m$ .

321 Fig.12 shows the measured mixing length  $L_m$  versus the computed shear scale  $L_s$  and  
 322  $K_m$  versus  $L_s^2 \partial_z u$  for all the experiments performed. The experimental data of the present  
 323 study all are close to or fall above the dashed straight line in Fig.12 representing  $L_m = L_s$   
 324  $K_m = L_s^2 \partial_z u$ , which is different from the results of Odier, Chen, and Ecke<sup>48</sup> where  $L_m < L_s$ .  
 325 A possible explanation for the difference is the non-constant and much steeper bottom slope  
 326  $\theta$  in the present experiments that can have important consequences on the mixing properties.

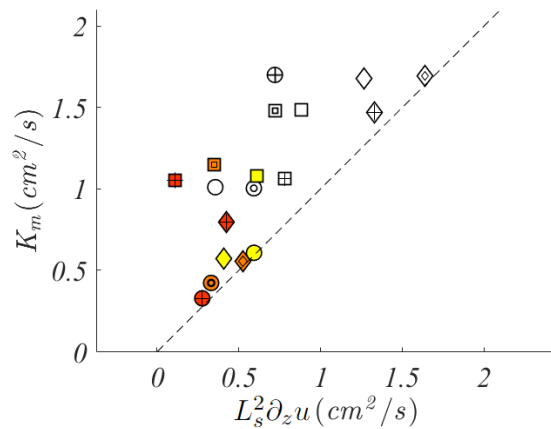
#### 327 IV. COMPARISON WITH KATABATIC WINDS

328 Studies of katabatic winds are numerous (see for instance<sup>4,6</sup>) because these flows affect  
 329 local weather conditions causing also temperature inversion in valleys that are prone to  
 330 pollution. In Antarctica and Greenland, katabatic winds are directly responsible for cooling  
 331 the ocean surface water at the polynya<sup>70</sup> and open sea and play an important role for the deep  
 332 water formation. Katabatic flows are driven by buoyancy supply from the ground (ground  
 333 cooling), whereas in most laboratory currents buoyancy flux is constant and equal to the  
 334 upstream buoyancy supply, hence, the flow structure is expected to be different. A formal  
 335 comparison is, nevertheless, of interest. Ellison and Turner<sup>26</sup> for instance evaluated the mean  
 336 flow development of katabatic winds using their results of a buoyancy conserving gravity  
 337 current on a slope. The recent detailed field measurements by Charrondière *et al.*<sup>6,47,71</sup> on  
 338 steep alpine slopes of 30° inclination (Grand Colon, Belledonne chain) provide an excellent  
 339 data set for comparing katabatic jets data, including turbulent mixing, with laboratory  
 340 gravity currents results. The shape and slope inclination adopted in the present study  
 341 reproduces a typical alpine topography in the French Alps and specifically the Grand Colon  
 342 topography.

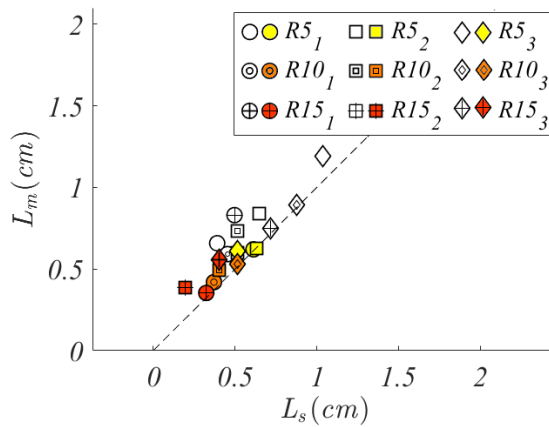
344 Fig.13a shows a comparison of the slope normal katabatic wind mean velocity profile dur-  
 345 ing a representative katabatic event on February 24th 2019 (5h-8h) with a slight up-slope  
 346 wind of velocity  $U_a = -0.2m/s$ , with the  $R15_3$  experimental mean velocity. The errors  
 347 bars on the katabatic velocity profile show the variability of the mean wind during the kata-  
 348 batic event, while the black dashed line represents the fit derived from the Prandtl model<sup>5</sup>.  
 349 The velocity profiles are quite different: indeed in katabatic winds the velocity distribution  
 350 above maximum velocity has a logarithmic trend with maximum gradient close to the ve-  
 351 locity maximum whereas in laboratory experiments the maximum gradient is located near

This is the author's peer reviewed, accepted manuscript. However, the online version of record will be different from this version once it has been copyedited and typeset.  
 PLEASE CITE THIS ARTICLE AS DOI: 10.1063/5.0132830

Accepted to Phys. Fluids 10.1063/5.0132830



(a)



(b)

FIG. 12. Eddy coefficient  $K_m$  versus  $L_s^2 \partial_z u$  (a) and mixing length  $L_m$  versus computed shear length  $L_s$  (b), for all the experiments performed at  $x^* = 7$  (empty markers) and  $x^* = 11$  (filled markers).

352 the current mid-height. The explanation for this difference are the very different density  
 353 distributions, as presented in Fig.13b. In the constant, upstream buoyancy supply of labo-

TABLE II. Characteristic turbulence length scales of present experiments of Odier, Chen, and Ecke<sup>48</sup> and in katabatic flows<sup>1</sup>. The dissipation  $\epsilon$  has been computed using equations (5) and (8).  $\Delta z = \Delta u / \partial_z u_{z_{0.5}}$  is the shear thickness.

Run	$\langle \epsilon \rangle (\text{cm}^2 \text{s}^{-3})$	$L_m (\text{cm})$	$L_s (\text{cm})$	$ \Delta z  (\text{cm})$	$z_{0.5} (\text{cm})$
R15 <sub>2</sub> ( $x^* = 7$ )	6.8	0.61	0.51	6.0	6.8
R15 <sub>2</sub> ( $x^* = 11$ )	1.0	0.38	0.20	7.5	5.6
R15 <sub>3</sub> ( $x^* = 7$ )	9.0	0.75	0.72	7.0	8.0
R15 <sub>3</sub> ( $x^* = 11$ )	2.8	0.55	0.40	9.9	5.9
Charrondière, Hopfinger, and Brun <sup>1</sup>					
$z = 0.66\text{m}$	57	9	21	$11.1 \cdot 10^2$	$3.7 \cdot 10^2$
$z = 0.98\text{m}$	55	16	21	$11.1 \cdot 10^2$	$3.7 \cdot 10^2$
$z = 1.50\text{m}$	52	26	27	$11.1 \cdot 10^2$	$3.7 \cdot 10^2$
$z = 1.93\text{m}$	44	35	32	$11.1 \cdot 10^2$	$3.7 \cdot 10^2$
$z = 2.37\text{m}$	40	45	39	$11.1 \cdot 10^2$	$3.7 \cdot 10^2$
$z = 9.77\text{m}$	46	116	120	$11.1 \cdot 10^2$	$3.7 \cdot 10^2$
Odier, Chen, and Ecke <sup>48</sup>					
	$0.5 \div 1.4$	$0.2 \div 0.6$	$0.15 \div 0.7$	$1.6 \div 6.8$	

354 ratory gravity currents, the excess density decreases over the whole flow depth, whereas in  
 355 the katabatic wind (buoyancy supply from the boundary) the density variation is located in  
 356 the lower 10 – 20% of the gravity flow. In spite of this considerable difference in mean flow,  
 357 in addition to the large difference in Reynolds number, entrainment coefficients lie within  
 358 the bulk of laboratory currents as is seen in Fig.6.

359 To compare turbulence quantities, notably mixing lengths  $L_m$  and  $K_m$ , with those ob-  
 360 tained in katabatic winds, extended to larger  $z$  values given in Charrondière, Hopfinger, and  
 361 Brun<sup>1</sup> (cf. Tab.II), a characteristic length scale is required for making  $L_m$ ,  $K_m$  as well as  $L_s$   
 362 dimensionless. An appropriate length scale is  $\Delta z = \Delta u / \partial_z u_{z_{0.5}}$ , where  $\Delta u$  is the maximum  
 363 mean velocity  $u_m$ . Indeed, by adopting the latter, all the data collapses reasonably well  
 364 as is shown in Figs.13(c,d), where in (c),  $K_m / \Delta z \Delta u$  are plotted as a function of  $L_s^2 / \Delta u^2$   
 365 and in (d), mixing lengths  $L_m / \Delta z$  as a function of  $L_s / \Delta z$ . Both, the scaled  $K_m$  and  $L_m$   
 366 increase with  $L_s$  to reach an upper limit of  $K_m / \Delta z \Delta u \approx 0.008$  and  $L_m / \Delta z \approx 0.1$ . Inter-

367 estingly, these maximum values of dimensionless eddy coefficients and mixing lengths are  
 368 similar to that of a turbulent boundary layer where  $L_m/\delta \approx 0.1$  (the shear thickness  $\Delta z$  is  
 369 the equivalent of the velocity shear layer thickness  $\delta$ ). In terms of bottom friction velocity,  
 370  $u_\tau \approx 0.07u_m^6$ ,  $K_m/\Delta z u_\tau \approx 0.1$ , and which is close to the maximum value in a turbulent  
 371 boundary layer (Pope<sup>61</sup>, p.307). However, the variations of eddy coefficients and mixing  
 372 lengths with  $L_s$ , have quite different origins. In katabatic flows, these are a function of  
 373 height  $z$  with values increasing from nearly zero up to the maximum value, whereas in the  
 374 constant buoyancy flux gravity current, the mixing length is practically constant along  $z$ .  
 375 The change seen in Figs.13(c,d) is due to a change with position  $x$ , i.e. values are maximum  
 376 at  $x^* = 7$  and lower at  $x^* = 11$ . The eddy coefficient varies with  $z$  and with  $x$ . This notable  
 378 difference with katabatic winds is due to the widely different mean velocity profiles.

## 379 V. SUMMARY AND CONCLUDING REMARKS

380 The constant buoyancy flux gravity currents flowing from horizontal onto a steep, hy-  
 381 perbolic tangent shaped slope that is representative of an alpine topography, reveal novel  
 382 features. The current accelerates down the slope until Kelvin-Helmholtz instabilities de-  
 383 velop, which cause the slow down of the current followed by a nearby maximum constant  
 384 velocity. Downstream the slope, on the horizontal boundary, the maximum velocity remains  
 385 nearly unchanged because both the gravitational force and entrainment are drastically re-  
 386 duced. The interfacial instability changes from Holmboe instability (HI) near slope begin to  
 387 Kelvin-Helmholtz (KHI) on the steepest part of the slope, where  $Ri_g \approx 0.1$  and entrainment  
 388 is large, followed by turbulence collapse, i.e. a stable turbulent shear layer (TSL), where  
 389  $Ri_g \approx 0.3$  and entrainment ceases.

390 The computed Reynolds stresses are maximum in the central part of the interface with  
 391 the distribution depending on the buoyancy flux. In the TSL region Reynolds stresses are  
 392 more spread out. Mixing lengths determined via the correlation terms between fluctuating  
 393 components of the velocity field at the location of the steepest slope ( $x^* = 7$ ) and at  
 394 a downstream position in the turbulent shear layer (TSL) region ( $x^* = 11$ ) are practically  
 395 constant across the shear zone whereas eddy coefficients vary with height. Both scale closely  
 396 with the shear scale, in agreement with Odier, Chen, and Ecke<sup>48</sup>. The comparison between  
 397 the present saline gravity current experiments and of field data, obtained in katabatic winds



This is the author's peer reviewed, accepted manuscript. However, the online version of record will be different from this version once it has been copyedited and typeset.  
 PLEASE CITE THIS ARTICLE AS DOI: 10.1063/5.0132830

Accepted to Phys. Fluids 10.1063/5.0132830

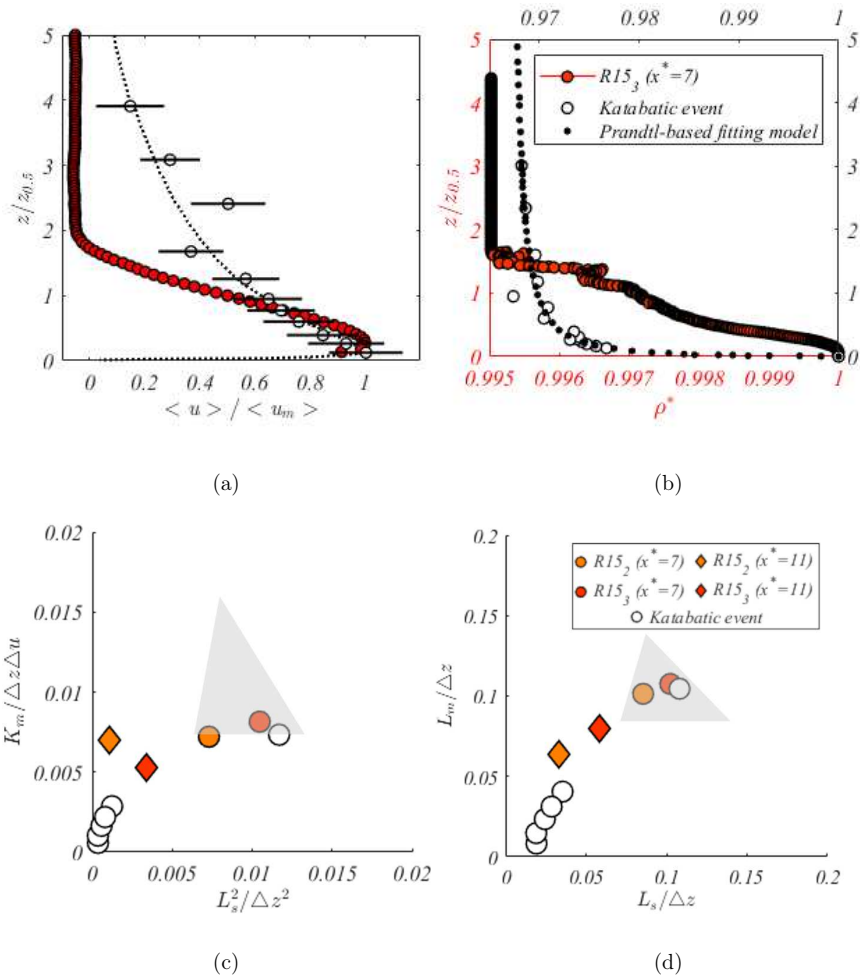


FIG. 13. Dimensionless profiles of mean streamwise velocity, (a) and of density, (b), at  $x^* = 7$  in experiment  $R15_3$  compared with katabatic wind profiles of 2019B event in<sup>6</sup>. Dimensionless eddy coefficients  $K_m$ , (c), and mixing lengths  $L_m$  (d), versus dimensionless shear length  $L_s$ . The shaded gray area represents the values of Odier, Chen, and Ecke<sup>48</sup>.

398 on alpine slopes, highlights the very different mean flow structures. However, the mixing  
 399 lengths and the eddy coefficients data agree surprisingly well and collapse when using an  
 400 appropriate scaling which has been defined as ( $\Delta z = \Delta u / \partial_z u_{z_{0,5}}$ ), even though Reynolds

401 numbers between the laboratory and the observational data differ at least of two orders of  
402 magnitude. An upper limit of mixing length and eddy coefficient is reached at a certain  
403 value of the shear scale, corresponding to a certain height in katabatic winds.

404 Reproducing katabatic wind conditions in the laboratory would be of interest for the  
405 understanding of certain important aspects of these flows. It is for instance well documented  
406 that katabatic winds exhibit mean flow oscillations<sup>4,6,72</sup> and it has been speculated that these  
407 oscillations are related with ambient stratification. Thus, experiments with saline gravity  
408 currents in the presence of ambient stratification could help in clarifying the underlying  
409 mechanism of these oscillations. As a further step, simulating katabatic flow conditions  
410 in the laboratory, by injecting a saline solution through a porous bottom boundary or by  
411 cooling it, would allow to study the spatial mean flow development and related mixing  
412 characteristics proper of katabatic flows.

#### 413 ACKNOWLEDGEMENTS

414 The authors are very grateful to Claudine Charrondiere for making available the katabatic  
415 wind in situ data and for fruitful discussions. Special thanks go to Joseph Virone and Vincent  
416 Govart for their technical support in preparing the experiments. Financial support was given  
417 by a grant from Labex OSUG@2020 (Investissements d'avenir ANR10 LABX56).

#### 418 DECLARATION OF INTERESTS

419 The authors report no conflict of interest.

#### 420 AUTHOR STATEMENT

421 We hereby declare and confirm that all the authors have substantially contributed to the  
422 work, and have read and approved the submitted manuscript.

#### 423 DATA AVAILABILITY STATEMENT

424 The data that support the findings of this study are available from the corresponding  
425 author upon reasonable request.

426 **REFERENCES**

- 427 <sup>1</sup>C. Charrondière, E. J. Hopfinger, and C. Brun, “Identification of  $k_x^{-1}$  strong wave tur-  
 428 bulence and of  $k_x^{-7/5}$  temperature spectral ranges in katabatic winds on a steep slope,”  
 429 Journal of Fluid Mechanics. (Accepted).
- 430 <sup>2</sup>J. E. Simpson, *Gravity currents: In the environment and the laboratory* (Cambridge Uni-  
 431 versity Press, 1997).
- 432 <sup>3</sup>H. Fernando, “Fluid dynamics of urban atmospheres in complex terrain,” *Annu. Rev. Fluid*  
 433 *Mech.* **42**, 365–389 (2010).
- 434 <sup>4</sup>M. Princevac, J. C. R. Hunt, and H. J. S. Fernando, “Quasi-steady katabatic winds on  
 435 slopes in wide valleys: Hydraulic theory and observations,” *J. of Atm. Sci.* **65**, 627 – 643  
 436 (2008).
- 437 <sup>5</sup>C. Brun, S. Blein, and J.-P. Chollet, “Large-eddy simulation of a katabatic jet along a  
 438 convexly curved slope. part i: Statistical results,” *Journal of the Atmospheric Sciences* **74**,  
 439 4047–4073 (2017).
- 440 <sup>6</sup>C. Charrondière, C. Brun, E. J. Hopfinger, J.-M. Cohard, and J.-E. Sicart, “Mean flow  
 441 structure of katabatic winds and turbulent mixing properties,” *Journal of Fluid Mechanics*  
 442 **941** (2022).
- 443 <sup>7</sup>A. L. Gordon, A. H. Orsi, R. Muench, B. A. Huber, E. Zambianchi, and M. Visbeck,  
 444 “Western ross sea continental slope gravity currents,” *Deep Sea Research Part II: Topical*  
 445 *Studies in Oceanography* **56**, 796–817 (2009).
- 446 <sup>8</sup>E. Meiburg and B. Keller, “Turbidity currents and their deposits,” *Annu. Rev. Fluid Mech.*  
 447 **42**, 135–156 (2010).
- 448 <sup>9</sup>E. Hopfinger, “Snow avalanche motion and related phenomena,” *Annu. Rev. Fluid Mech.*  
 449 **15**, 47–76 (1983).
- 450 <sup>10</sup>B. Marino, L. Thomas, and P. Linden, “The front condition for gravity currents,” *J. Fluid*  
 451 *Mech.* **536**, 49–78 (2005).
- 452 <sup>11</sup>M. E. Negretti, D. Z. Zhu, and G. H. Jirka, “Barotropically induced interfacial waves in  
 453 two-layer exchange flows over a sill,” *Journal of Fluid Mechanics* **592**, 135–154 (2007).
- 454 <sup>12</sup>H. I. Nogueira, C. Adduce, E. Alves, and M. J. Franca, “Analysis of lock-exchange gravity  
 455 currents over smooth and rough beds,” *J. Hydraul. Res.* **51**, 417–431 (2013).

This is the author's peer reviewed, accepted manuscript. However, the online version of record will be different from this version once it has been copyedited and typeset.

PLEASE CITE THIS ARTICLE AS DOI: 10.1063/5.0132830

Accepted to *Phys. Fluids* 10.1063/5.0132830

- 456 <sup>13</sup>R. Inghilesi, C. Adduce, V. Lombardi, F. Roman, and V. Armenio, “Axisymmetric three-  
457 dimensional gravity currents generated by lock exchange,” *J. Fluid Mech.* **851**, 507–544  
458 (2018).
- 459 <sup>14</sup>M. C. De Falco, C. Adduce, A. Cuthbertson, M. E. Negretti, J. Laanearu, D. Malcangio,  
460 and J. Sommeria, “Experimental study of uni-and bi-directional exchange flows in a large-  
461 scale rotating trapezoidal channel,” *Phys. Fluids* **33**, 036602 (2021).
- 462 <sup>15</sup>M. La Rocca, P. Prestininzi, C. Adduce, G. Sciortino, R. Hinkelmann, *et al.*, “Lattice  
463 boltzmann simulation of 3d gravity currents around obstacles,” *Int. J. Offshore Polar*  
464 *Engineering* **23** (2013).
- 465 <sup>16</sup>A. Cuthbertson, J. Laanearu, M. Carr, J. Sommeria, and S. Viboud, “Blockage of saline  
466 intrusions in restricted, two-layer exchange flows across a submerged sill obstruction,”  
467 *Environmental Fluid Mechanics* **18**, 27–57 (2018).
- 468 <sup>17</sup>S. Venuleo, D. Pokrajac, A. J. Schleiss, and M. J. Franca, “Continuously-fed gravity  
469 currents propagating over a finite porous substrate,” *Phys. Fluids* **31**, 126601 (2019).
- 470 <sup>18</sup>J. Zhou and S. K. Venayagamoorthy, “How does three-dimensional canopy geometry affect  
471 the front propagation of a gravity current?” *Physics of Fluids* **32**, 096605 (2020).
- 472 <sup>19</sup>M. De Falco, C. Adduce, and M. Maggi, “Gravity currents interacting with a bottom  
473 triangular obstacle and implications on entrainment,” *Advances in Water Resources* **154**,  
474 103967 (2021).
- 475 <sup>20</sup>M. R. Maggi, C. Adduce, and M. E. Negretti, “Lock-release gravity currents propagating  
476 over roughness elements,” *Environmental Fluid Mechanics* , 1–20 (2022).
- 477 <sup>21</sup>C. Adduce, M. R. Maggi, and M. C. De Falco, “Non-intrusive density measurements in  
478 gravity currents interacting with an obstacle,” *Acta Geophysica* , 1–12 (2022).
- 479 <sup>22</sup>Z. He, D. Han, Y.-T. Lin, R. Zhu, Y. Yuan, and P. Jiao, “Propagation, mixing,  
480 and turbulence characteristics of saline and turbidity currents over rough and perme-  
481 able/impermeable beds,” *Physics of Fluids* **34**, 066604 (2022).
- 482 <sup>23</sup>P. G. Baines, “Mixing regimes for the flow of dense fluid down slopes into stratified envi-  
483 ronments,” *Journal of Fluid mechanics* **538**, 245–267 (2005).
- 484 <sup>24</sup>A. Dai, “Non-boussinesq gravity currents propagating on different bottom slopes,” *Journal*  
485 *of Fluid Mechanics* **741**, 658–680 (2014).
- 486 <sup>25</sup>T. Zemach, M. Ungarish, A. Martin, and M.-E. Negretti, “On gravity currents of fixed  
487 volume that encounter a down-slope or up-slope bottom,” *Physics of Fluids* **31**, 096604

This is the author's peer reviewed, accepted manuscript. However, the online version of record will be different from this version once it has been copyedited and typeset.

PLEASE CITE THIS ARTICLE AS DOI: 10.1063/5.0132830

Accepted to *Phys. Fluids* 10.1063/5.0132830

- 488 (2019).
- 489 <sup>26</sup>T. Ellison and J. Turner, “Turbulent entrainment in stratified flows,” *J. Fluid Mech.* **6**,  
490 423–448 (1959).
- 491 <sup>27</sup>G. Pawlak and L. Armi, “Mixing and entrainment in developing stratified currents,” *Journal of Fluid Mechanics* **424**, 45–73 (2000).
- 492
- 493 <sup>28</sup>M. C. De Falco, L. Ottolenghi, and C. Adduce, “Dynamics of gravity currents flowing up  
494 a slope and implications for entrainment,” *J. Hydraul. Eng.* **146**, 04020011 (2020).
- 495 <sup>29</sup>M. C. De Falco, C. Adduce, M. E. Negretti, and E. J. Hopfinger, “On the dynamics of  
496 quasi-steady gravity currents flowing up a slope,” *Adv. Water Res.* **147**, 103791 (2021).
- 497 <sup>30</sup>C. Marshall, R. Dorrell, S. Dutta, G. Keevil, J. Peakall, and S. Tobias, “The effect of  
498 schmidt number on gravity current flows: The formation of large-scale three-dimensional  
499 structures,” *Physics of Fluids* **33**, 106601 (2021).
- 500 <sup>31</sup>M. Maggi, C. Adduce, and G. Lane-Serff, “Gravity currents interacting with slopes and  
501 overhangs,” *Advances in Water Resources*, 104339 (2022).
- 502 <sup>32</sup>M. Nicholson and M. R. Flynn, “Gravity current flow over sinusoidal topography in a  
503 two-layer ambient,” *Physics of Fluids* **27**, 096603 (2015).
- 504 <sup>33</sup>M. Negretti, J. Flør, and E. Hopfinger, “Development of gravity currents on rapidly  
505 changing slopes,” *J. Fluid Mech.* **833**, 70–97 (2017).
- 506 <sup>34</sup>A. Martin, M. E. Negretti, and E. J. Hopfinger, “Development of gravity currents on  
507 slopes under different interfacial instability conditions,” *Journal of Fluid Mechanics* **880**,  
508 180–208 (2019).
- 509 <sup>35</sup>M. Negretti, A. Martin, and F. Naaim Bouvet, “On the propagation of the front speed of  
510 lock released density clouds,” *Adv. Water Res.* (2022).
- 511 <sup>36</sup>H. J. Fernando, “Turbulent mixing in stratified fluids,” *Annual review of fluid mechanics*  
512 **23**, 455–493 (1991).
- 513 <sup>37</sup>P. Odier, J. Chen, and R. E. Ecke, “Entrainment and mixing in a laboratory model of  
514 oceanic overflow,” *Journal of Fluid Mechanics* **746**, 498–535 (2014).
- 515 <sup>38</sup>W. D. Smyth, J. R. Carpenter, and G. A. Lawrence, “Mixing in symmetric holmboe  
516 waves,” *Journal of Physical Oceanography* **37**, 1566 – 1583 (2007).
- 517 <sup>39</sup>N. Laanaia, A. Wirth, J.-M. Molines, B. Barnier, and J. Verron, “On the numerical  
518 resolution of the bottom layer in simulations of oceanic gravity currents,” *Ocean Sci.* **6**,  
519 563–572 (2010).

- 520 <sup>40</sup>G. Danabasoglu, W. Large, and B. Briegleb, “Climate impacts of parametrized nordic sea  
521 overflows,” *J. Geophys. Res.* **115**, C11005 (2010).
- 522 <sup>41</sup>P. Odier, J. Chen, M. K. Rivera, and R. E. Ecke, “Fluid mixing in stratified gravity  
523 currents: the prandtl mixing length,” *Physical review letters* **102**, 134504 (2009).
- 524 <sup>42</sup>S. Balasubramanian and Q. Zhong, “Entrainment and mixing in lock-exchange gravity  
525 currents using simultaneous velocity-density measurements,” *Physics of Fluids* **30**, 056601  
526 (2018).
- 527 <sup>43</sup>T. Agrawal, B. Ramesh, S. Zimmerman, J. Philip, and J. C. Klewicki, “Probing the  
528 high mixing efficiency events in a lock-exchange flow through simultaneous velocity and  
529 temperature measurements,” *Phys. Fluids* **33**, 016605 (2021).
- 530 <sup>44</sup>P. Mukherjee and S. Balasubramanian, “Energetics and mixing efficiency of lock-exchange  
531 gravity currents using simultaneous velocity and density fields,” *Physical Review Fluids* **5**,  
532 063802 (2020).
- 533 <sup>45</sup>P. Mukherjee and S. Balasubramanian, “Diapycnal mixing efficiency in lock-exchange grav-  
534 ity currents,” *Phys. Rev. Fluids* **6**, 013801 (2021).
- 535 <sup>46</sup>P. Monti, H. Fernando, and M. Princevac, “Waves and turbulence in katabatic winds,”  
536 *Environ Fluid Mech* **14**, 431–450 (2014).
- 537 <sup>47</sup>C. Charrondière, C. Brun, J.-M. Cohard, J.-E. Sicart, M. Obligado, R. Biron, C. Coulaud,  
538 and H. Guyard, “Katabatic winds over steep slopes: overview of a field experiment de-  
539 signed to investigate slope-normal velocity and near-surface turbulence,” *Boundary-Layer*  
540 *Meteorology*, 1–26 (2021).
- 541 <sup>48</sup>P. Odier, J. Chen, and R. Ecke, “Understanding and modeling turbulent fluxes and en-  
542 trainment in a gravity current,” *Physica D: Nonlinear Phenomena* **241**, 260–268 (2012).
- 543 <sup>49</sup>A. J. Yang, E. Tedford, J. Olsthoorn, and G. Lawrence, “Asymmetric holmboe instabilities  
544 in arrested salt-wedge flows,” *Physics of Fluids* **34**, 036601 (2022).
- 545 <sup>50</sup>M. E. Negretti, D. Zhu, and G. Jirka, “The effect of bottom roughness in two-layer flows  
546 down a slope,” *Dyn. Oceans Atm.* **45**, 46–68 (2008).
- 547 <sup>51</sup>J. Eriksson, R. Karlsson, and J. Persson, “An experimental study of a two-dimensional  
548 plane turbulent wall jet,” *Experiments in fluids* **25**, 50–60 (1998).
- 549 <sup>52</sup>C. Buckee, B. Kneller, and J. Peakall, “Turbulence structure in steady, solute-driven  
550 gravity currents,” *Particulate gravity currents*, 173–187 (2001).

This is the author's peer reviewed, accepted manuscript. However, the online version of record will be different from this version once it has been copyedited and typeset.

PLEASE CITE THIS ARTICLE AS DOI: 10.1063/5.0132830

Accepted to *Phys. Fluids* 10.1063/5.0132830

- 551 <sup>53</sup>L. Ottolenghi, C. Adduce, R. Inghilesi, F. Roman, and V. Armenio, “Mixing in lock-release  
552 gravity currents propagating up a slope,” *Phys. Fluids* **28**, 056604 (2016).
- 553 <sup>54</sup>B. Morton, G. I. Taylor, and J. S. Turner, “Turbulent gravitational convection from  
554 maintained and instantaneous sources,” *Proceedings of the Royal Society of London. Series*  
555 *A. Mathematical and Physical Sciences* **234**, 1–23 (1956).
- 556 <sup>55</sup>M. Princevac, H. Fernando, and C. D. Whiteman, “Turbulent entrainment into natural  
557 gravity-driven flows,” *Journal of Fluid Mechanics* **533**, 259–268 (2005).
- 558 <sup>56</sup>M. Wells, C. Cenedese, and C. Caulfield, “The relationship between flux coefficient and  
559 entrainment ratio in density currents,” *Journal of Physical Oceanography* **40**, 2713–2727  
560 (2010).
- 561 <sup>57</sup>C. Cenedese and C. Adduce, “Mixing in a density-driven current flowing down a slope in  
562 a rotating fluid.” *J. Fluid Mech.* **604**, 369–388 (2008).
- 563 <sup>58</sup>V. Alavian, “Behavior of density currents on an incline,” *Journal of hydraulic engineering*  
564 **112**, 27–42 (1986).
- 565 <sup>59</sup>C. Cenedese and C. Adduce, “A new parameterization for entrainment in overflows.”  
566 *J. Phys. Oceanogr.* **40**, 1835–1850 (2010).
- 567 <sup>60</sup>T. Gray, J. Alexander, and M. R. Leeder, “Longitudinal flow evolution and turbulence  
568 structure of dynamically similar, sustained, saline density and turbidity currents,” *Journal*  
569 *of Geophysical Research: Oceans* **111** (2006).
- 570 <sup>61</sup>S. B. Pope, *Turbulent flows* (Cambridge university press, 2000).
- 571 <sup>62</sup>L. Prandtl, “The generation of vortices in fluids of small viscosity,” *The Aeronautical*  
572 *Journal* **31**, 718–741 (1927).
- 573 <sup>63</sup>W. D. Smyth and J. N. Moum, “Length scales of turbulence in stably stratified mixing  
574 layers,” *Physics of Fluids* **12**, 1327–1342 (2000).
- 575 <sup>64</sup>C. Bluteau, N. Jones, and G. Ivey, “Turbulent mixing efficiency at an energetic ocean  
576 site,” *Journal of Geophysical Research: Oceans* **118**, 4662–4672 (2013).
- 577 <sup>65</sup>R. Antonia and B. Pearson, “Effect of initial conditions on the mean energy dissipation  
578 rate and the scaling exponent,” *Physical Review E* **62**, 8086 (2000).
- 579 <sup>66</sup>P. Doron, L. Bertuccioli, J. Katz, and T. Osborn, “Turbulence characteristics and dissi-  
580 pation estimates in the coastal ocean bottom boundary layer from piv data,” *Journal of*  
581 *Physical Oceanography* **31**, 2108–2134 (2001).

This is the author's peer reviewed, accepted manuscript. However, the online version of record will be different from this version once it has been copyedited and typeset.

PLEASE CITE THIS ARTICLE AS DOI: 10.1063/5.0132830

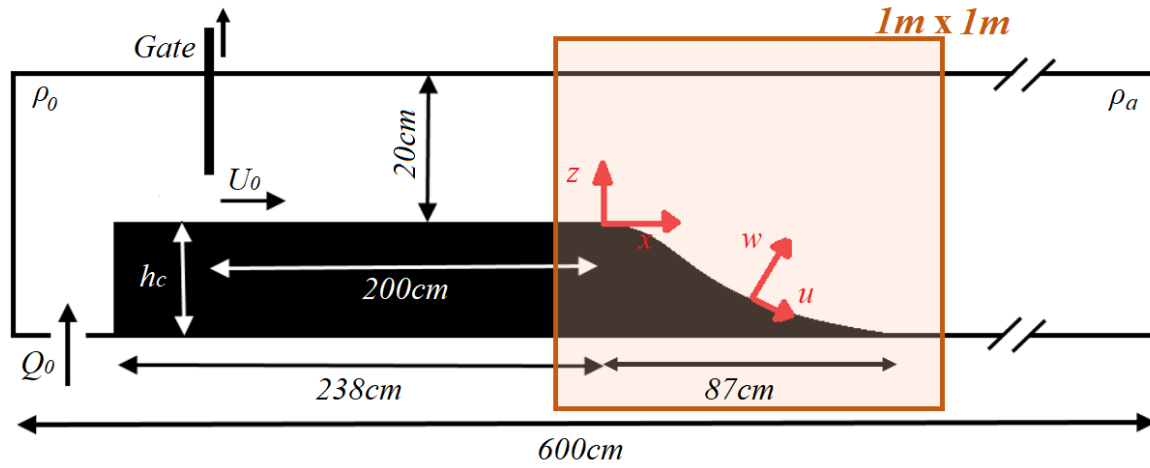
Accepted to *Phys. Fluids* 10.1063/5.0132830

- 582 <sup>67</sup>D. Xu and J. Chen, “Accurate estimate of turbulent dissipation rate using piv data,”  
 583 *Experimental Thermal and Fluid Science* **44**, 662–672 (2013).
- 584 <sup>68</sup>J. V. Steinbuck, P. L. Roberts, C. D. Troy, A. R. Horner-Devine, F. Simonet, A. H.  
 585 Uhlman, J. S. Jaffe, S. G. Monismith, and P. J. Franks, “An autonomous open-ocean  
 586 stereoscopic piv profiler,” *Journal of Atmospheric and Oceanic Technology* **27**, 1362–1380  
 587 (2010).
- 588 <sup>69</sup>H. Tennekes, J. L. Lumley, J. L. Lumley, *et al.*, *A first course in turbulence* (MIT press,  
 589 1972).
- 590 <sup>70</sup>M. M. Maqueda, A. Willmott, and N. Biggs, “Polynya dynamics: a review of observations  
 591 and modeling,” *Rev. Geophys.* **42(1)**, – (2004).
- 592 <sup>71</sup>C. Charrondière, C. Brun, J.-E. Sicart, J.-M. Cohard, R. Biron, and S. Blein, “Buoyancy  
 593 effects in the turbulence kinetic energy budget and reynolds stress budget for a katabatic  
 594 jet over a steep alpine slope,” *Boundary-Layer Meteorology* **177**, 97–122 (2020).
- 595 <sup>72</sup>R. T. McNider, “A note on velocity fluctuations in drainage flows,” (1982).



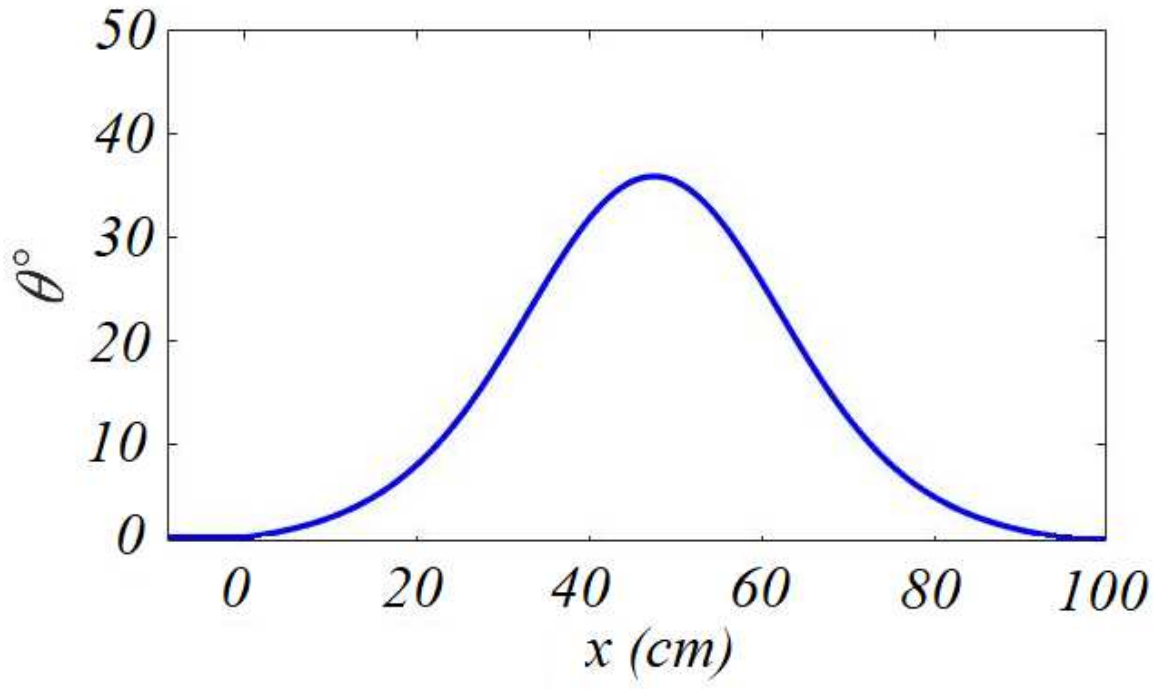
This is the author's peer reviewed, accepted manuscript. However, the online version of record will be different from this version once it has been copyedited and typeset.

PLEASE CITE THIS ARTICLE AS DOI: 10.1063/1.50132830



This is the author's peer reviewed, accepted manuscript. However, the online version of record will be different from this version once it has been copyedited and typeset.

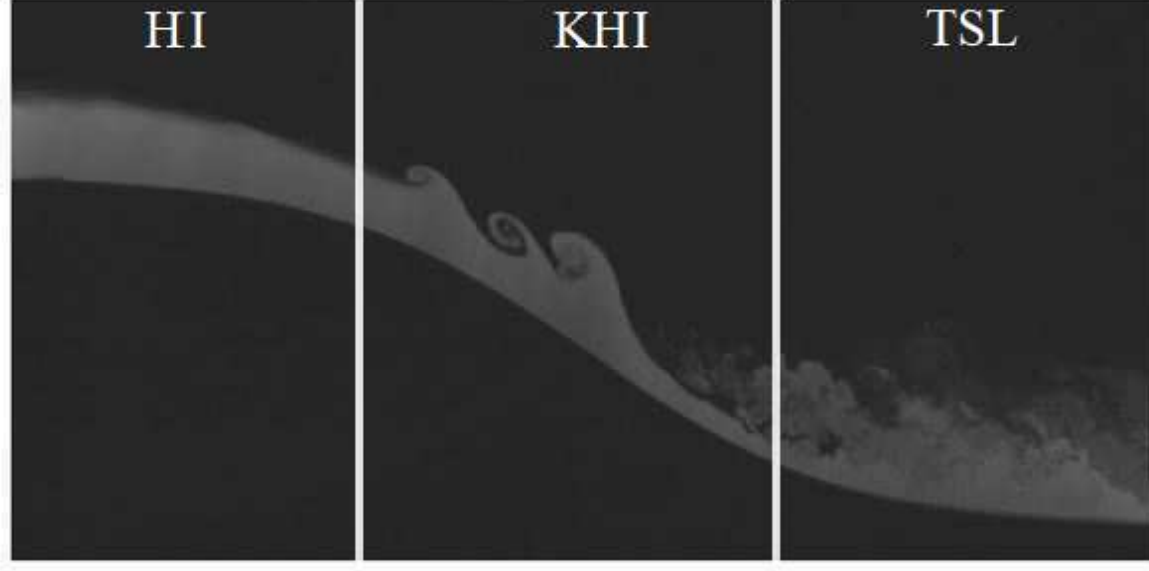
PLEASE CITE THIS ARTICLE AS DOI: 10.1063/5.0132830



**10.1063/**

This is the author's peer reviewed, accepted manuscript. However, the online version of record will be different from this version once it has been copyedited and typeset.

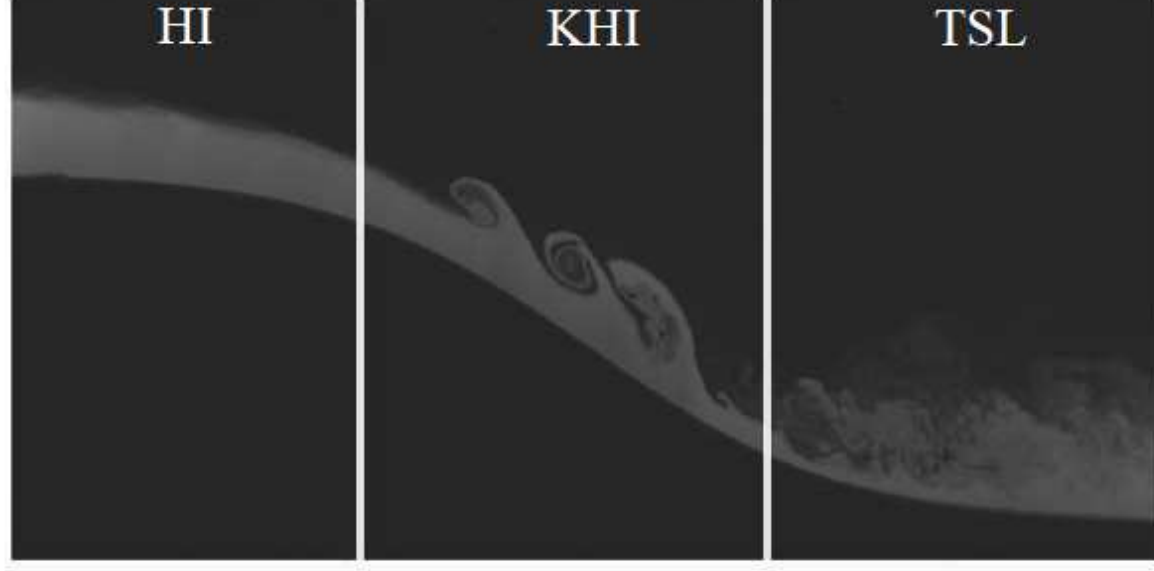
PLEASE CITE THIS ARTICLE AS DOI: 10.1063/1.50132830



  
*Phys.*

This is the author's peer reviewed, accepted manuscript. However, the online version of record will be different from this version once it has been copyedited and typeset.

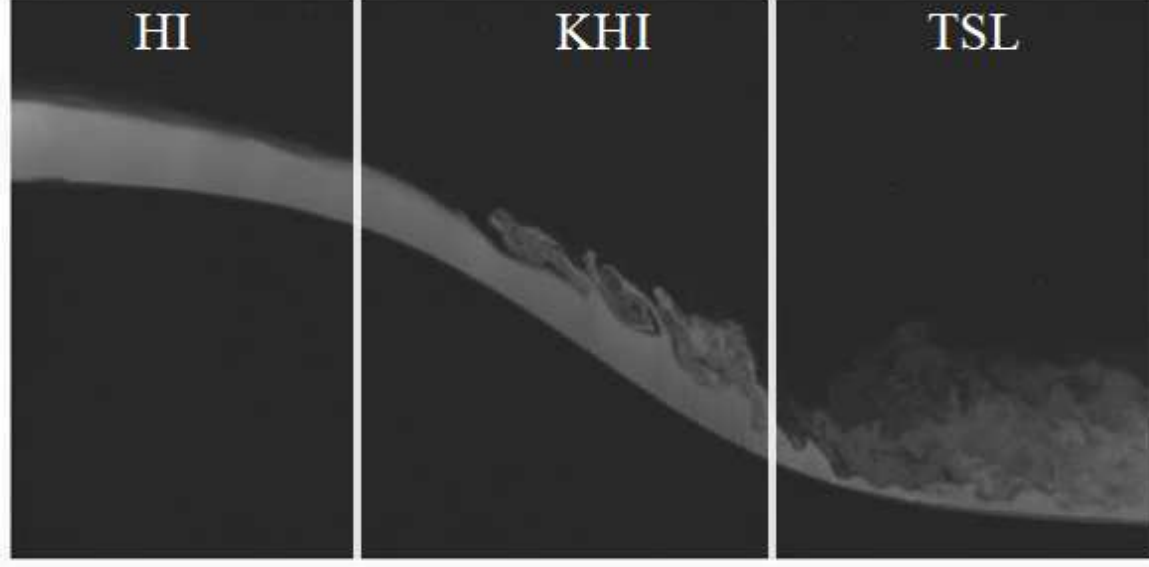
PLEASE CITE THIS ARTICLE AS DOI: 10.1063/1.50132830



*Phys.*

This is the author's peer reviewed, accepted manuscript. However, the online version of record will be different from this version once it has been copyedited and typeset.

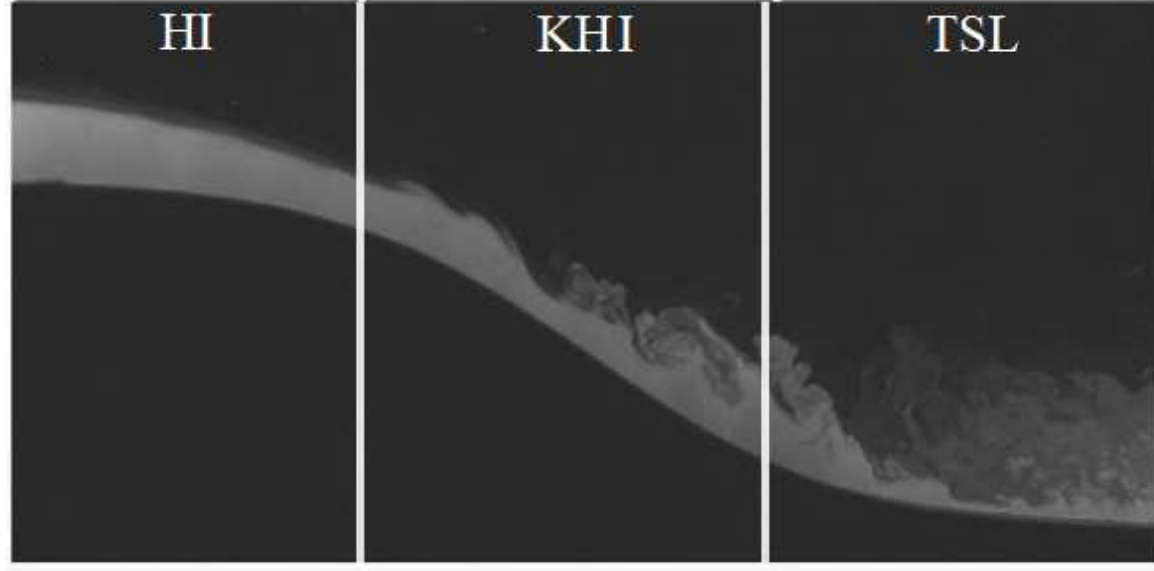
PLEASE CITE THIS ARTICLE AS DOI: 10.1063/1.50132830



*Phys.*

This is the author's peer reviewed, accepted manuscript. However, the online version of record will be different from this version once it has been copyedited and typeset.

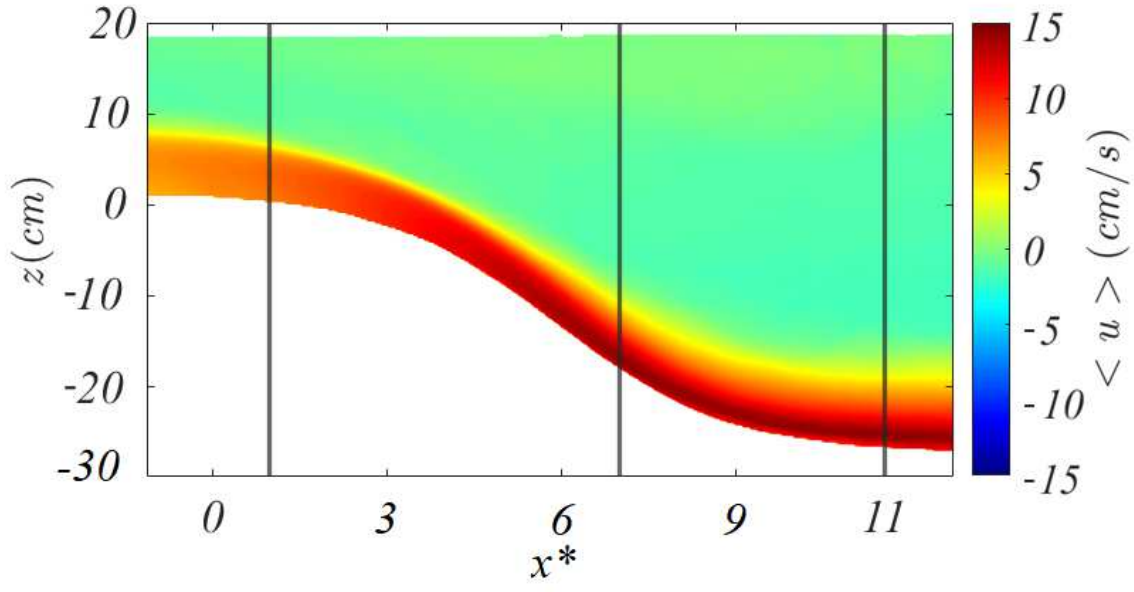
PLEASE CITE THIS ARTICLE AS DOI: 10.1063/1.50132830



*Phys.*

This is the author's peer reviewed, accepted manuscript. However, the online version of record will be different from this version once it has been copyedited and typeset.

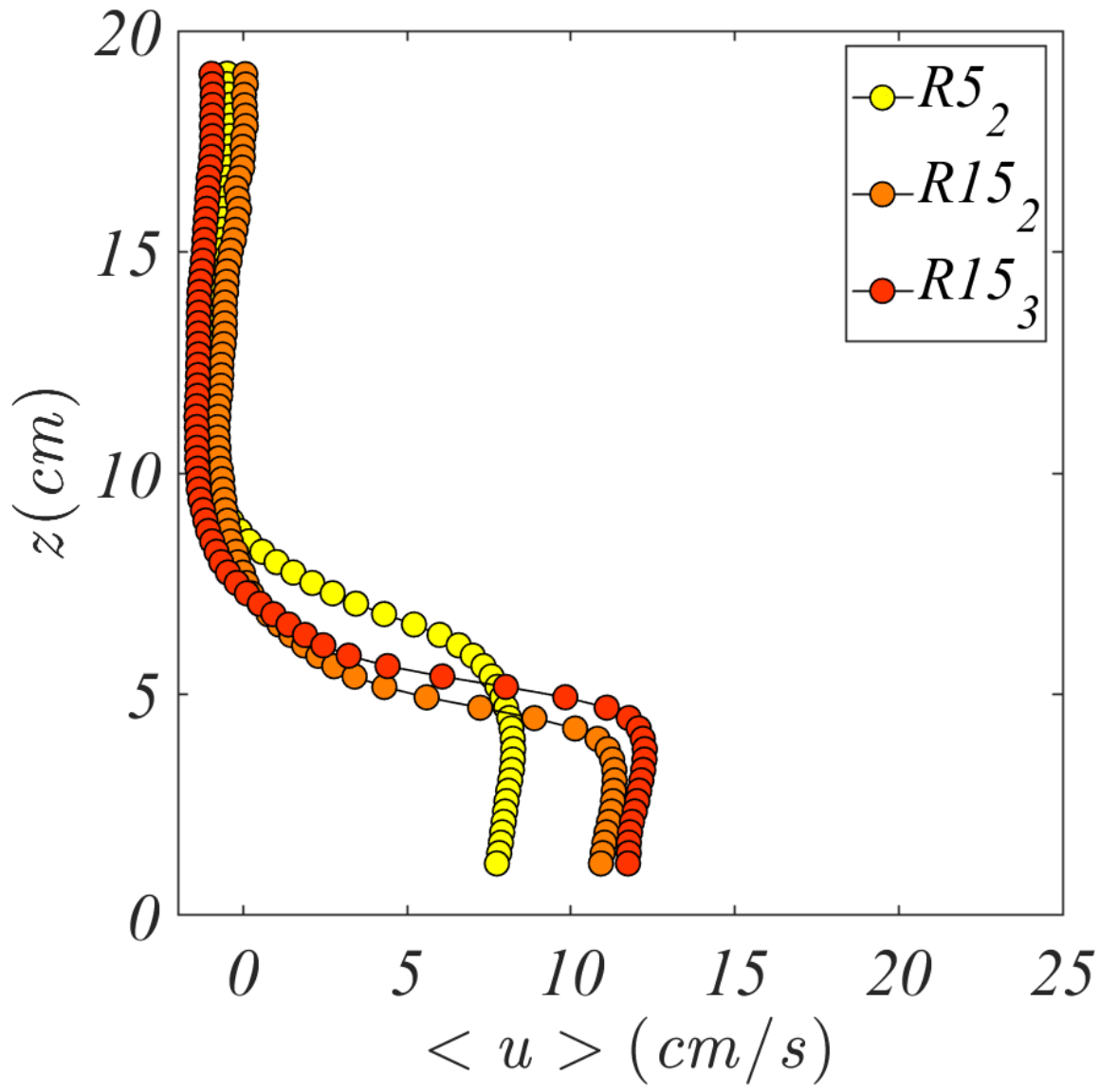
PLEASE CITE THIS ARTICLE AS DOI: 10.1063/5.0132830



**10.1063/5.0**

This is the author's peer reviewed, accepted manuscript. However, the online version of record will be different from this version once it has been copyedited and typeset.

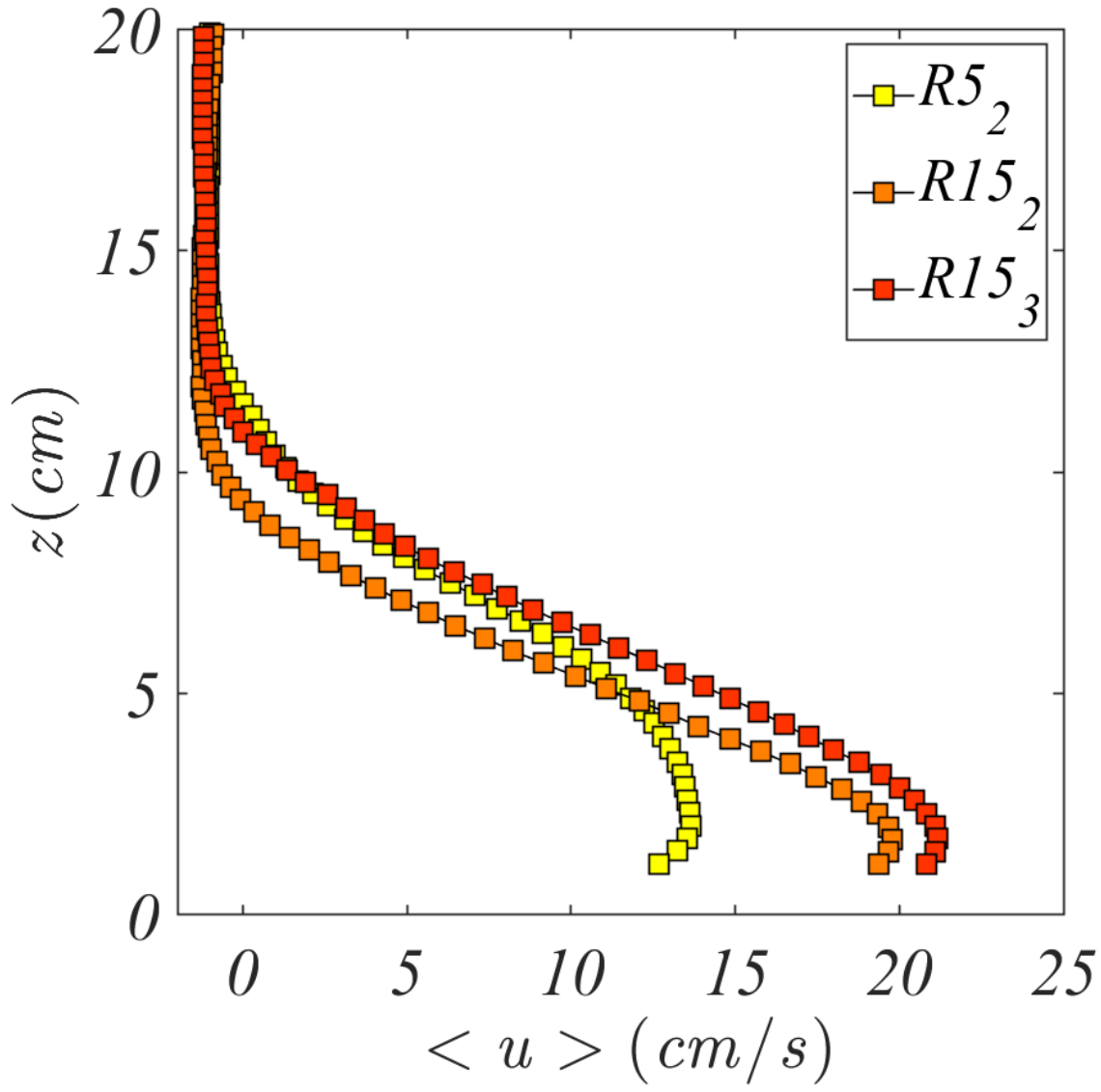
PLEASE CITE THIS ARTICLE AS DOI: 10.1063/1.50132830





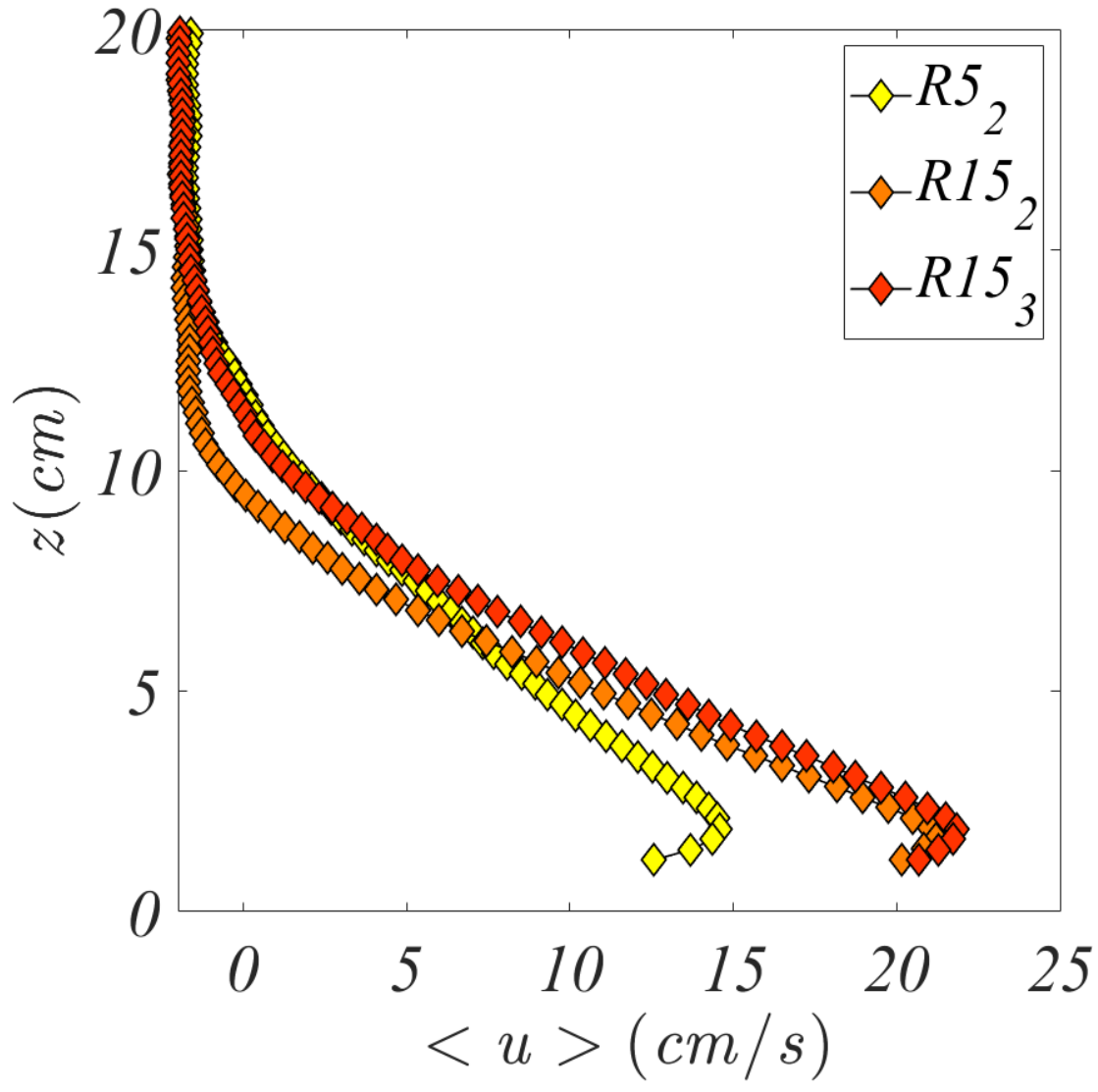
This is the author's peer reviewed, accepted manuscript. However, the online version of record will be different from this version once it has been copyedited and typeset.

PLEASE CITE THIS ARTICLE AS DOI: 10.1063/1.50132830



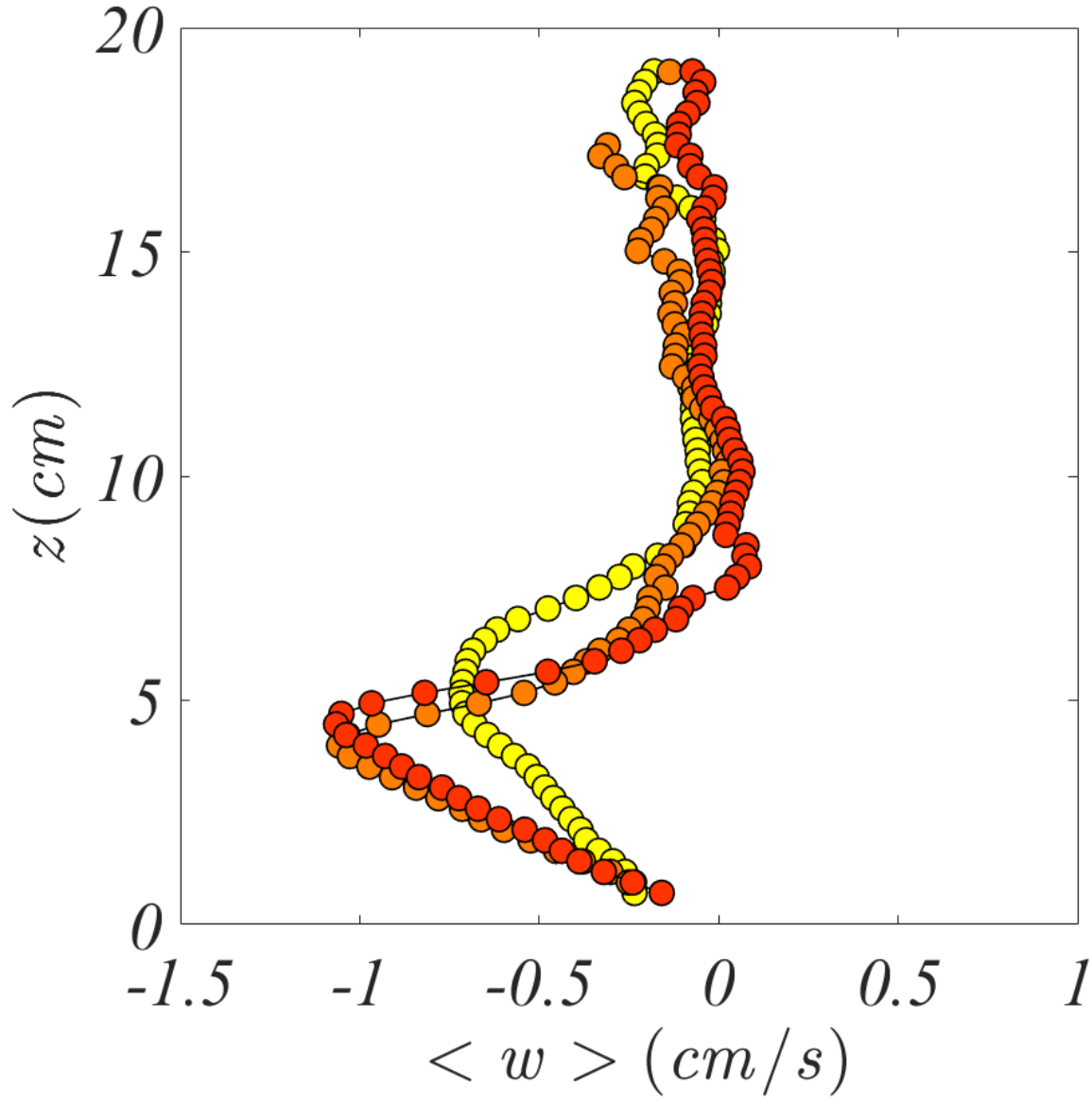
This is the author's peer reviewed, accepted manuscript. However, the online version of record will be different from this version once it has been copyedited and typeset.

PLEASE CITE THIS ARTICLE AS DOI: 10.1063/1.50132830



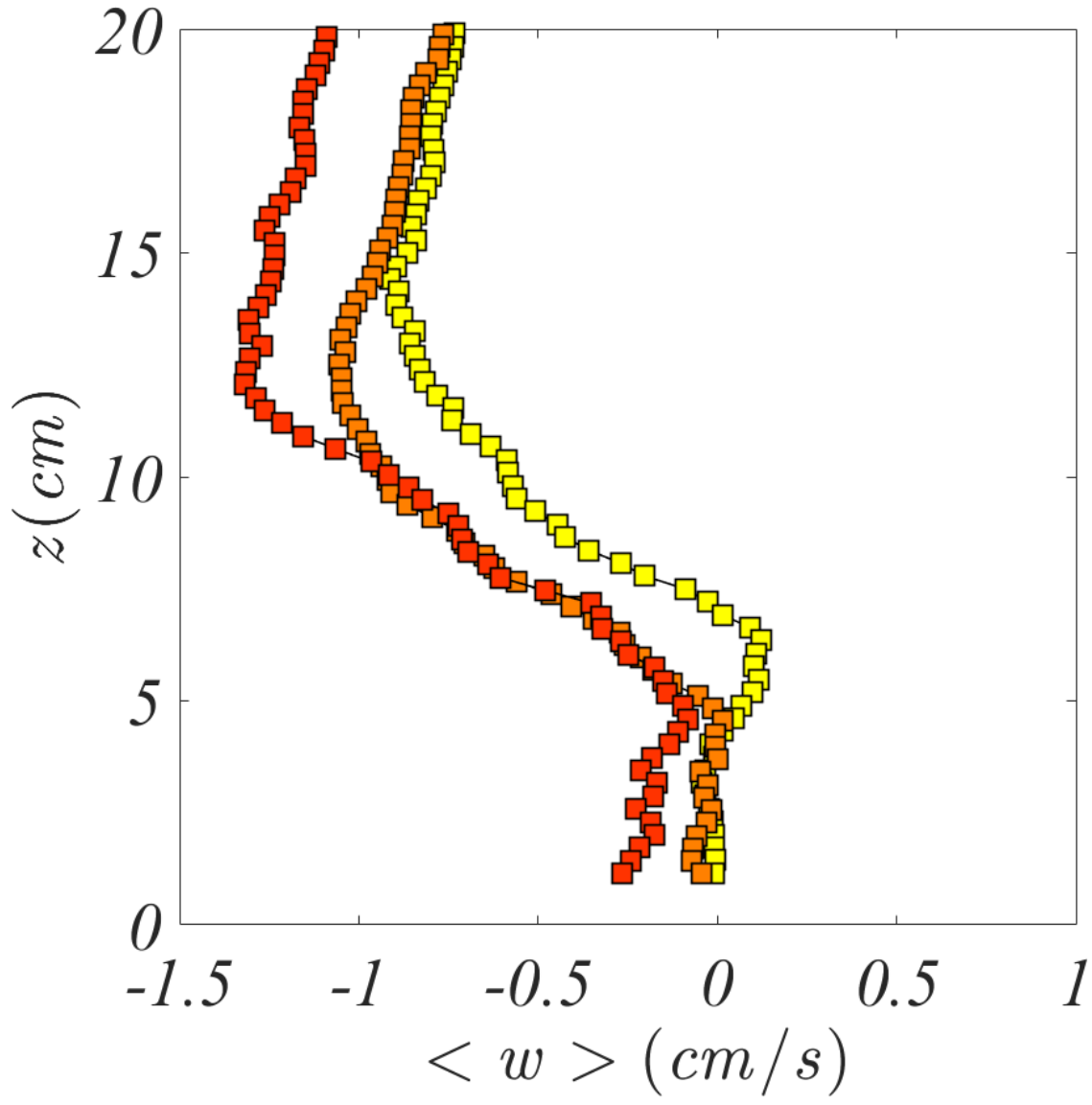
This is the author's peer reviewed, accepted manuscript. However, the online version of record will be different from this version once it has been copyedited and typeset.

PLEASE CITE THIS ARTICLE AS DOI: 10.1063/5.0132830



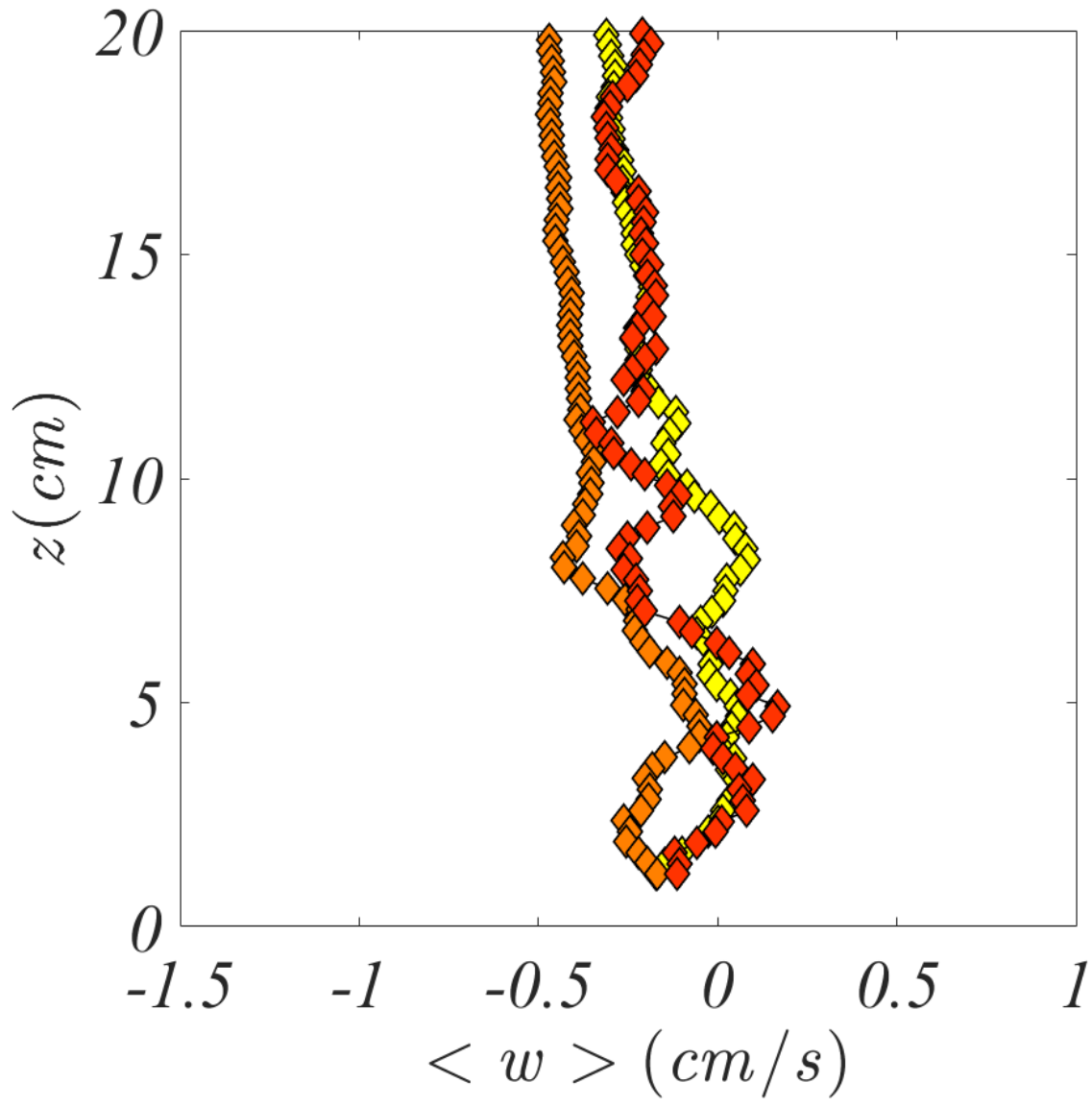
This is the author's peer reviewed, accepted manuscript. However, the online version of record will be different from this version once it has been copyedited and typeset.

PLEASE CITE THIS ARTICLE AS DOI: 10.1063/1.50132830



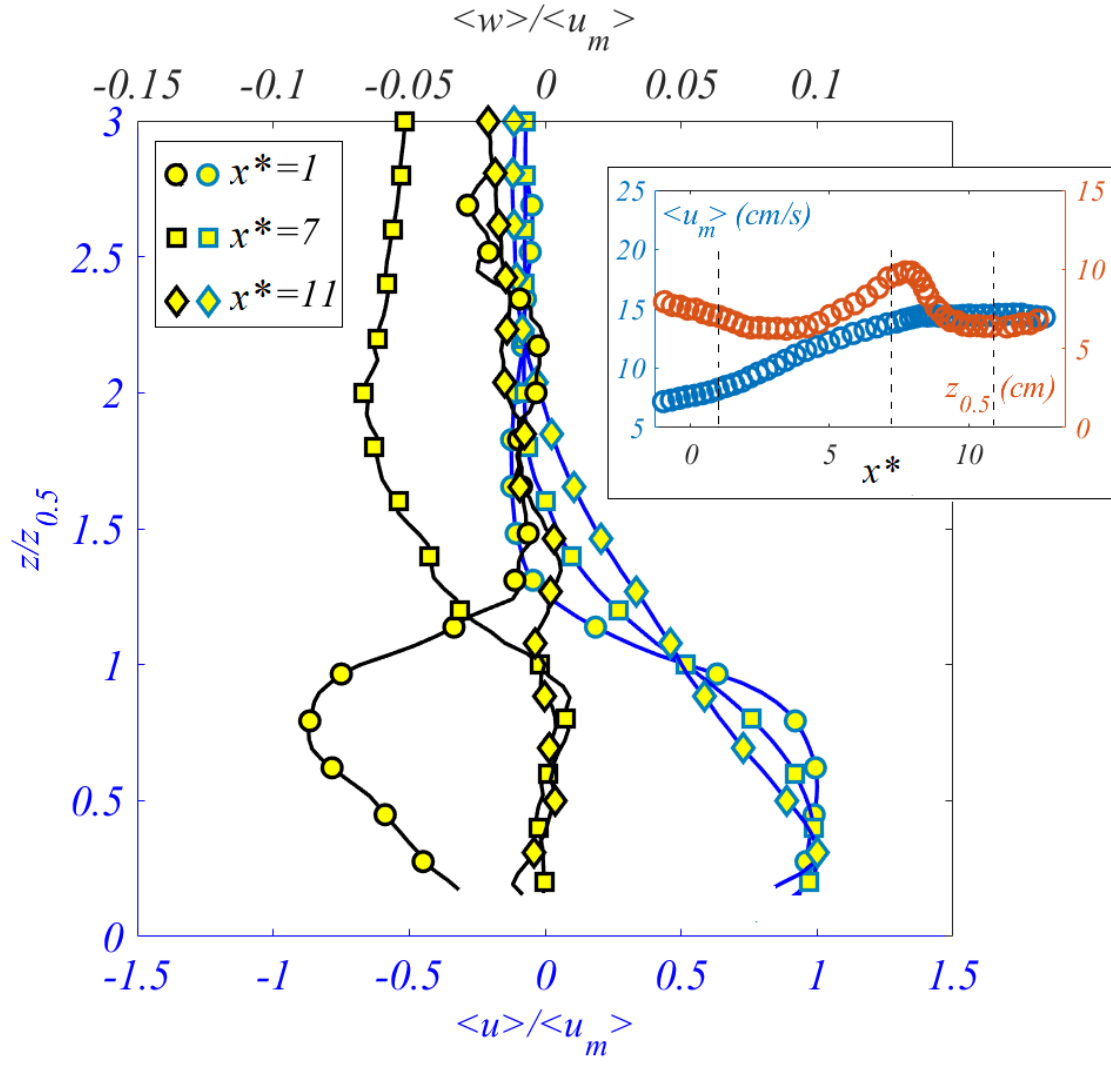
This is the author's peer reviewed, accepted manuscript. However, the online version of record will be different from this version once it has been copyedited and typeset.

PLEASE CITE THIS ARTICLE AS DOI: 10.1063/1.50132830



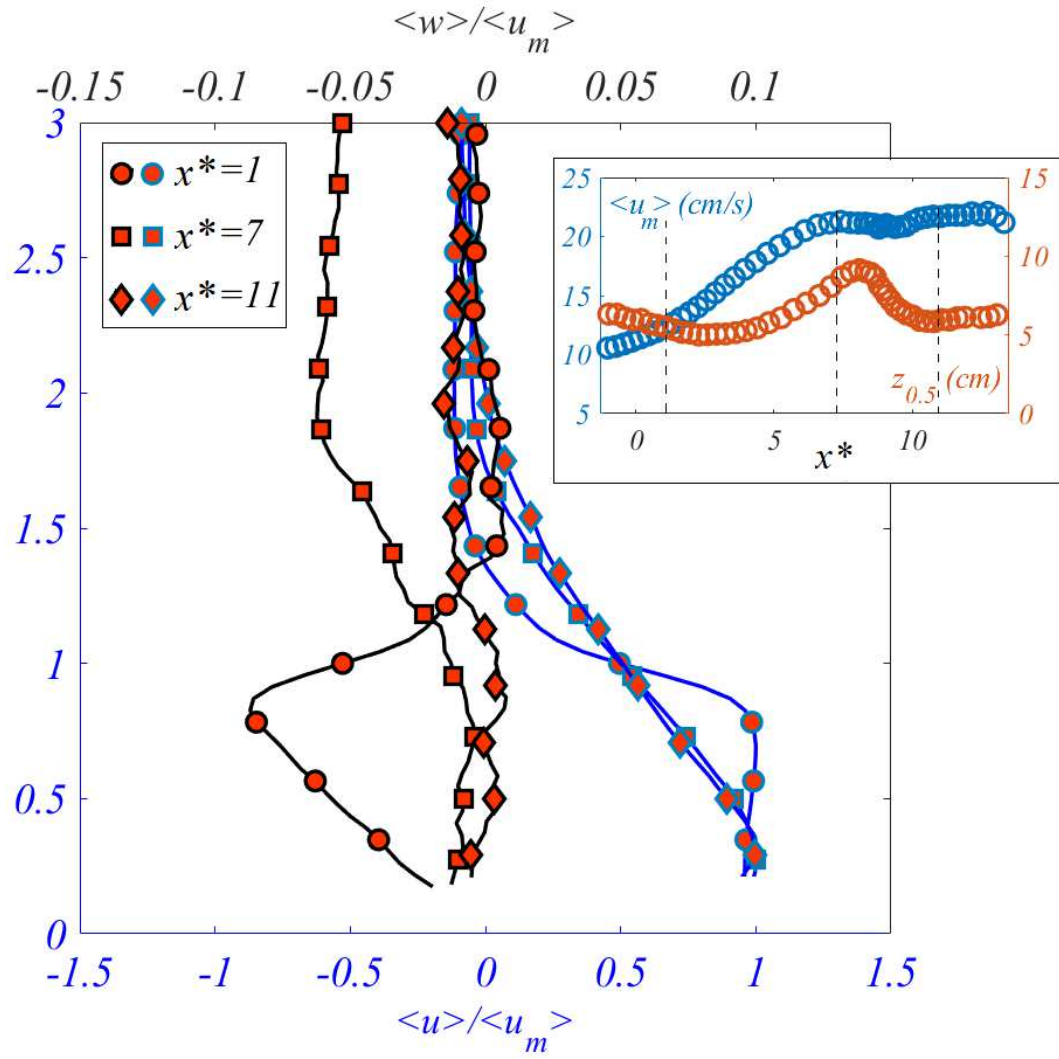
This is the author's peer reviewed, accepted manuscript. However, the online version of record will be different from this version once it has been copyedited and typeset.

PLEASE CITE THIS ARTICLE AS DOI: 10.1063/1.50132830



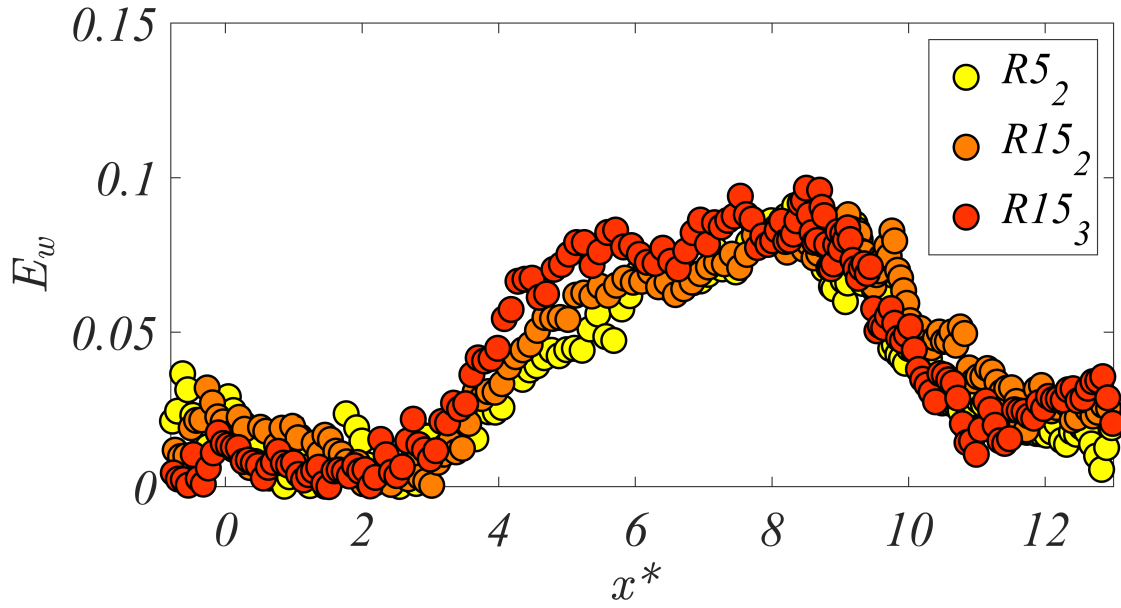
This is the author's peer reviewed, accepted manuscript. However, the online version of record will be different from this version once it has been copyedited and typeset.

PLEASE CITE THIS ARTICLE AS DOI: 10.1063/1.50132830



This is the author's peer reviewed, accepted manuscript. However, the online version of record will be different from this version once it has been copyedited and typeset.

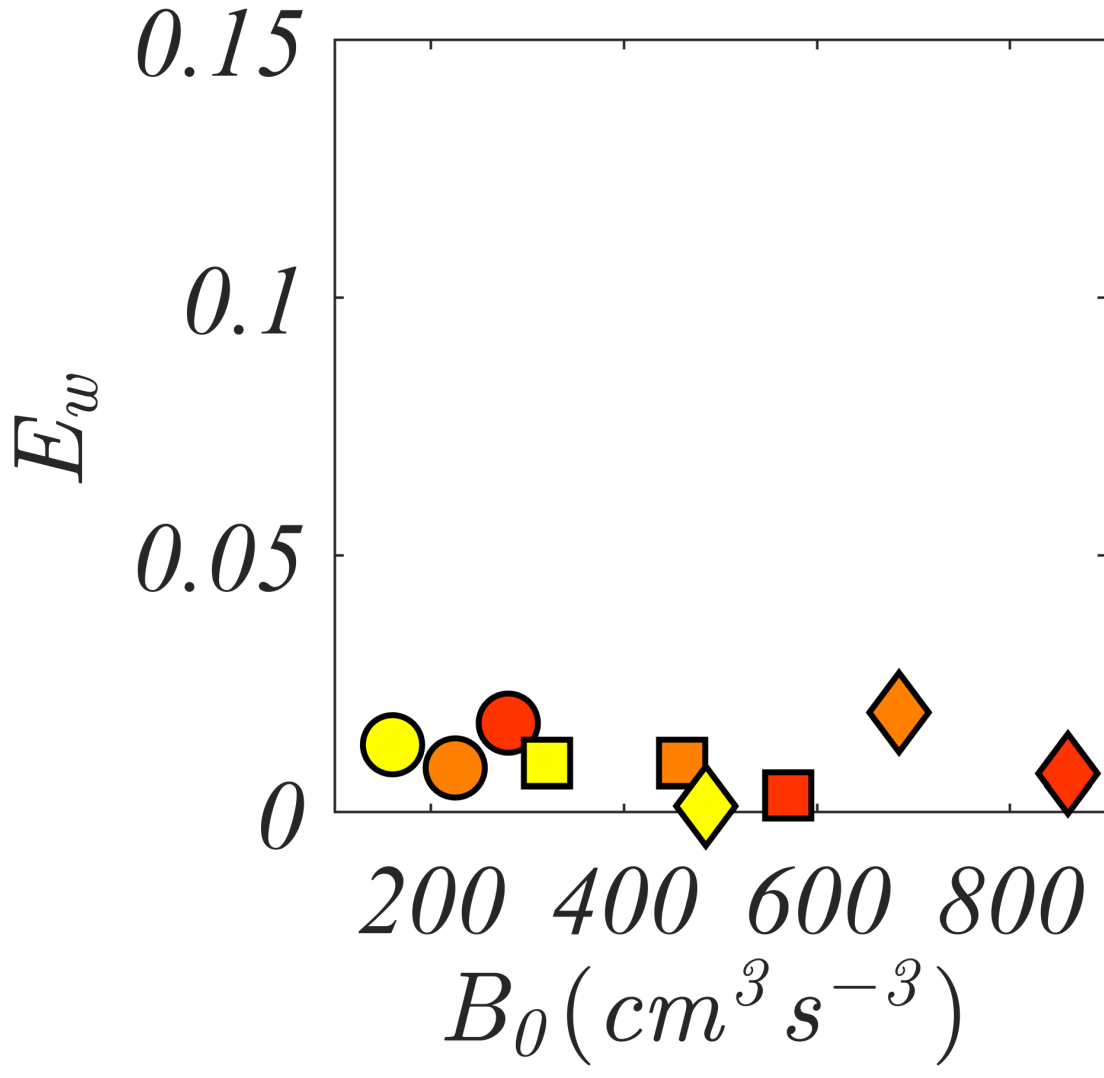
PLEASE CITE THIS ARTICLE AS DOI: 10.1063/1.50132830





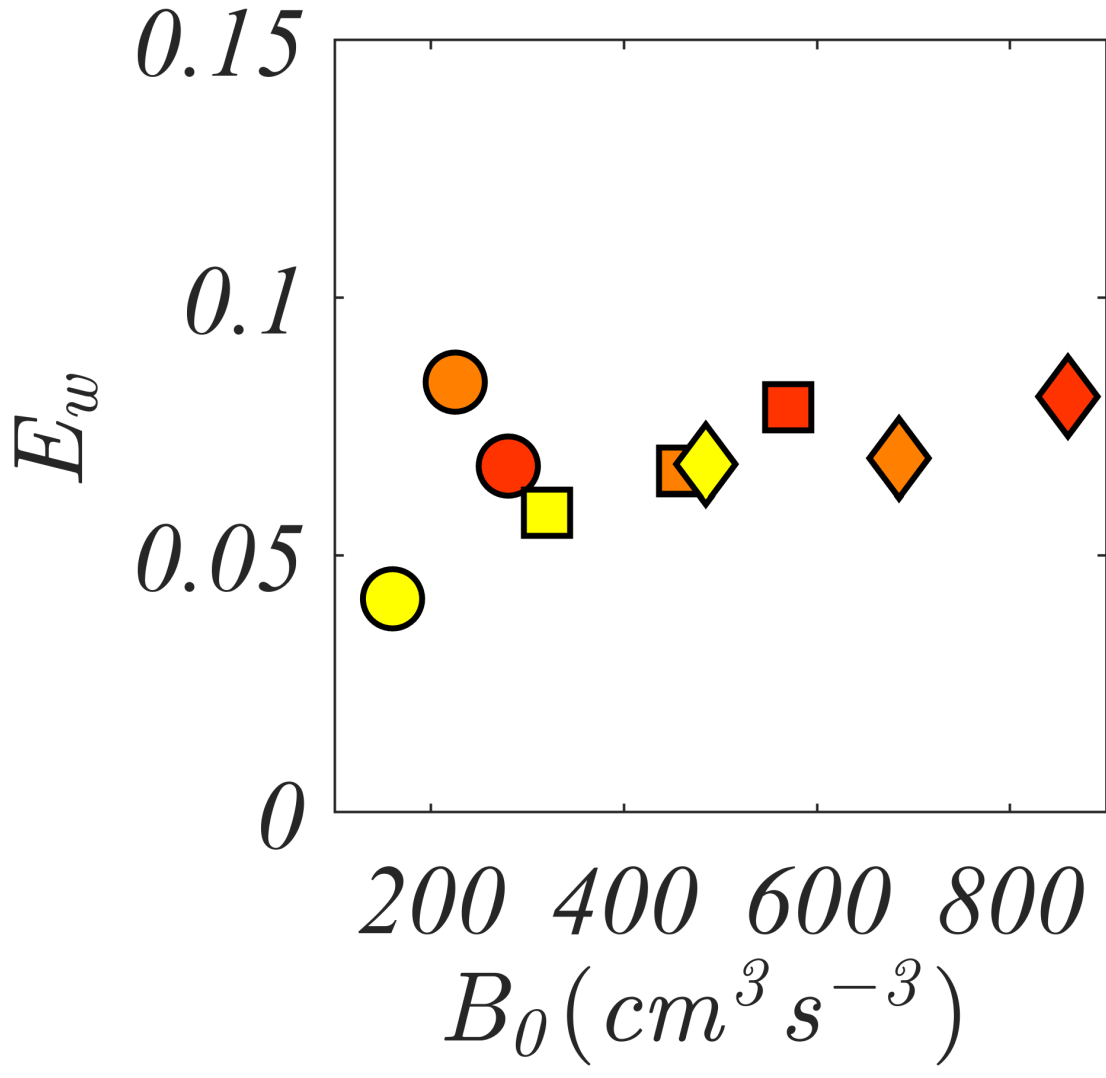
This is the author's peer reviewed, accepted manuscript. However, the online version of record will be different from this version once it has been copyedited and typeset.

PLEASE CITE THIS ARTICLE AS DOI: 10.1063/1.50132830



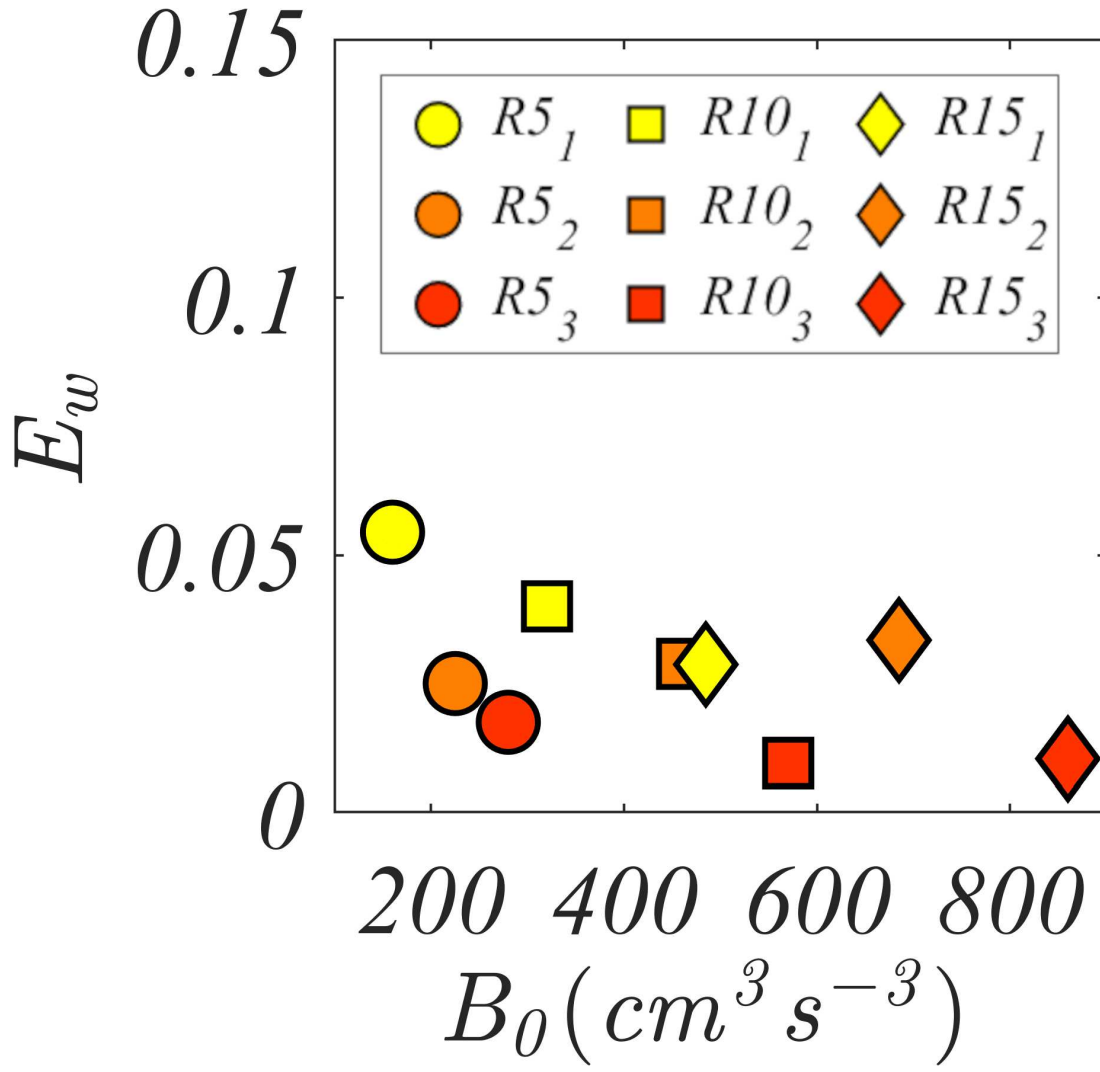
This is the author's peer reviewed, accepted manuscript. However, the online version of record will be different from this version once it has been copyedited and typeset.

PLEASE CITE THIS ARTICLE AS DOI: 10.1063/1.50132830



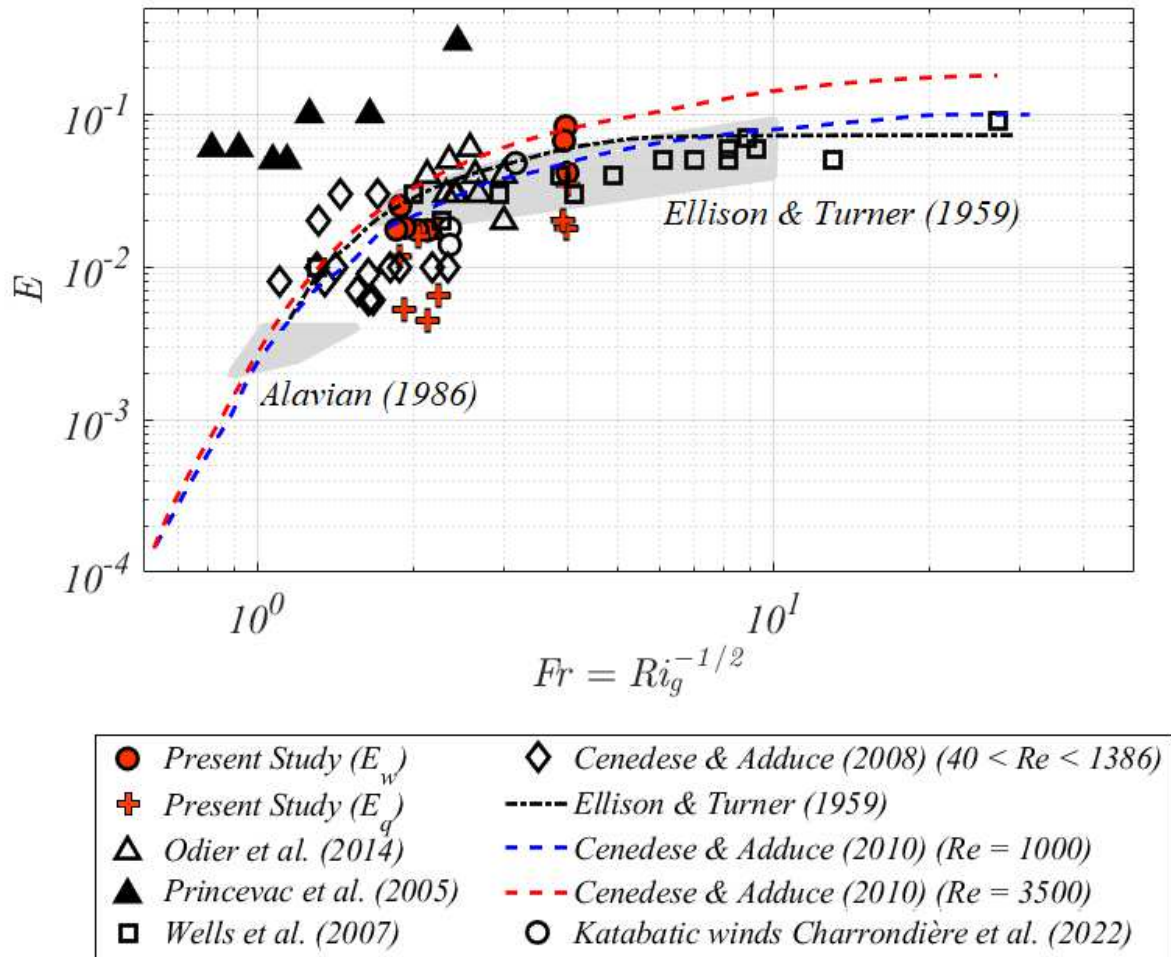
This is the author's peer reviewed, accepted manuscript. However, the online version of record will be different from this version once it has been copyedited and typeset.

PLEASE CITE THIS ARTICLE AS DOI: 10.1063/1.50132830



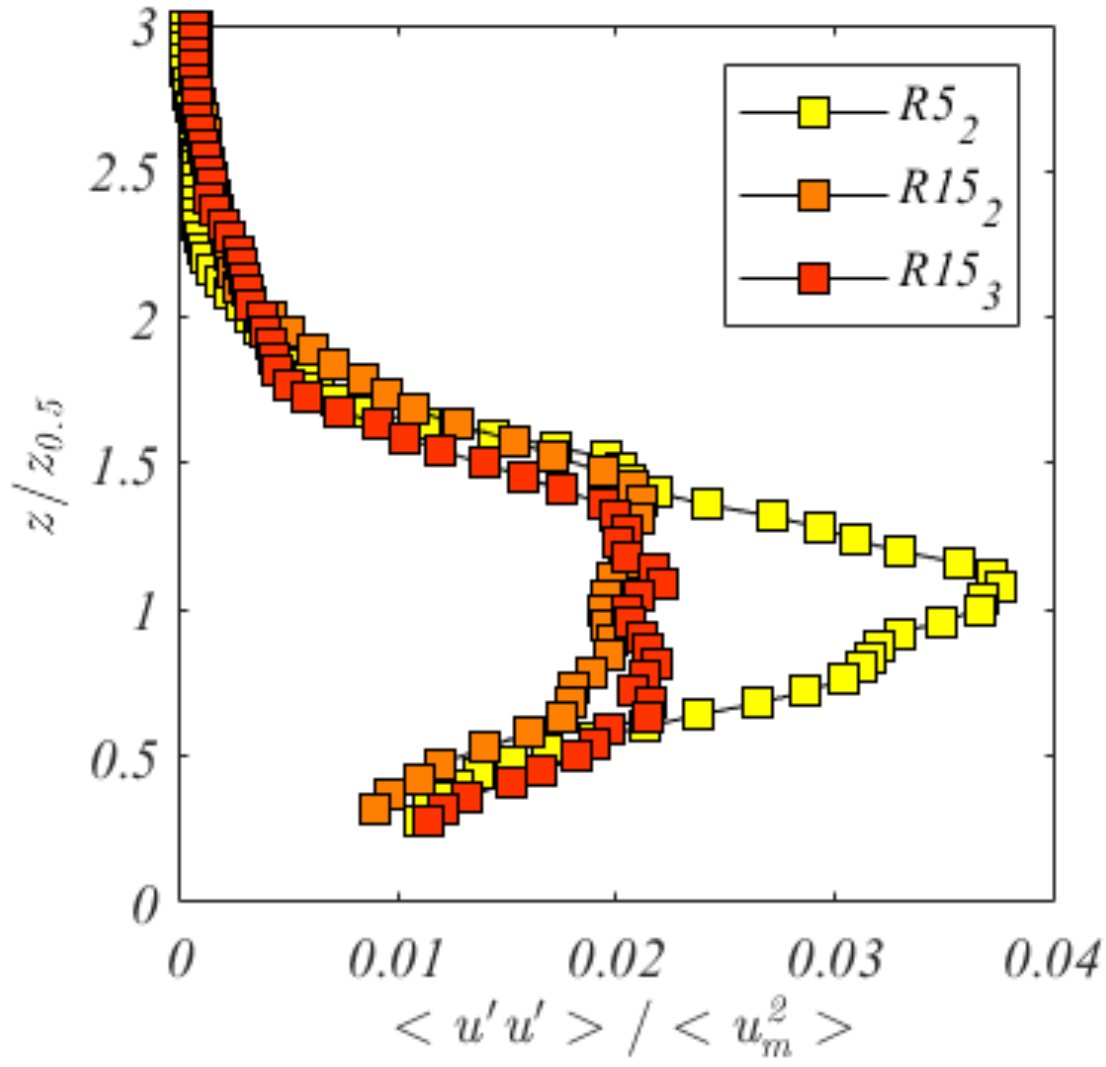
This is the author's peer reviewed, accepted manuscript. However, the online version of record will be different from this version once it has been copyedited and typeset.

PLEASE CITE THIS ARTICLE AS DOI: 10.1063/5.0132830



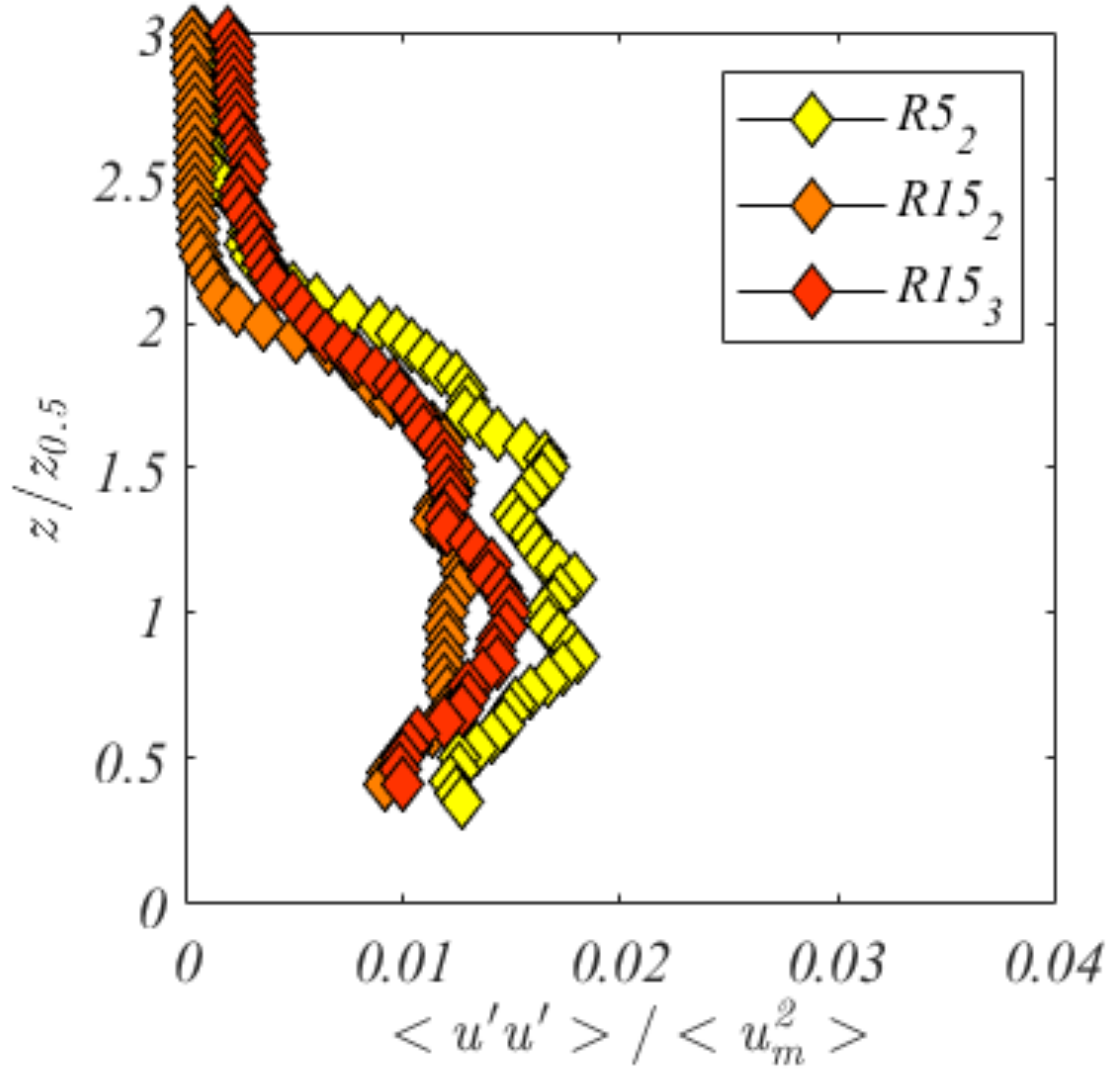
This is the author's peer reviewed, accepted manuscript. However, the online version of record will be different from this version once it has been copyedited and typeset.

PLEASE CITE THIS ARTICLE AS DOI: 10.1063/1.50132830



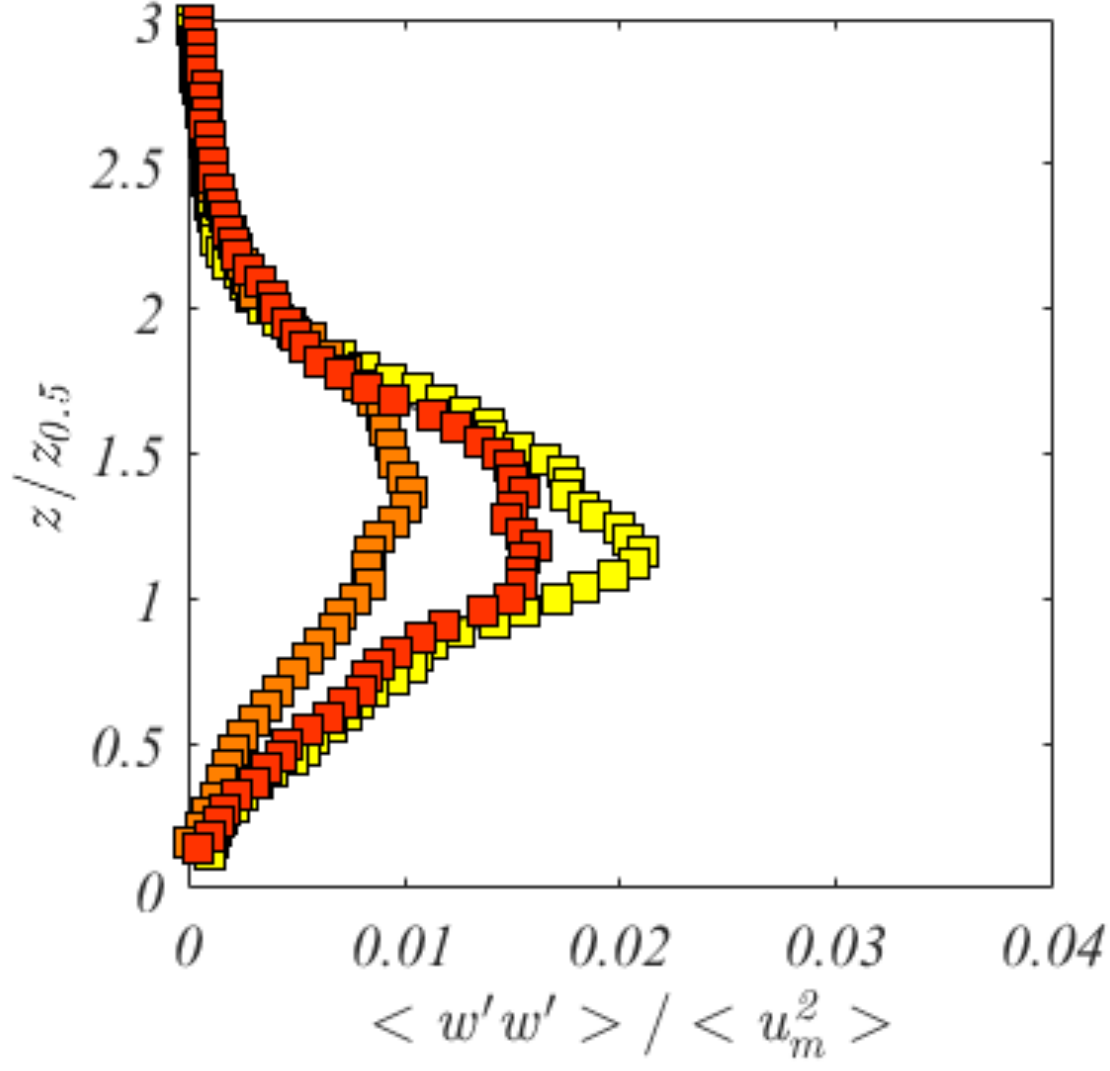
This is the author's peer reviewed, accepted manuscript. However, the online version of record will be different from this version once it has been copyedited and typeset.

PLEASE CITE THIS ARTICLE AS DOI: 10.1063/1.50132830



This is the author's peer reviewed, accepted manuscript. However, the online version of record will be different from this version once it has been copyedited and typeset.

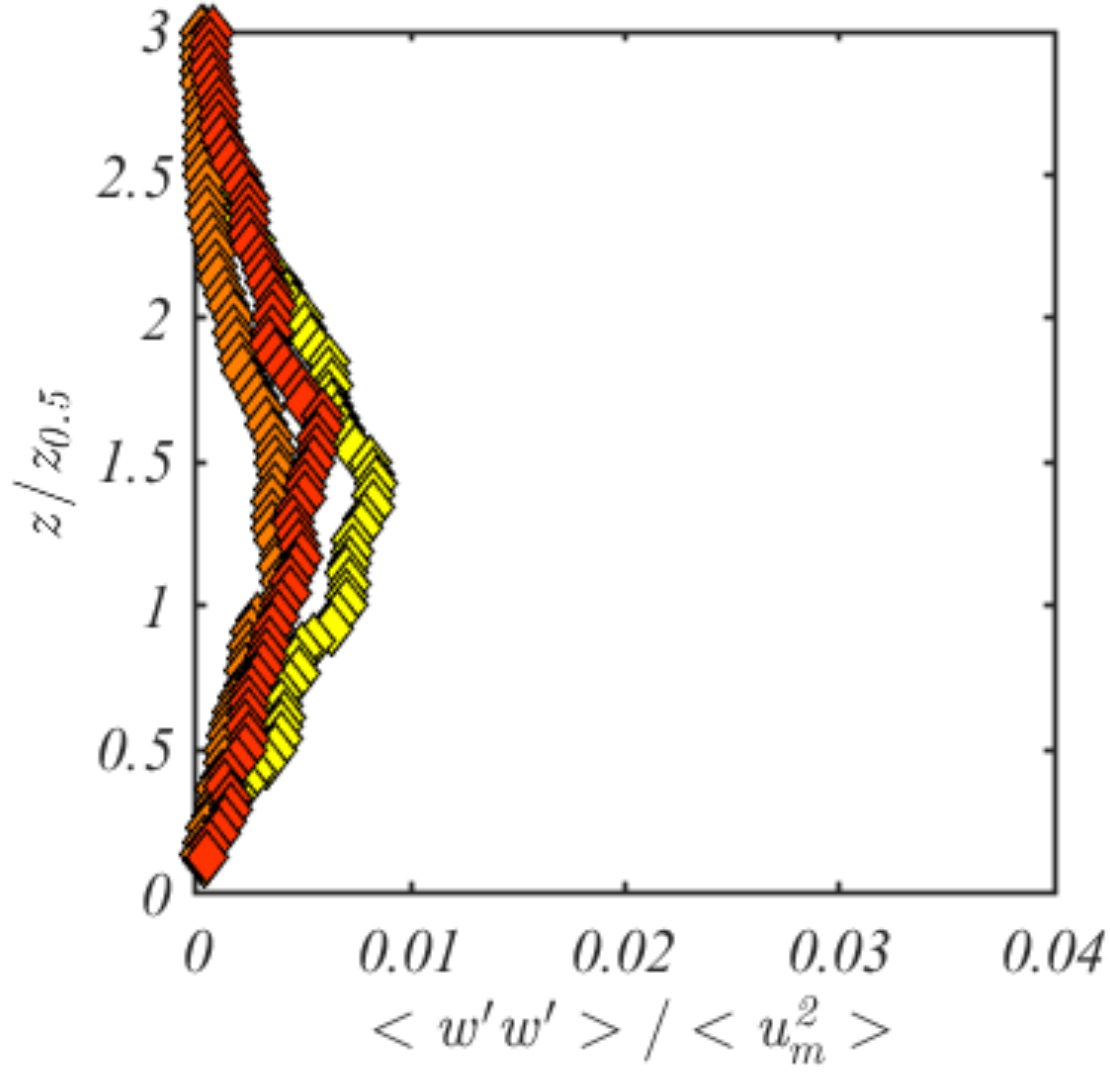
PLEASE CITE THIS ARTICLE AS DOI: 10.1063/1.50132830



**Phys**

This is the author's peer reviewed, accepted manuscript. However, the online version of record will be different from this version once it has been copyedited and typeset.

PLEASE CITE THIS ARTICLE AS DOI: 10.1063/1.50132830

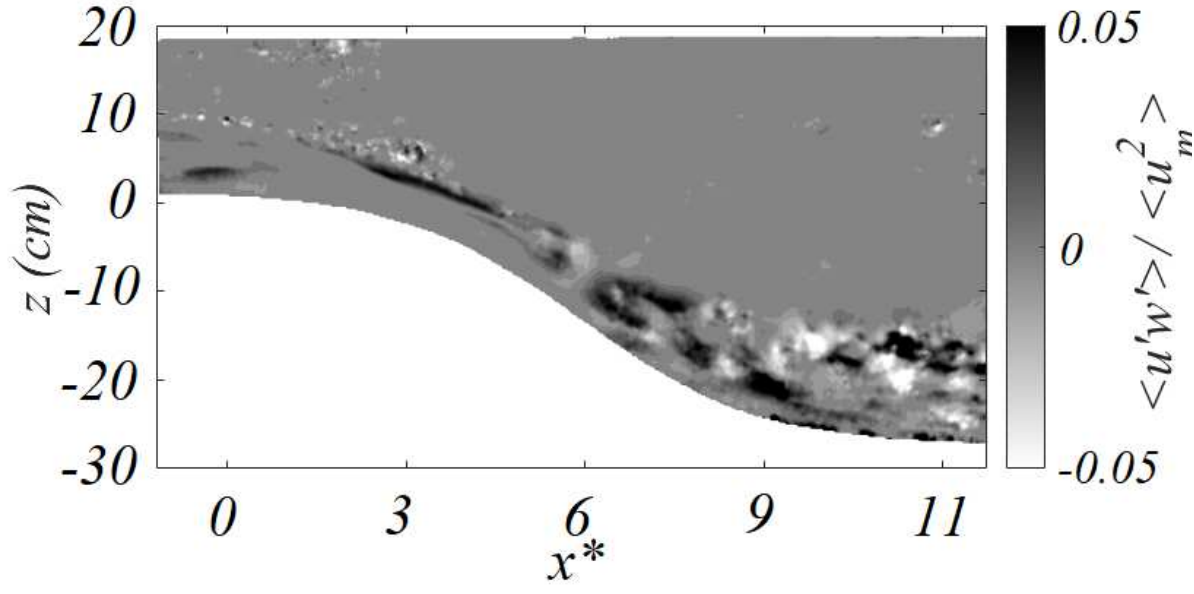


**Phys**



This is the author's peer reviewed, accepted manuscript. However, the online version of record will be different from this version once it has been copyedited and typeset.

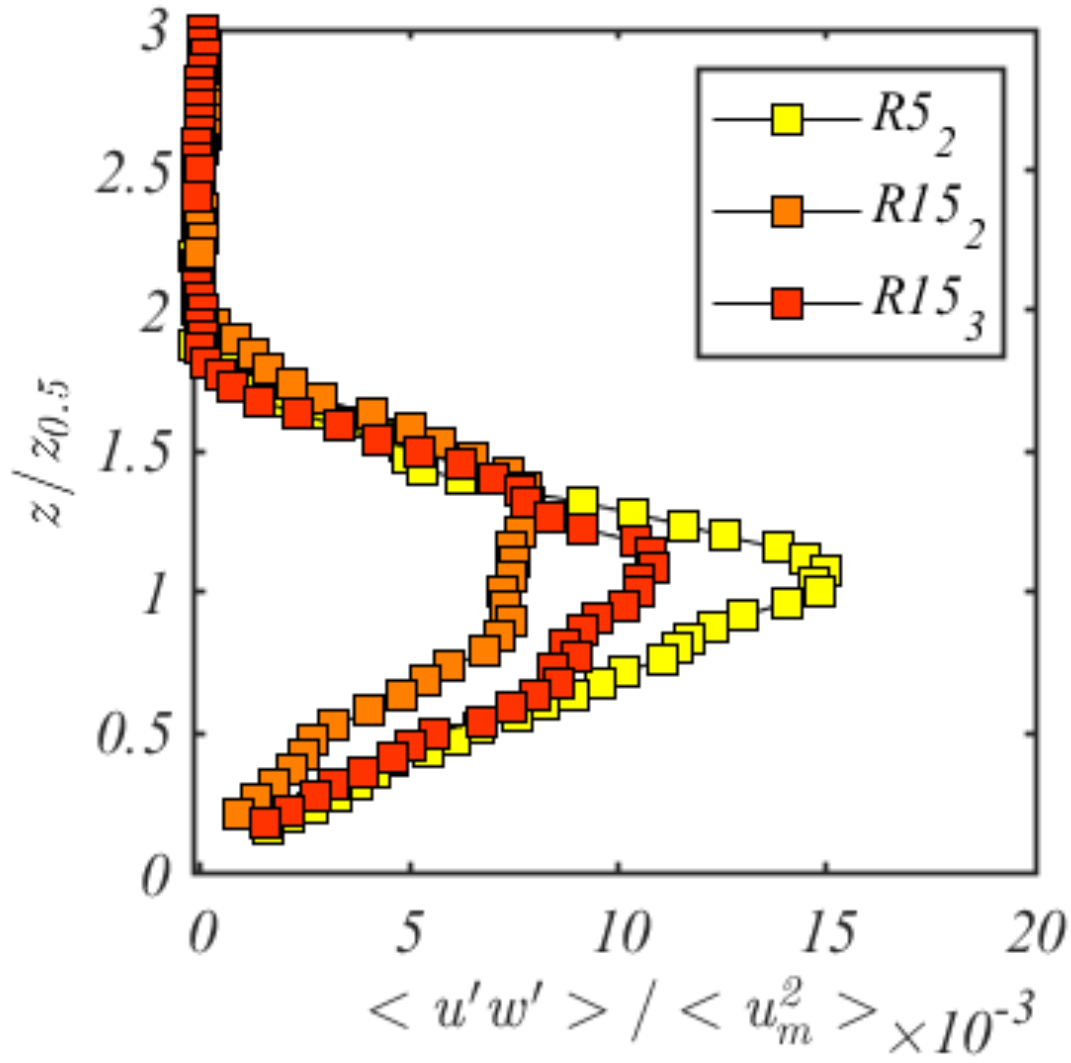
PLEASE CITE THIS ARTICLE AS DOI: 10.1063/5.0132830



10.1063/5.0

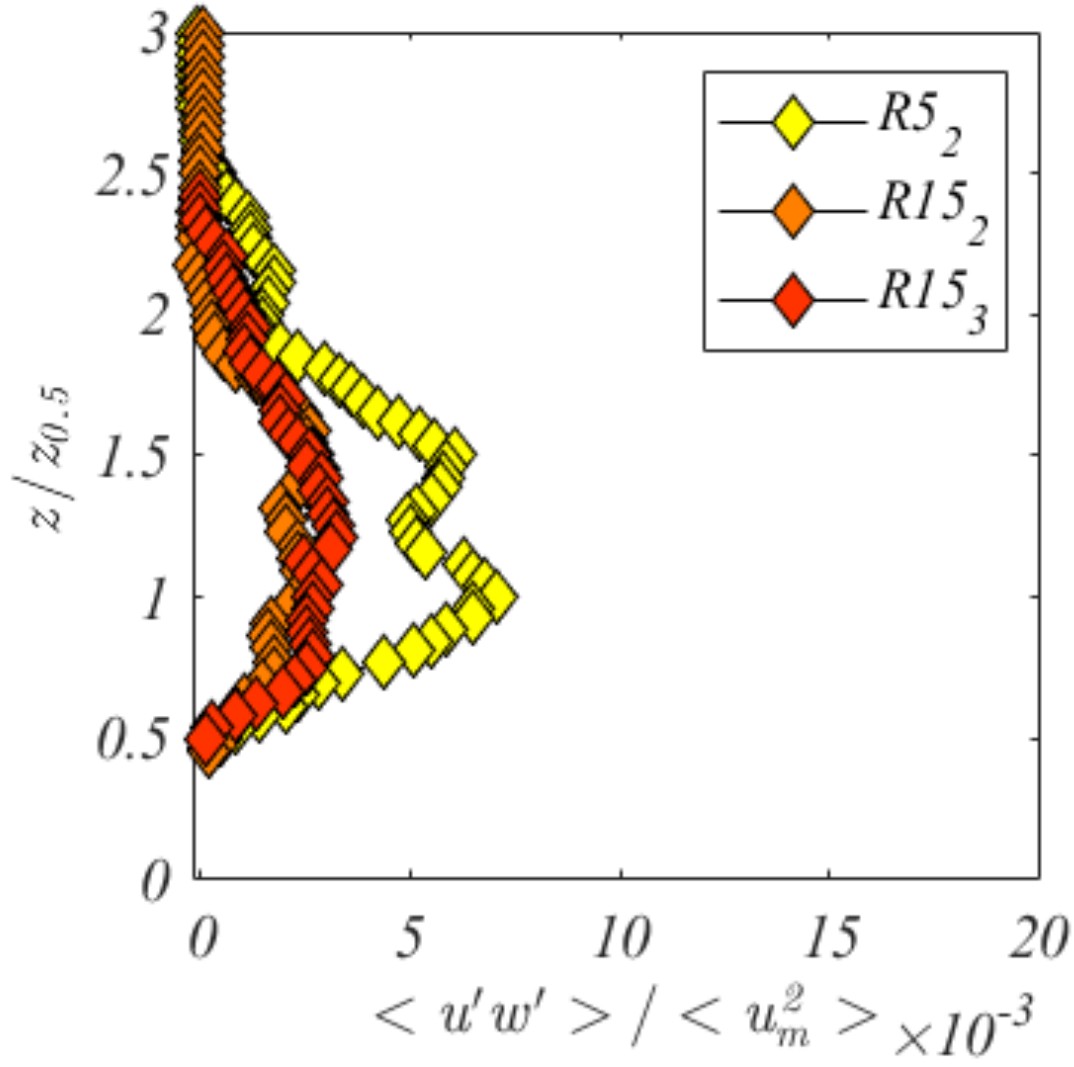
This is the author's peer reviewed, accepted manuscript. However, the online version of record will be different from this version once it has been copyedited and typeset.

PLEASE CITE THIS ARTICLE AS DOI: 10.1063/1.50132830



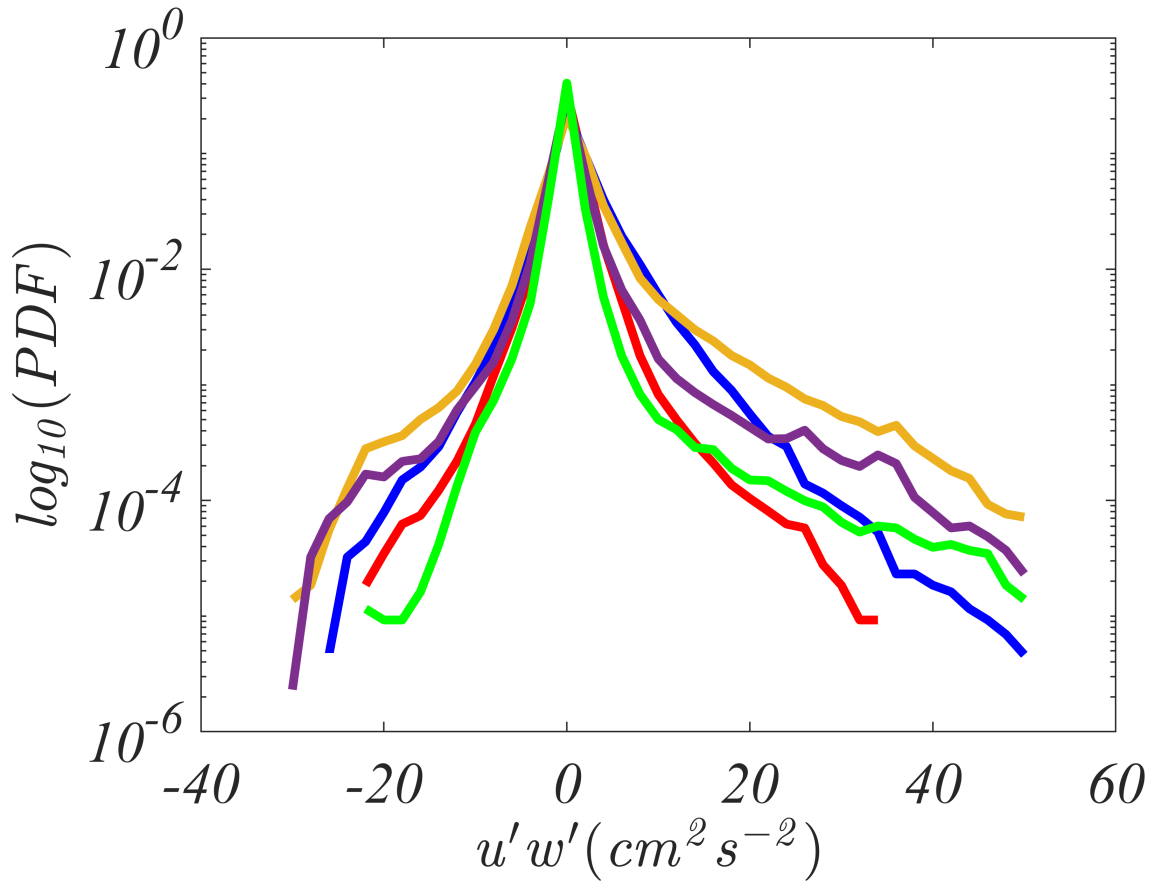
This is the author's peer reviewed, accepted manuscript. However, the online version of record will be different from this version once it has been copyedited and typeset.

PLEASE CITE THIS ARTICLE AS DOI: 10.1063/1.50132830



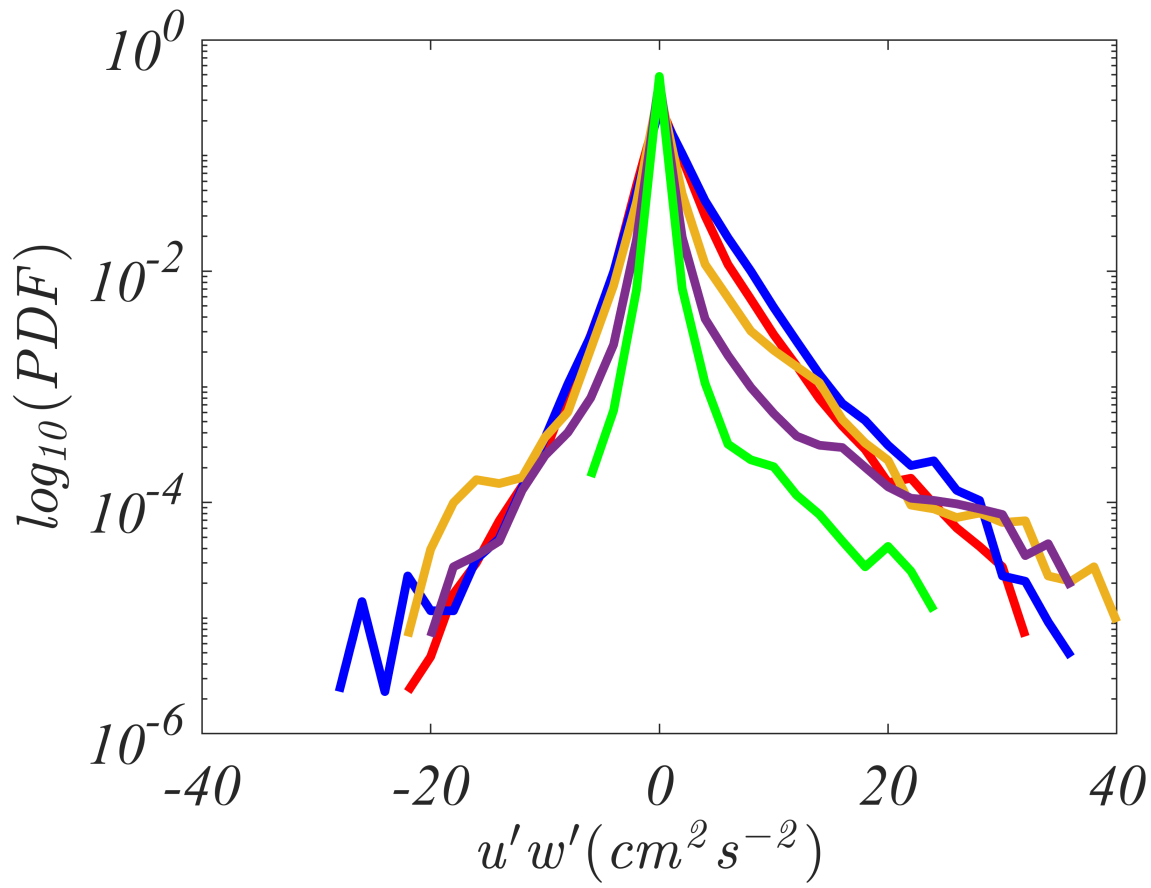
This is the author's peer reviewed, accepted manuscript. However, the online version of record will be different from this version once it has been copyedited and typeset.

PLEASE CITE THIS ARTICLE AS DOI: 10.1063/1.50132830



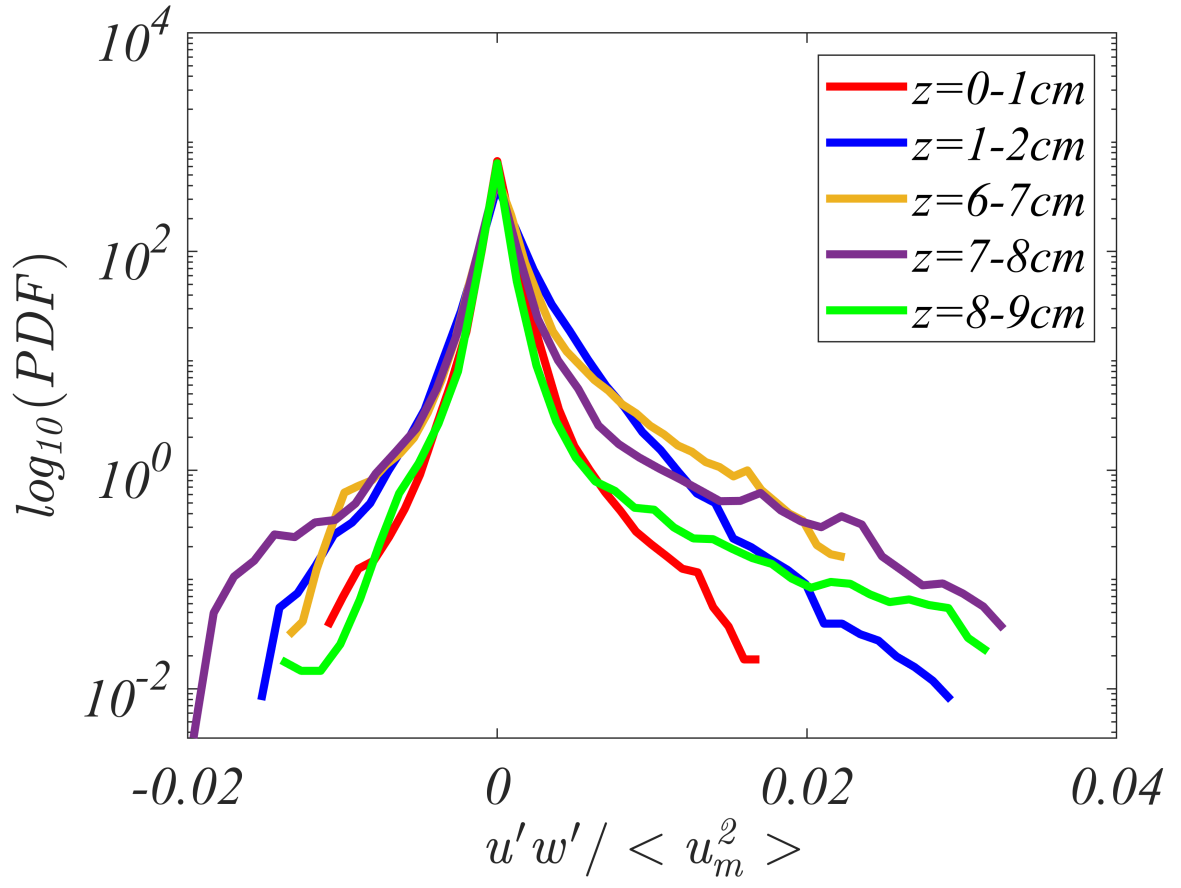
This is the author's peer reviewed, accepted manuscript. However, the online version of record will be different from this version once it has been copyedited and typeset.

PLEASE CITE THIS ARTICLE AS DOI: 10.1063/5.0132830



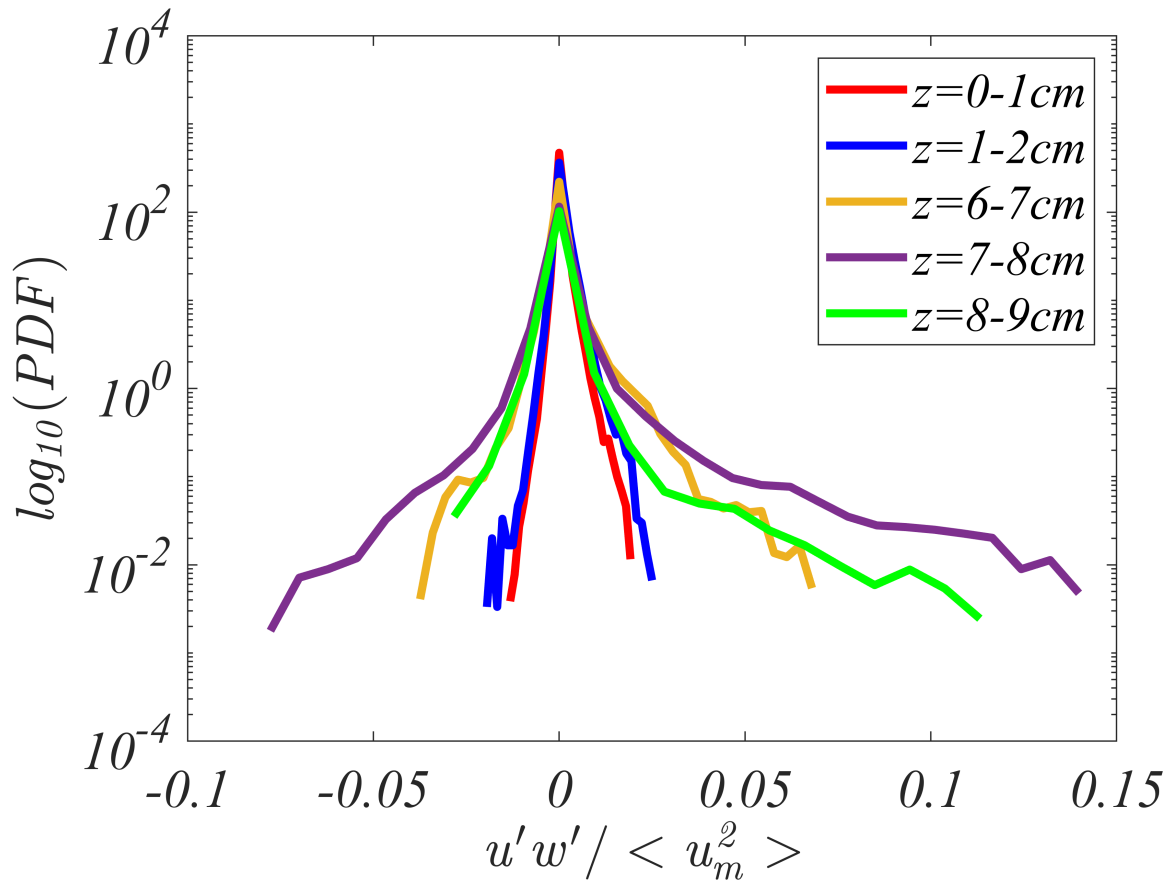
This is the author's peer reviewed, accepted manuscript. However, the online version of record will be different from this version once it has been copyedited and typeset.

PLEASE CITE THIS ARTICLE AS DOI: 10.1063/1.50132830



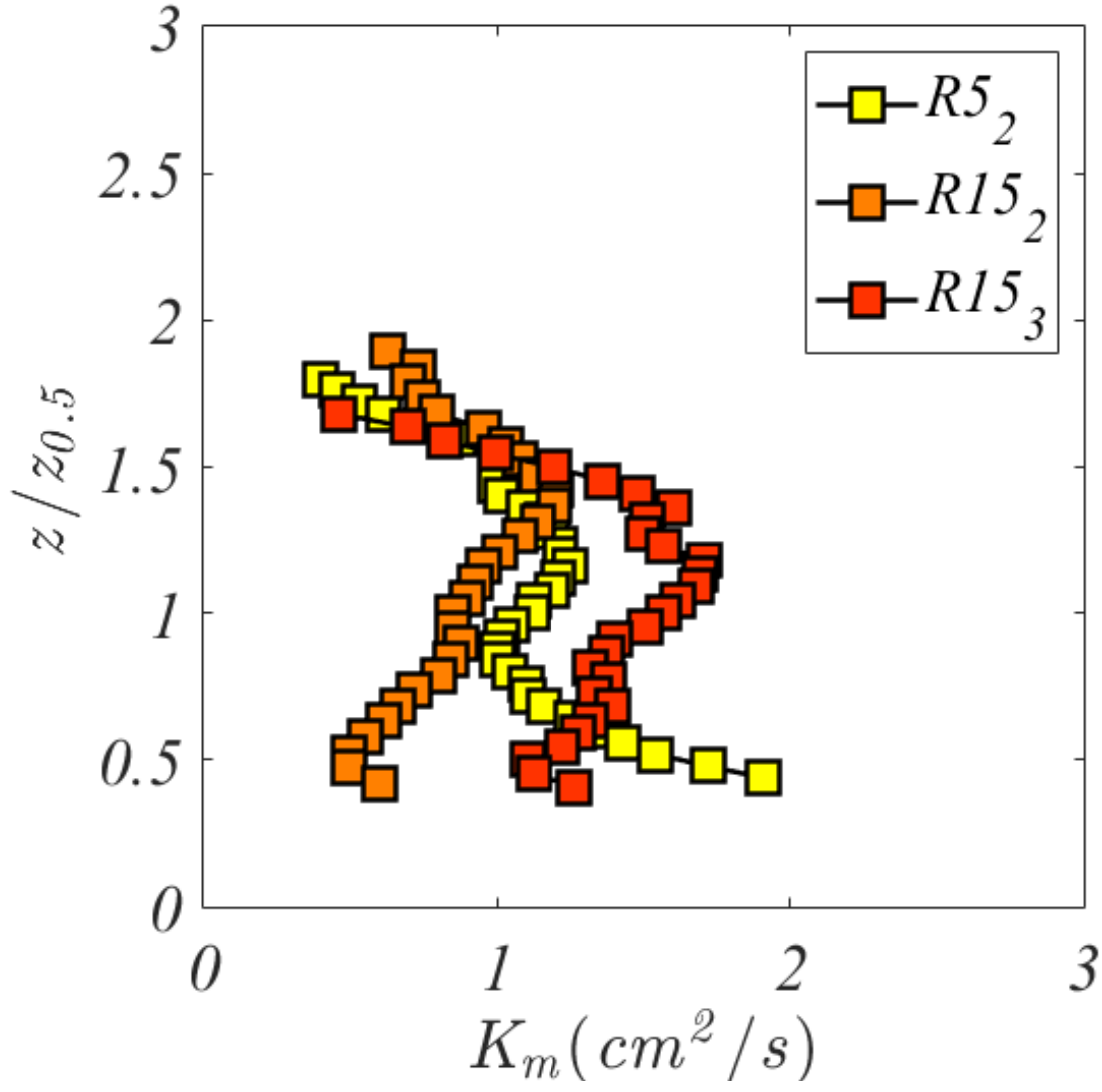
This is the author's peer reviewed, accepted manuscript. However, the online version of record will be different from this version once it has been copyedited and typeset.

PLEASE CITE THIS ARTICLE AS DOI: 10.1063/1.50132830



This is the author's peer reviewed, accepted manuscript. However, the online version of record will be different from this version once it has been copyedited and typeset.

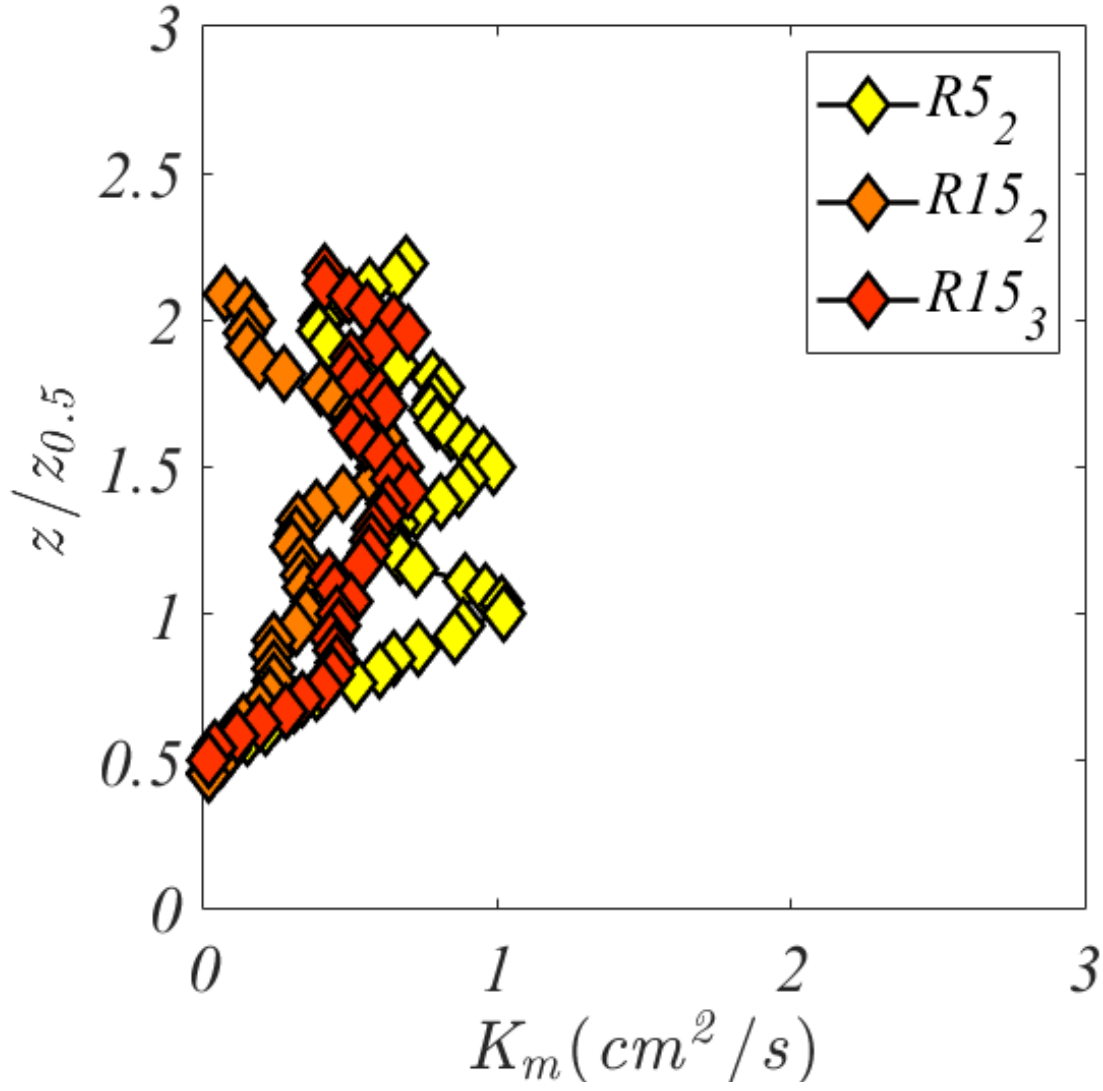
PLEASE CITE THIS ARTICLE AS DOI: 10.1063/1.50132830





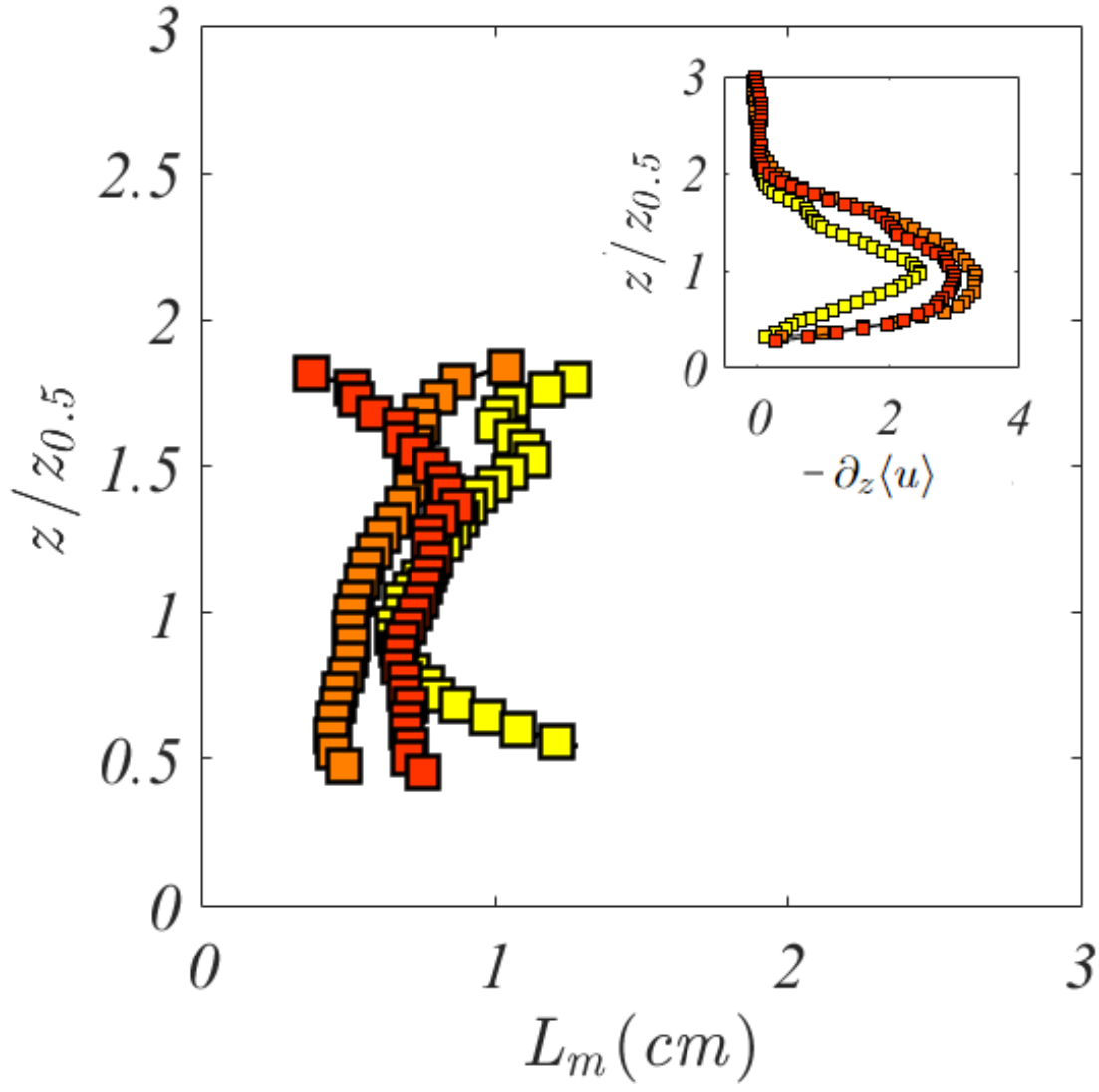
This is the author's peer reviewed, accepted manuscript. However, the online version of record will be different from this version once it has been copyedited and typeset.

PLEASE CITE THIS ARTICLE AS DOI: 10.1063/1.50132830



This is the author's peer reviewed, accepted manuscript. However, the online version of record will be different from this version once it has been copyedited and typeset.

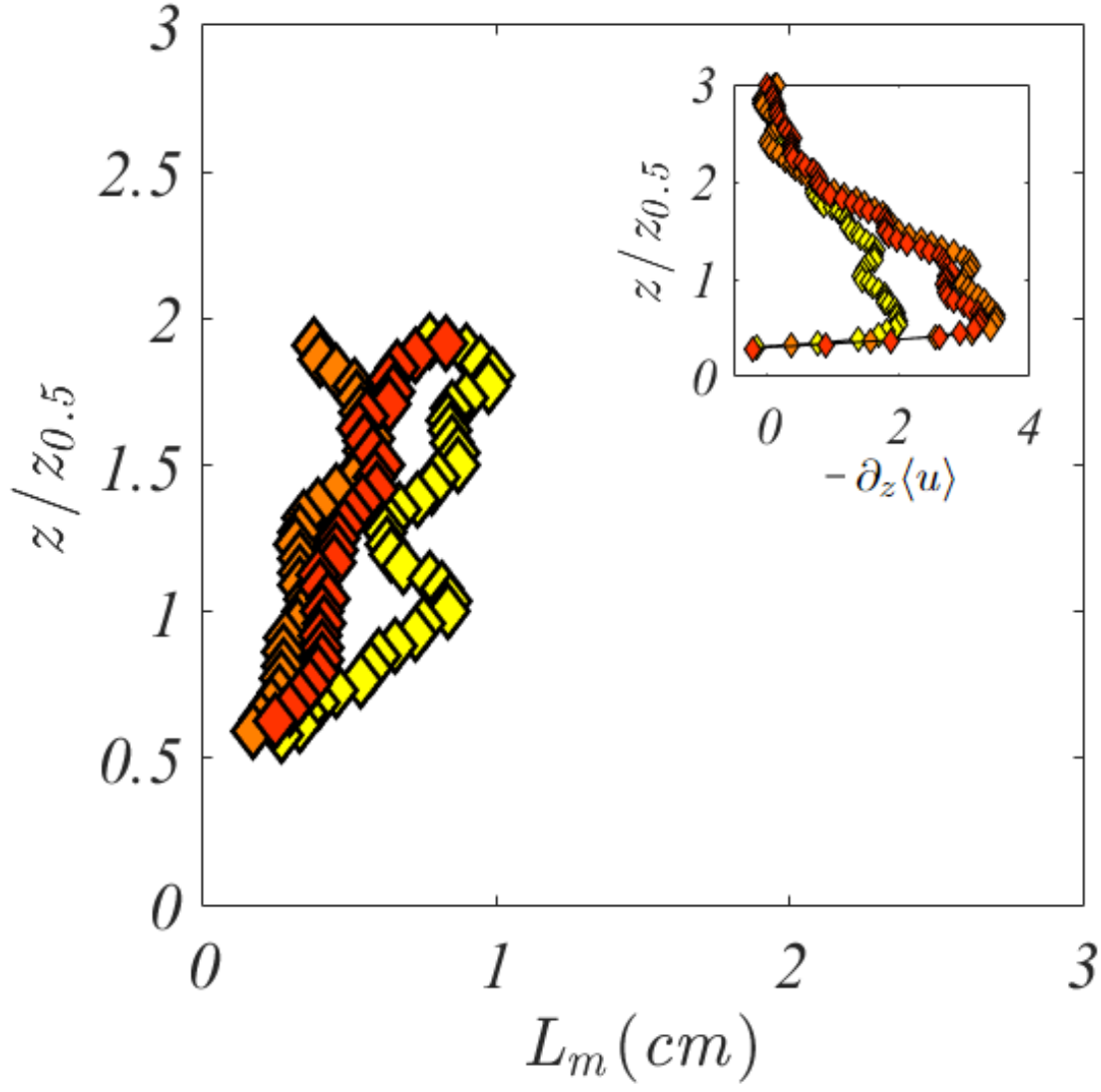
PLEASE CITE THIS ARTICLE AS DOI: 10.1063/5.0132830



10.1063/

This is the author's peer reviewed, accepted manuscript. However, the online version of record will be different from this version once it has been copyedited and typeset.

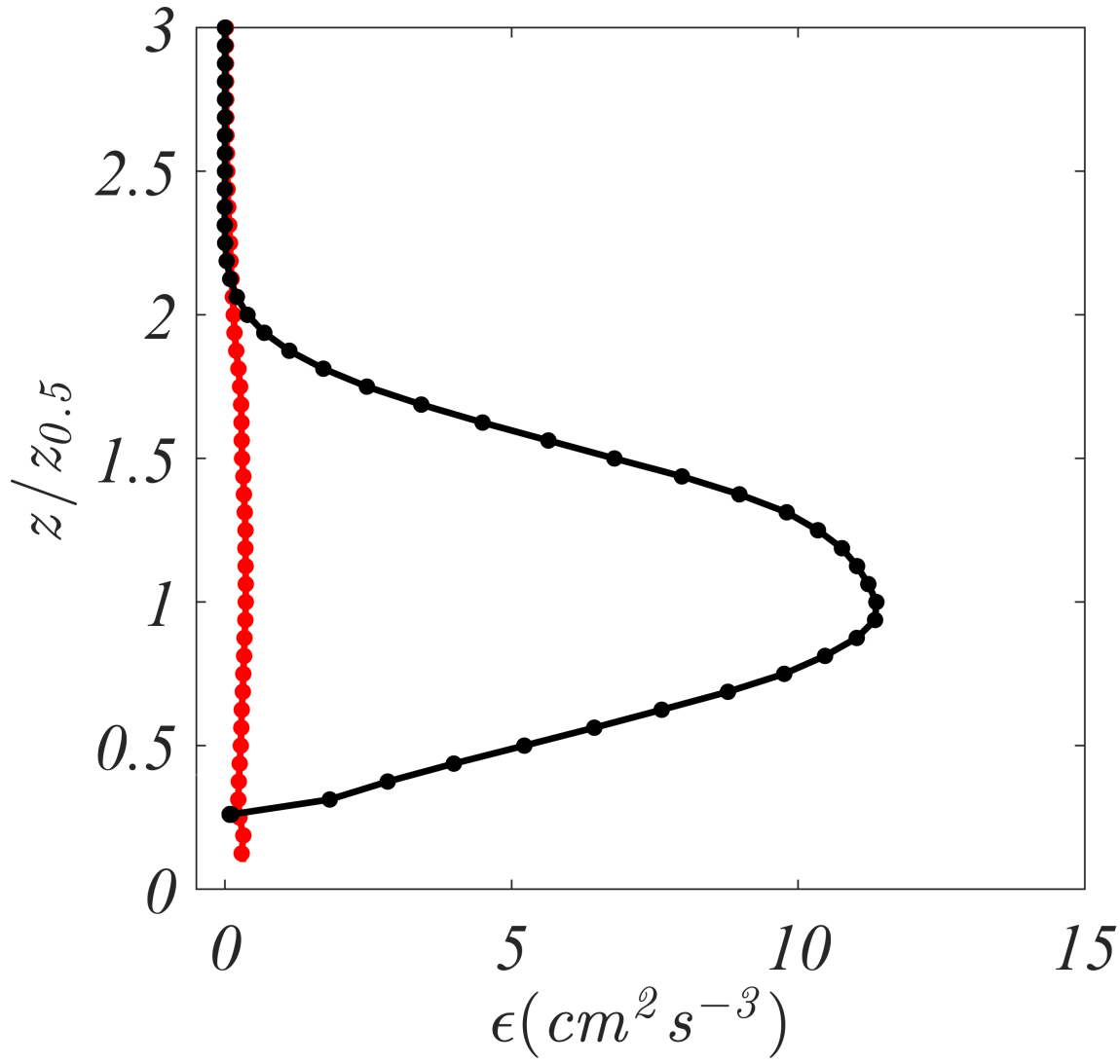
PLEASE CITE THIS ARTICLE AS DOI: 10.1063/5.0132830



10.1063/

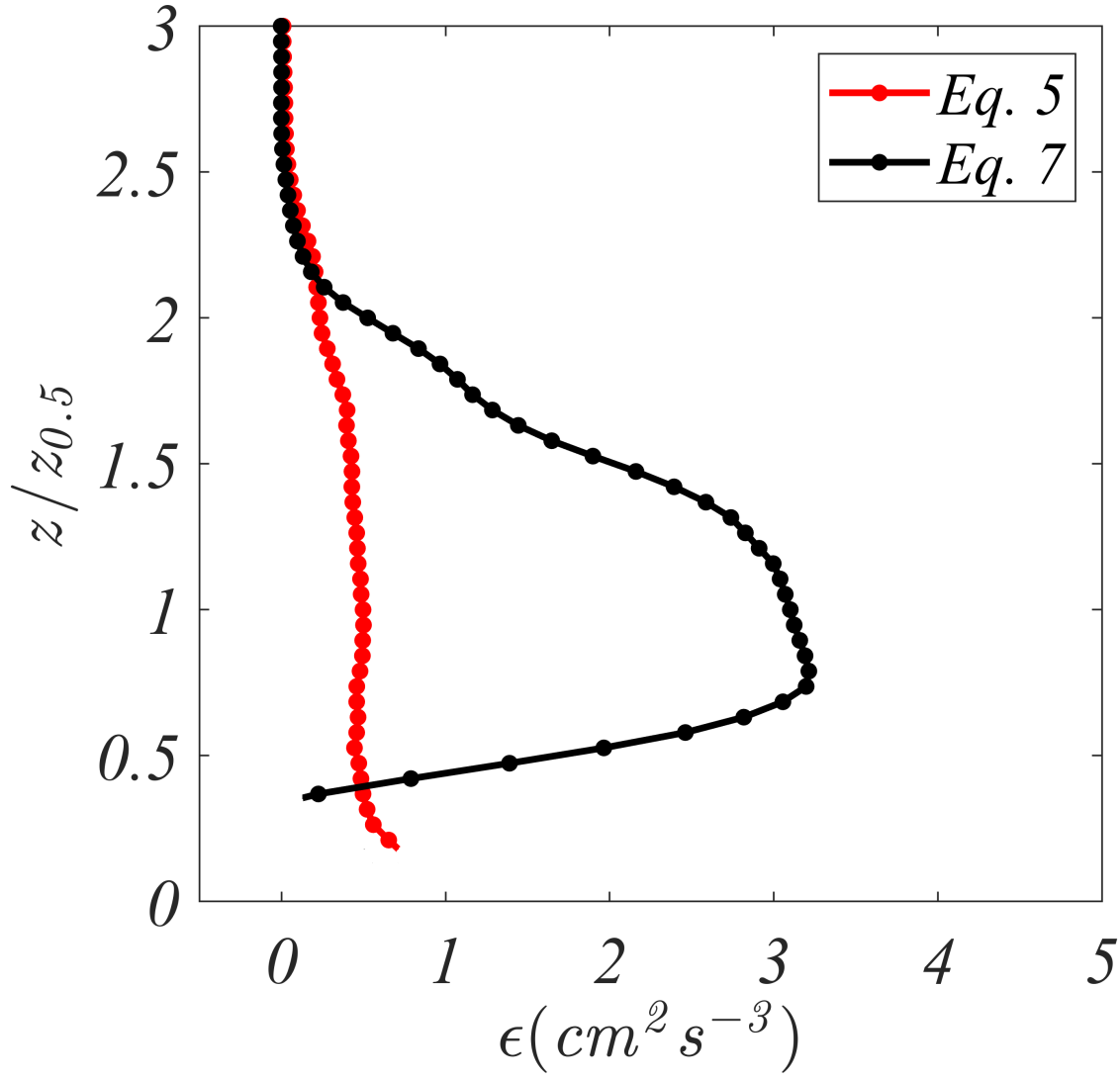
This is the author's peer reviewed, accepted manuscript. However, the online version of record will be different from this version once it has been copyedited and typeset.

PLEASE CITE THIS ARTICLE AS DOI: 10.1063/1.50132830



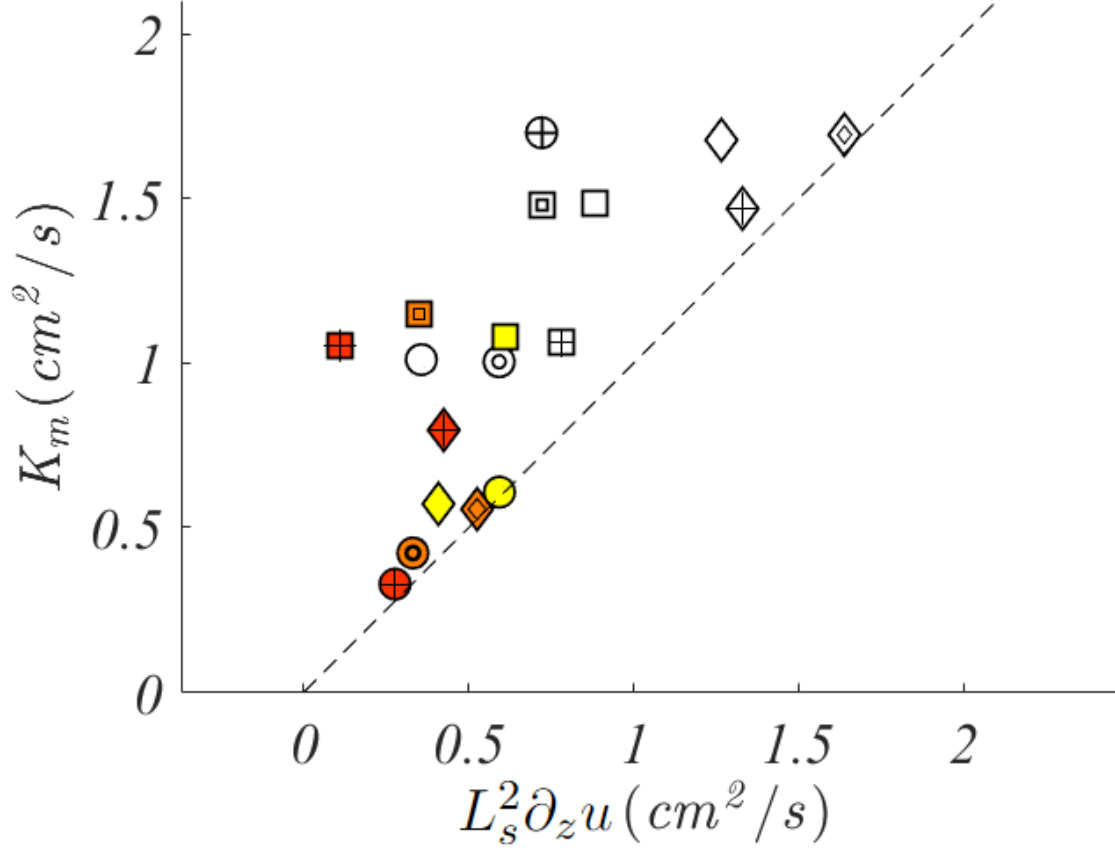
This is the author's peer reviewed, accepted manuscript. However, the online version of record will be different from this version once it has been copyedited and typeset.

PLEASE CITE THIS ARTICLE AS DOI: 10.1063/1.50132830



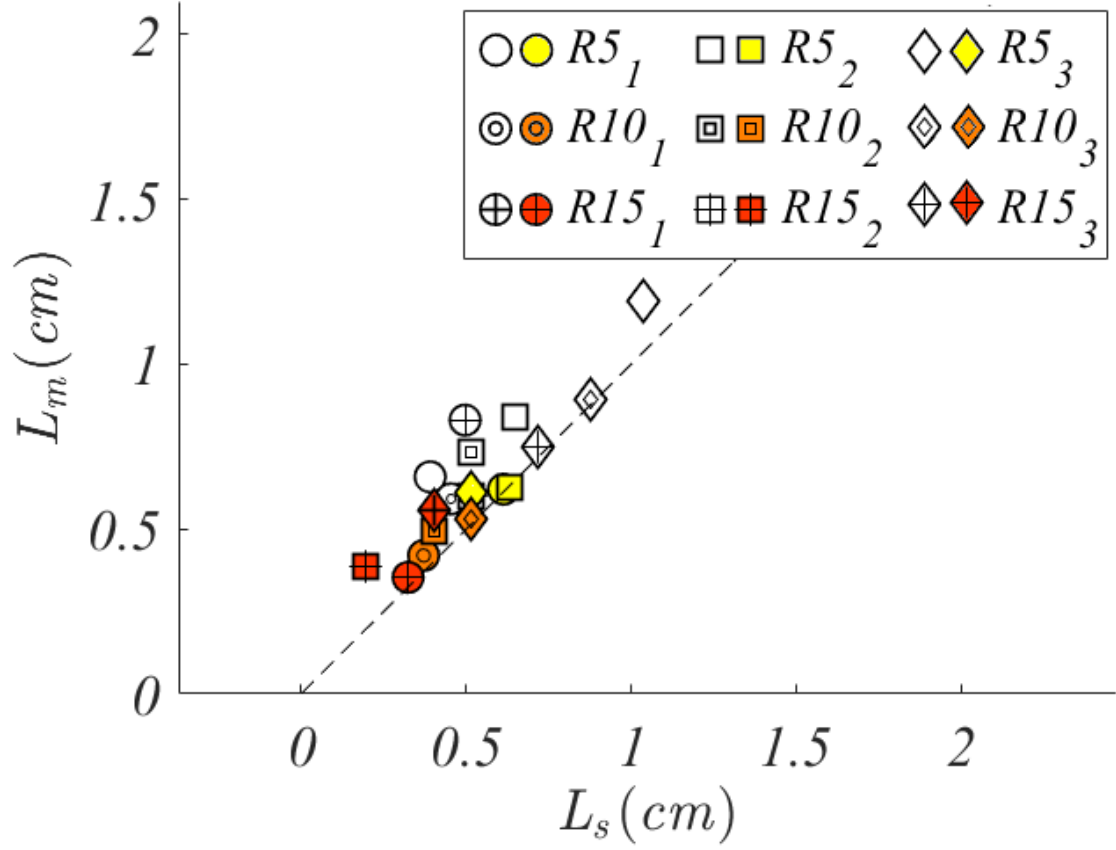
This is the author's peer reviewed, accepted manuscript. However, the online version of record will be different from this version once it has been copyedited and typeset.

PLEASE CITE THIS ARTICLE AS DOI: 10.1063/5.0132830



This is the author's peer reviewed, accepted manuscript. However, the online version of record will be different from this version once it has been copyedited and typeset.

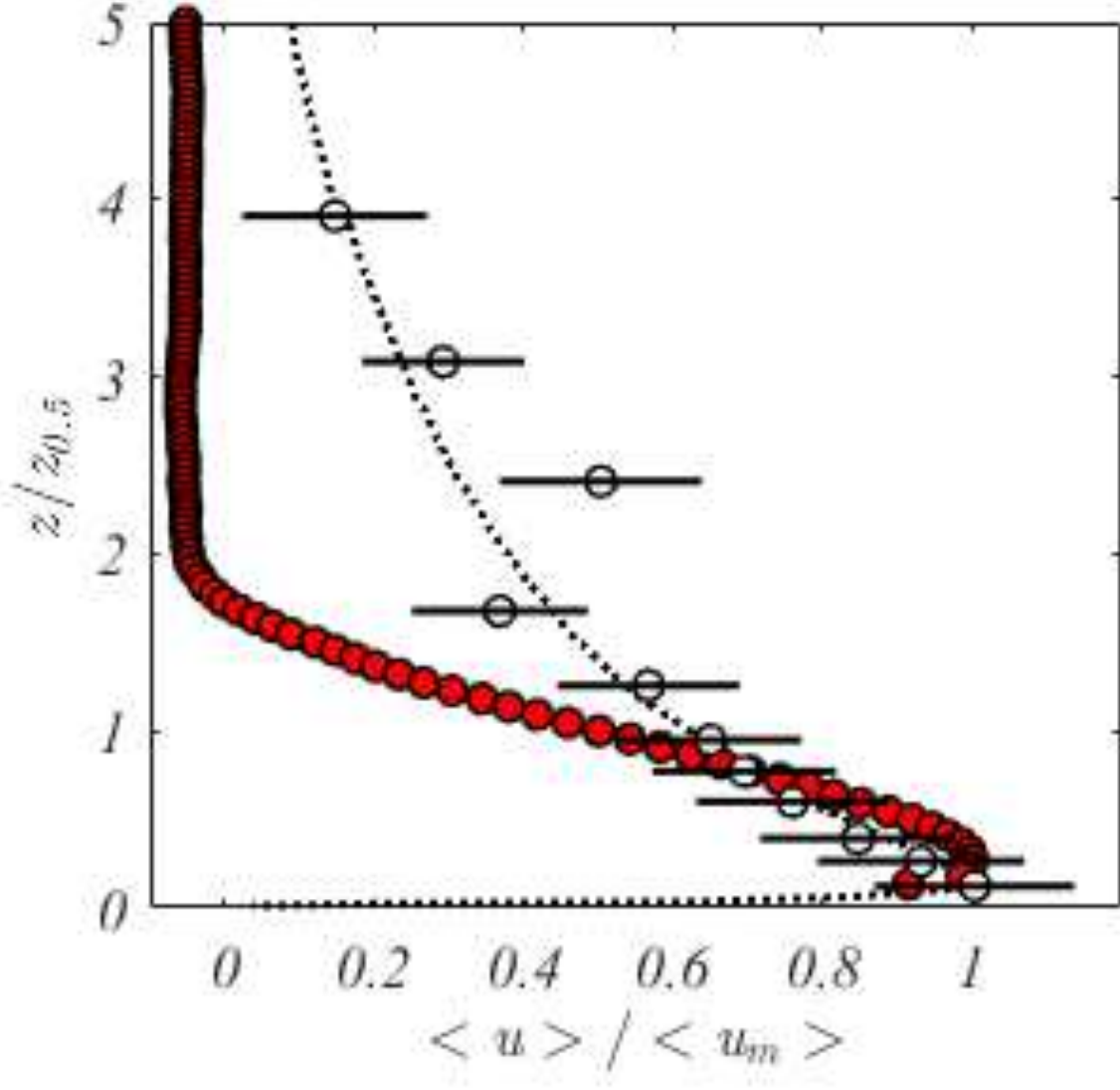
PLEASE CITE THIS ARTICLE AS DOI: 10.1063/5.0132830



# Fluids

This is the author's peer reviewed, accepted manuscript. However, the online version of record will be different from this version once it has been copyedited and typeset.

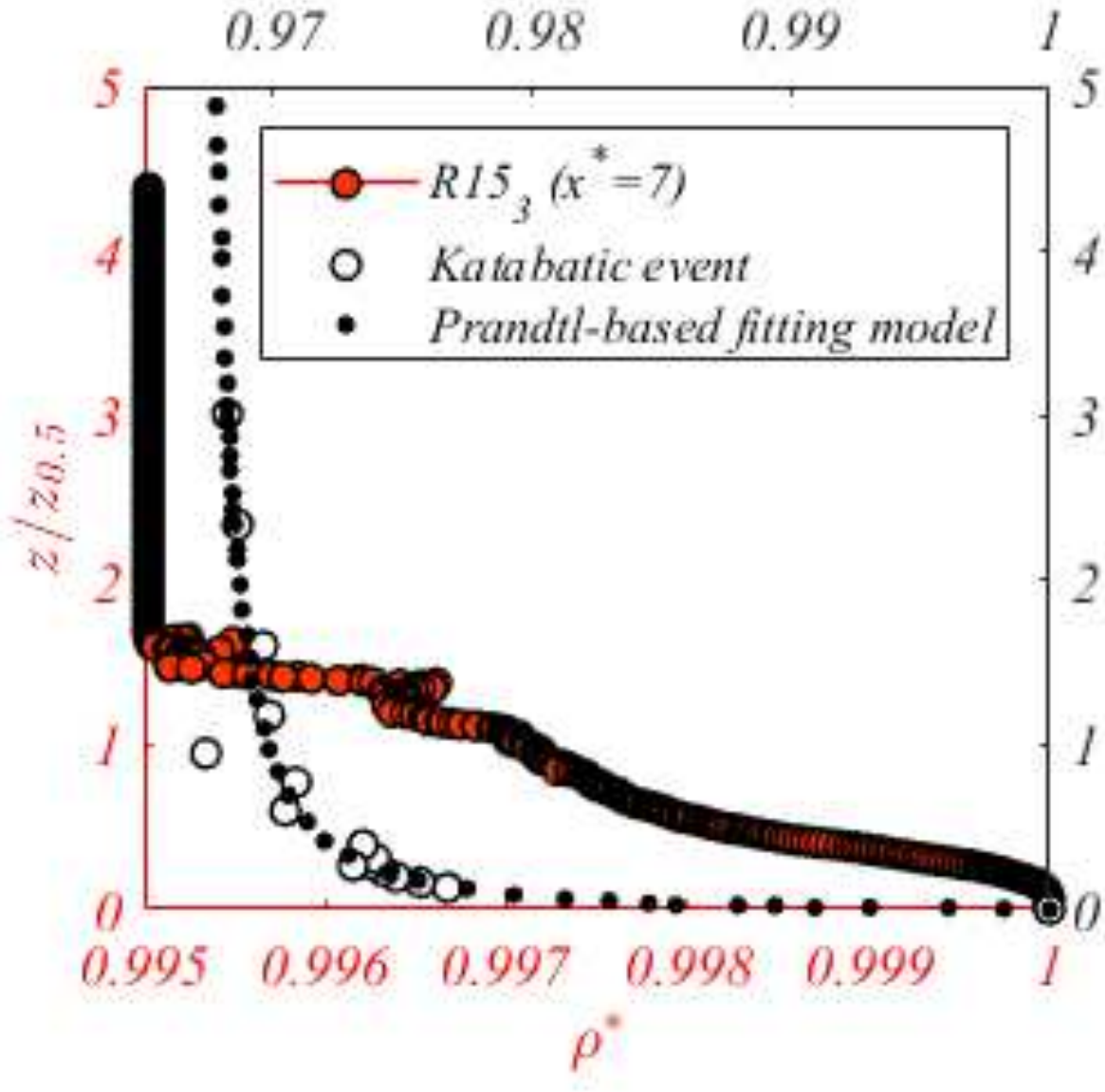
PLEASE CITE THIS ARTICLE AS DOI: 10.1063/1.50132830





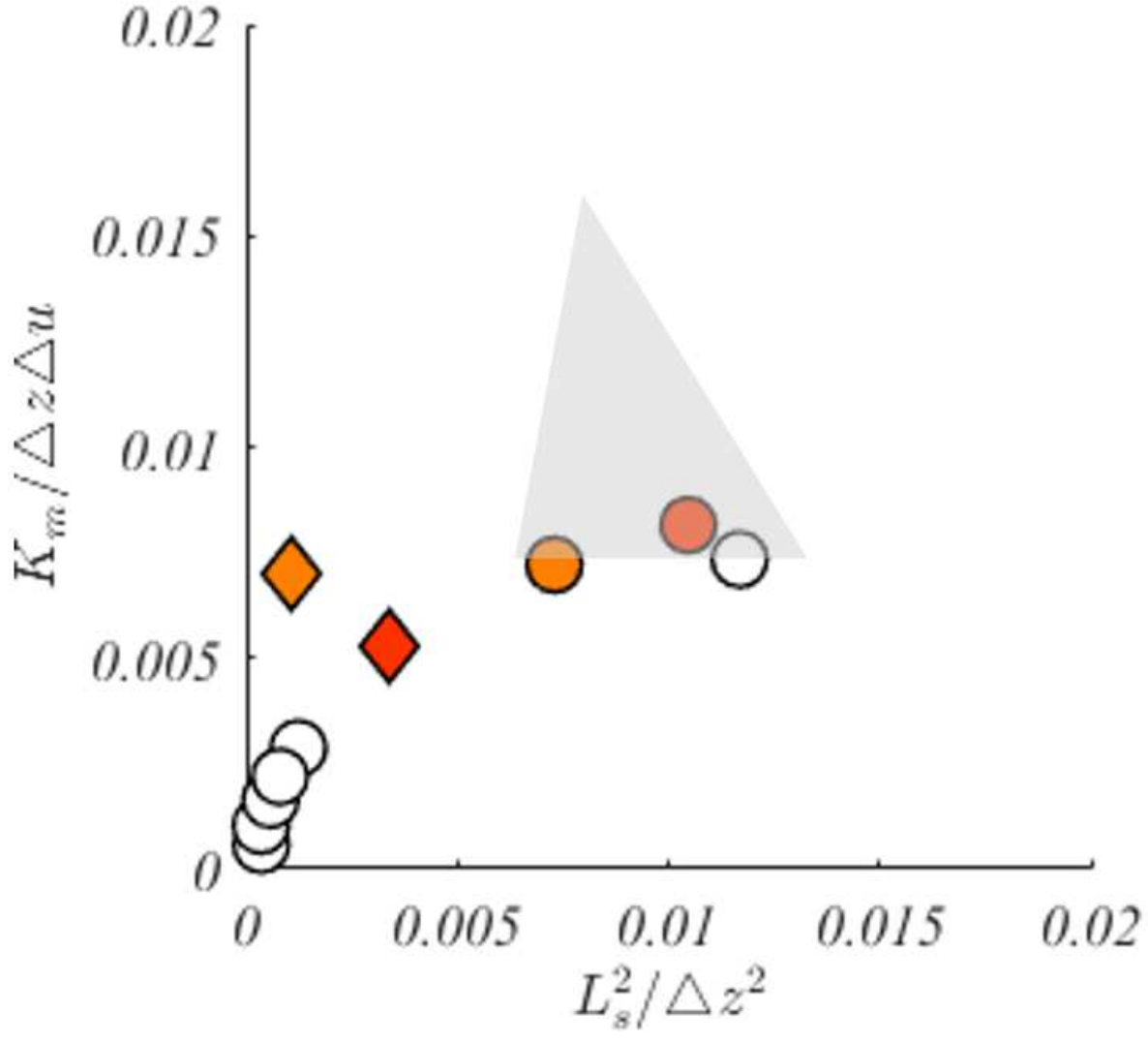
This is the author's peer reviewed, accepted manuscript. However, the online version of record will be different from this version once it has been copyedited and typeset.

PLEASE CITE THIS ARTICLE AS DOI: 10.1063/1.50132830



This is the author's peer reviewed, accepted manuscript. However, the online version of record will be different from this version once it has been copyedited and typeset.

PLEASE CITE THIS ARTICLE AS DOI: 10.1063/5.0132830



This is the author's peer reviewed, accepted manuscript. However, the online version of record will be different from this version once it has been copyedited and typeset.

PLEASE CITE THIS ARTICLE AS DOI: 10.1063/1.50132830

